Modélisation de la croissance des nanofils de Si et métrologie à l'échelle atomique de la composition des nanofils

Wanghua Chen

UNIVERSITÉ DE ROUEN
U.F.R. DE SCIENCES ET TECHNIQUES

␣ ␣ ␣ ␣ ␣ ␣ ␣ ␣ ␣ ␣␣ N° attribué par la bibliothèque

THÈSE
Pour l'obtention du grade de

DOCTEUR DE L'UNIVERSITÉ DE ROUEN

Discipline : Physique
Spécialité : Sciences des Matériaux

Présentée et soutenue publiquement le 17 novembre 2011 par

WANGHUA CHEN

Modeling the growth of Si nanowires and atomic scale metrology of Si nanowire composition

Directeur de Thèse : Philippe PAREIGE
Co-directeur de Thèse : Bruno GRANDIDIER
Encadrant : Rodrigue LARDE

Membres du Jury:

M. Daniel Bouchier	Directeur de Recherche CNRS – IEF, France	Rapporteur
M. Guido Schmitz	Professeur des Universités – IMP, Allemagne	Rapporteur
M. Pere Roca i Cabarrocas	Directeur de Recherche CNRS – LPICM, France	Président
M. Vladimir Dubrovskii	Professeur des Universités – Institut Ioffe, Russie	Examinateur
M. Philippe Pareige	Professeur des Universités – GPM, France	Directeur
M. Bruno Grandidier	Directeur de Recherche CNRS – IEMN, France	Co-directeur
M. Rodrigue Lardé	Maître de Conférences – GPM, France	Encadrant

Abstract

Si nanowires (NWs) are the typical one-dimensional nanomaterials and attract lots of interest in recent years due to their good properties and their wide range of possible applications. As far as their applications are considered, it is important to control their growth as well as their doping. Therefore, the aim of this thesis is devoted to the modeling the growth of Si NWs and the atomic scale metrology of Si NW composition

In the first part of this work, we study the NW growth rate (length) as well as the morphology such as tapering. Several models are proposed owing to different nature of NWs synthesized via different methods: Chemical Vapor Deposition (CVD) and Molecular Beam Epitaxy (MBE). Different growth rate tendencies are found depending on the synthesis methods. A good fit is found between the modeling and the experimental data. The influence of experimental conditions on NW morphology is also investigated in this part.

The aim of the second part of this thesis is devoted to the metrology of impurities (catalyst and dopant) in Si NWs using the Atom Probe Tomography (APT). This technique allows analysis at the atomic scale in real space with a three-dimensional analysis. Several types of Si NWs synthesized via different approaches such as etching, Vapor-Liquid-Solid (VLS) mechanism and Solid-Liquid-Solid (SLS) mechanism with different growth catalysts (Au, In and Sn) are investigated. The residing of catalyst atoms in Si NWs is found to be a rather general phenomenon and it is related to the catalyst types and growth mechanisms. The dopant concentration and distribution in Si NW produced by etching is unchanged. As far as the doped Si NWs via VLS mechanism are concerned, a formation of NW core-shell structure with an under-doped core surrounded by an over-doped shell is found whatever the NW morphology and dopant type. A NW sidewall diffusion-based model is proposed to reproduce experimental data and give a possible incorporation pathway for dopant into NW.

Key words: Si nanowires, etching, vapor-liquid-solid, solid-liquid-solid, atom probe, catalyst, dopant, growth rate, diffusion

Résumé

Les nanofils de silicium (Si) sont des nano-objets à une dimension. Ils font l'objet de beaucoup d'intérêt ces dernières années en raison de leurs bonnes propriétés et leur grand potentiel d'applications. Pour ces applications, il est important de parfaitement contrôler la croissance de ces objets ainsi que leurs dopages. Dans ce contexte, l'objectif de ce travail de thèse est la modélisation de la croissance des nanofils de Si et la métrologie à l'échelle atomique de la composition des nanofils.

Dans la première partie de ce travail, nous avons étudié le taux de croissance (longueur) ainsi que l'évolution de la morphologie des nanofils, en particulier l'effet d'effilage. Plusieurs modèles sont proposés selon la nature des nanofils synthétisés via différentes méthodes d'élaboration: Dépôt Chimique en phase Vapeur et Epitaxie par Jets Moléculaires. Les taux de croissance varient selon les méthodes de synthèse. Le modèle reproduit fidèlement les données expérimentales. L'influence des conditions expérimentales sur la morphologie des nanofils est également étudiée dans cette partie.

L'objectif de la seconde partie de ce travail est la métrologie des impuretés (catalyseur et dopant) dans les nanofils de Si. Cette étude est réalisée à l'aide de la technique de Sonde Atomique Tomographique (SAT). Cette technique permet une analyse à l'échelle atomique, dans l'espace réel et en trois dimensions de l'objet analysé. Des nanofils synthétisés par différentes techniques telles : la gravure chimique, la méthode Vapeur-Liquide-Solide (VLS) et la méthode Solide-Liquide-Solide (SLS), en utilisant différents catalyseurs de croissance tels Au, In et Sn, sont étudiés. La présence d'atomes des catalyseurs dans les nanofils se trouve être un phénomène général. Un travail sur la métrologie des dopants a également été réalisé. La concentration des dopants et leurs distributions dans les nanofils synthétisé par gravure chimique est inchangée. En revanche, dans les nanofils de Si dopés via un mécanisme de croissance VLS, une structure cœur-coquille avec un cœur sous-dopé et une coquille sur-dopée est observée. Ceci est retrouvé quelque soit la morphologie du nanofil et la nature chimique du dopant. Un modèle basé sur la diffusion latéral (via la surface du nanofil) des dopants est proposé afin de reproduire les profils expérimentaux observés et aussi préciser une voie d'incorporation possible des dopants.

Mots clés: nanofils de Si, gravure, vapeur-liquide-solide, solide-liquide-solide, sonde atomique, catalyseur, dopant, taux de croissance, diffusion

Remerciements

Ce travail de thèse s'est déroulé au sein du Groupe de Physique des Matériaux (GPM) UMR CNRS 6634 de l'Université et INSA de Rouen. Il a été réalisé en collaboration avec l'Institut d'Electronique, de Microélectronique et de Nanotechnologie (IEMN) de Lille et dans le cadre d'un projet de la Direction Générale de l'Armement (DGA). Une partie de ce travail a également été réalisé en collaboration avec le Laboratoire de Physique des Interfaces et Couches Minces (LPICM) de l'École Polytechnique (Palaiseau).

Je tiens tout d'abord à remercier Pr. Philippe Pareige, Dr. Bruno Grandidier et Dr. Rodrigue Lardé pour leur encadrement, leur confiance et leur soutien tout au long de ces trois années. Je les remercie également pour toutes leurs compétences scientifiques, leurs dynamismes, leur sens de la pédagogie, leur bonne humeur, leurs encouragements et leur disponibilité.

Je remercie également Pr. Didier Blavette, directeur du GPM, de m'avoir accueilli au sein de son laboratoire.

Je remercie l'ensemble des membres du jury d'avoir accepté d'évaluer ce travail: M. Pere Roca i Cabarrocas, Directeur de Recherche au LPICM de Palaiseau, qui m'a fait l'honneur d'accepter la présidence de ce jury; M. Daniel Bouchier, Directeur de Recherche à l'IEF d'Orsay et M. Guido Schmitz, Professeur de l'Université de Münster pour avoir accepté d'en être les rapporteurs ainsi que M. Vladimir Dubrovskii, Professeur de l'Université d'État de Saint-Pétersbourg pour avoir accepté de collaborer et examiner ce travail.

Je remercie également Dr. Emmanuel Cadel, du GPM, pour m'avoir initié aux manipulations complexes de la plateforme de microscopie électronique à balayage.

Un grand merci à toutes les personnes qui m'ont aidé et à toutes les personnes du laboratoire aux côtés desquelles j'ai évolué durant ces trois années.

Pour finir, j'adresse mes plus vifs remerciements à mes parents et ma sœur situés de l'autre côté de la Terre.

Contents

Introduction

There is a great increase of the energy consumption and a strong demand for more powerful devices as standard of living improves. Plenty of sciences and technologies such as nano and bio emerge with these requirements. Just as indicated by Richard Feynman in 1959 that “there is plenty of room at the bottom” [1], the nanoscience and nanotechnology have attracted more and more interest in recent years. Nanoscience and nanotechnology is the study and ability to fabricate, manipulate, model and characterize matter at the nanoscale. Plenty of materials and applications have been found since the emergence of nanoscience and nanotechnology in 1980s. Among the different domains in nanoscience and nanotechnology, nanomaterials as the basic building blocks are the mainstream. Nanomaterials are materials with morphological features at nanoscale. They can be semiconductors, metals, ceramics, polymeric or composite materials. They exhibit new properties in domains such as electronics [2] and photonics [3] for example. However, these nanomaterials as new materials also impose the challenges such as their synthesis and characterization.

Among the number of nanomaterials, Si nanowires (NWs) are important ones which have been studied extensively due to the abundance of this material and the maturity of the existing Si-based technology. Si NWs are the typical one-dimensional nanomaterials that exhibit good properties as compared to the Si bulk [4]. These properties open new perspectives in different domains such as solar cells [5]. But successful applications of Si NWs depend largely on the control to synthesize them. Hence, it is a key and necessary issue to understand and control effectively their growth as well as their doping process. As far as the synthesis of Si NWs is considered, two different approaches can be considered: the “top-down” approach (auto-assembly of Si atoms) and the “bottom-up” approach (cut of Si bulk). Both approaches have their advantages and disadvantages as it will be shown.

In recent years, a number of research works have been done from theory to experience since the discovery of the Vapor-Liquid-Solid (VLS) mechanism by Wagner and Ellis in 1964 [6]. However, there are still several aspects that are not fully understood. For example, what is the origin of the differences observed in the dependence of the growth with the NW diameter when the growth method changes? Can we narrow the NW length distribution effectively? How do the experimental growth conditions influence the NW morphology, leading to the formation of cylindrical or more tapered shapes? Therefore, the first part of this present work will try to partly answer these important questions, by modelling the NW growth rate.

As the conductivity of pure Si bulk crystal is too small for electronic applications, this material must be doped. Moreover, the synthesis of Si NWs based on the "bottom-up" approach using a catalyst, such as Au, may lead to the diffusion of the catalyst atoms into the NWs. Such incorporation of impurities is known to affect the electrical properties of Si [7]. Therefore, locating impurities such as catalyst atoms and dopants in Si NWs is important to understand and control the transport properties of Si NWs. In order to realize this, appropriate characterization tools are necessary. In this work, the Atom Probe Tomography (APT) [8] which is a three dimensional analytical high resolution microscope is chosen as the main technique due to its unique ability to study the chemical composition of nanostructures at the atomic scale. Such a powerful technique will allow to answer key questions, such as: Do the catalyst atoms such as Au, In and Sn can reside in Si NW considering the different growth mechanisms? What is the level of concentration of these impurities? How are the impurities distributed in Si NWs? How do dopant atoms incorporate in Si NWs? In a word, the second part of this work is based on the use of the APT technique for the metrology of single Si NWs at the atomic scale. Here, it must be noted that the use of the APT technique for the characterization of Si NW with a high success rate, strongly depends on the preparation of an appropriate sample. Therefore, the manipulation of single NWs and the development of convenient and effective sample preparation methods were an important and key issue in the realization of this work. The use of a dual beam Scanning Electron Microscope was essential for the nanoscale observation and manipulation of single NWs.

After an introduction that provides a summary of the "state of the art" on NWs (chapter I), this research work will consist of four chapters. Chapter II focuses on the experimental techniques either for the syntheses of NWs or for their characterizations (Scanning Electron Microscopy (SEM) with Focused Ion Beam (FIB), Transmission Electron Microscopy (TEM) and APT). The basic concepts of the main technique used in this work, namely the APT are also given in detail.

Chapter III is a chapter concerning the modelling of NW growth rate (length) and the tapering effect. Several models are proposed here and discussed based on nanoscale experimental observation.

Chapter IV deals with the investigation of catalyst atoms that reside in Si NWs synthesized owing to different growth mechanisms (VLS (out of plane) and SLS (in plane)) and metallic seed particles (Au, In and Sn).

The last chapter describes the ability of the atom probe technique in the dopant (n- or p-type) metrology for out of plane Si NWs elaborated by different methods, namely etching and VLS process.

Finally, a general conclusion and perspectives are given.

Bibliography of introduction

[1] R. Feynman, Caltech's Engineering and Science Magazine (1960)
[2] R. Rurali, Rev. Mod. Phys., 82, 427 (2010)
[3] R. Yan, D. Gargas, and P. Yang, Nat. Photonics, 3, 569 (2009)
[4] A. I. Hochbaum, R. Chen, R. D. Delgado, W. Liang, E. C. Garnett, M. Najarian, A. Majumdar, and P. Yang, Nature, 451, 163 (2008)
[5] E. C. Garnett, M. L. Brongersma, Y. Cui, and M. D. McGehee, Annu. Rev. Mater. Res., 41, 269 (2011)
[6] R. S. Wagner, and W. C. Ellis, Appl. Phys. Lett., 4, 89 (1964)
[7] A. J. Tavendale, and S. J. Pearton, J. Phys. C: Solid State Phys., 16, 1665 (1983)
[8] M. K. Miller, A. Cerezo, M. G. Hetherington, and G. D. W. Smith, oxford science publications (1996)

Chapter I

I State of the art

I.1 Semiconductor nanowires

Zero-dimensional nanostructures (e.g. quantum dots), one-dimensional nanostructures (e.g. nanowires) and two-dimensional nanostructures (e.g. quantum wells) are the three types of low dimensional nanostructures. The one-dimensional nanostructure can be defined as a nanostructure with a very high length to diameter ratio (tens to several nanometers in width and unconstrained length). It includes two main categories: nanotubes (NTs) and nanowires (NWs), the last one being the subject of this work. According to physical properties (mostly transport and optical properties), NWs can be categorized into three different types: semiconductor NWs (e. g. Si, ZnO, GaAs and InP), metallic NWs (e. g. Cu and Pt) and insulating NWs (e. g. SiO_2). NWs can exhibit specific properties compared to bulk materials because of NWs' high surface to volume ratio and quantum confinement [1]. Plenty of material properties (electronics [2], photonics [3], mechanical [4] and thermal [5]) will become pronounced or different when the material size decreases towards nanoscale. NWs can be used as functional components or as connections for nano components, this will be illustrated in a next paragraph. Among the semiconductor NWs, three main types are developed: group II-VI (ZnO), group III-V (GaAs) and group IV (Si). This work is mostly devoted to the study of group IV NWs.

Group II-VI (ZnO)

ZnO NWs are the typical group II-VI semiconductor NWs with a large band gap of 3.37 eV at room temperature. ZnO NWs can also exhibit the piezoelectric property because of their non-symmetrical central structure. ZnO NWs are an energy harvesting and conversion material that can serve as solar cells [6], nanogenerators [7] and hybrid conversion structures [8]. Several methods can be used to grow ZnO nanostructure. The two mostly utilized methods are the chemical method [9] and the thermal evaporation [10]. ZnO has a good plasticity and can be grown with different types of nanostructure. Figure I.1 is a series of SEM images of ZnO nanostructures with different morphologies. Figure I.1 (a) shows ZnO NWs array grown on a single crystal alumina substrate using VLS mechanism with Au as catalyst [11]. Figure I.1 (b) shows ZnO NWs grown on an alumina substrate using VLS

mechanism with Ge as catalyst [12]. Figure I.1 (c) is an image of ZnO nanobelts with a helical nanostructure [13]. ZnO can also be grown as nanosprings because of the existence of ZnO polar surface (Figure I.1 (d)) [14].

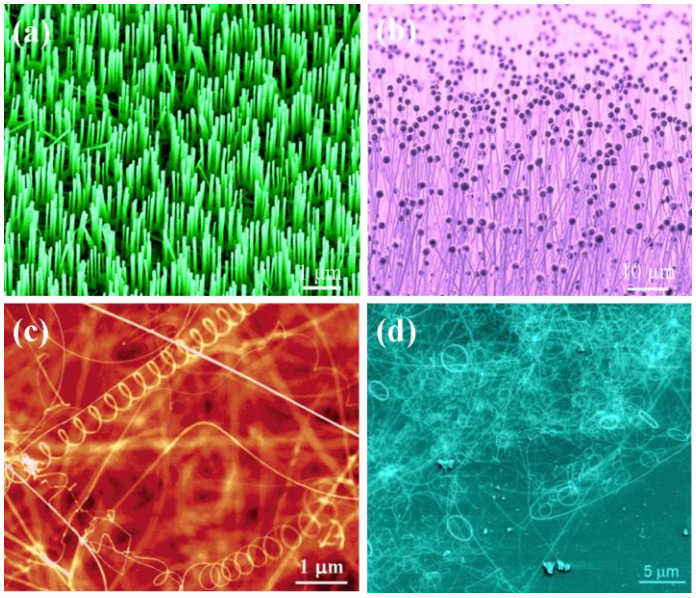

Figure I.1– A series of scanning electron microscopy images of ZnO nanostructures. (a) ZnO NW arrays grown on a single crystal alumina substrate [11]. (b) Ge-catalyzed ZnONWs on an alumina substrate [12]. (c) ZnO nanobelts with helical nanostructure [13]. (d) ZnO nanorings [14].

Group III-V (GaAs)

GaAs NWs are typical III-V semiconductor NWs. They can be applied in the domains such as electronics [15] and photovoltaics [16]. The principle growth method of GaAs NWs is CVD [17] and MBE [18]. Figure I.2 is a SEM side view of GaAs NWs grown by MBE method on a (311) B surface [19].

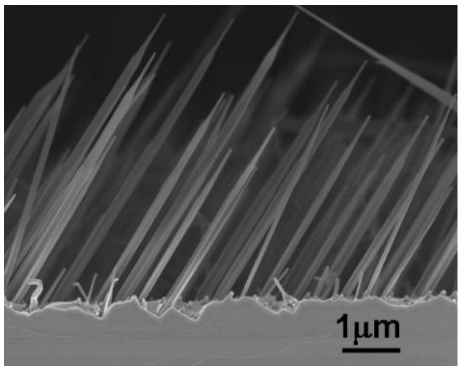

Figure I.2– Scanning electron microscopy image of zinc blende GaAs NWs grown on a (311) B surface. The NW growth direction is (001). Adapted from [19].

Group IV (Si)

Si NWs and Ge NWs are two types of group IV semiconductor NWs. Lots of methods can be utilized to grow Si NWs. Figure I.3 is a group of images of Si NWs synthesized by several of these methods and observed with SEM. Si NWs can exhibit different morphologies depending on the growth methods. Figure I.3 (a) is an image of Si NWs grown by the CVD method [20]. Figure I.3 (b) is an image of vertically aligned, diameter-controlled Si NWs grown from ordered Au dots on Si (111) substrates via porous anodic alumina mask [21]. Figure I.3 (c) is an image of Si NWs grown on a Si (111) substrate using MBE method [22]. Finally, Figure I.3 (d) is an image of Si NW arrays obtained by etching [23].

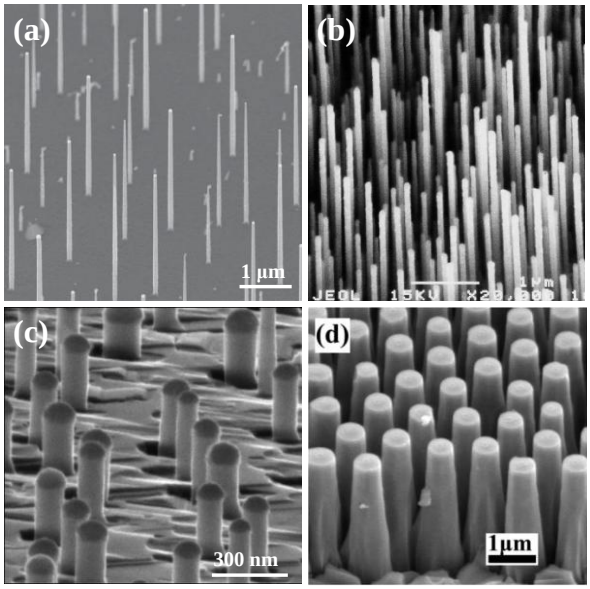

Figure I.3 – Scanning electron microscopy images of several types of Si NWs fabricated from different growth methods. (a) Si NWs grown from CVD method (1 h at 600 ℃ in a 20% disilane and 80% He solution at a pressure of 6.65 × 10^{-4} mbar [20]). (b) Vertically aligned, diameter-controlled Si NWs grown from ordered Au dots on Si (111) substrates via porous anodic alumina mask [21]. (c) Si NWs grown on a Si (111) substrate using MBE method [22]. (d) Si NW arrays obtained by etching [23].

As far as the applications of Si NWs are considered, Si NWs can be applied in plenty of domains such as electronics, photonics and photovoltaics. The example of some of these applications of Si NWs will be given in the following parts.

I.2 Si nanowire synthesis approaches and their limitations

Si NWs are the typical one-dimensional nanostructures that may have specific dimensions (diameter or length) either at nano- or microscopic scales. Two different synthesis approaches may be considered. The "top-down" approach: downsizing from Si bulk to Si NWs and the "bottom-up" approach: auto-assembly of Si atoms into Si NWs.

I.2.1 "Top-down" approach

The "top-down" approach allows the fabrication of Si NWs from macroscopic materials (Si wafer). This approach has been employed in the domain of electronic for several decades. The traditional procedure based on this approach is the fabrication by lithography and etching. The electronic industry production is based on this approach. However, the minimal size of nanostructures that may be achieved following this approach is limited by the thinness of the etching process masks and the optical projection. By using this approach, the manufacturing costs will increase greatly with the components' size shrinks towards nano scale. There are several techniques based on this approach to fabricate Si NWs, for example: the electron-beam lithography combined with etching [24, 25], the metal particles-assisted etching [26], the nanoimprint lithography [27] and the conventional micro fabrication [28]. Considering the lithography process, there are two main processes, namely, photolithography and electron-beam lithography. The fabrication cost using photolithography is relatively low. However, it does not easily allow elaborating nanostructures with diameter smaller than 1 μm. If we consider now the electron-beam lithography with high resolution (diameter smaller than dozens of nanometers), its high cost is a strong handicap for its on-line industrial application. In this work, the "top-down" Si NWs were produced with an effective and low cost method combining Langmuir-Blodgett (LB) assembly and Reactive Ion Etching (RIE). This procedure is based on methods described in the literature [23, 29] and is illustrated on Figure I.4. Three steps are involved in this process. Step one (Figure I.4 (a)): deposition of a mono-layer of SiO_2 nanoparticles (as the etching mask) by LB on a Si-wafer. The diameter of nanoparticles and the spacing between them are important parameters which can be controlled and modified by isotropic RIE of SiO_2. It is indeed a way to monitor the diameter of Si NWs and their inter-spacing. Step two (Figure I.4 (b)): anisotropic etching of Si wafer into Si NWs by Deep Reactive Ion Etching (DRIE). Compared to RIE, Si NWs fabricated by DRIE have a length of several micrometers. Step three (Figure I.4 (c)): removal of the residual mask (SiO_2

nanoparticles) by hydrofluoric acid (HF) etching. The typical diameter and length of Si NWs elaborated from this method are hundreds of nanometers and several micrometers, respectively. The inter spacing between NWs is about few hundreds of nanometers.

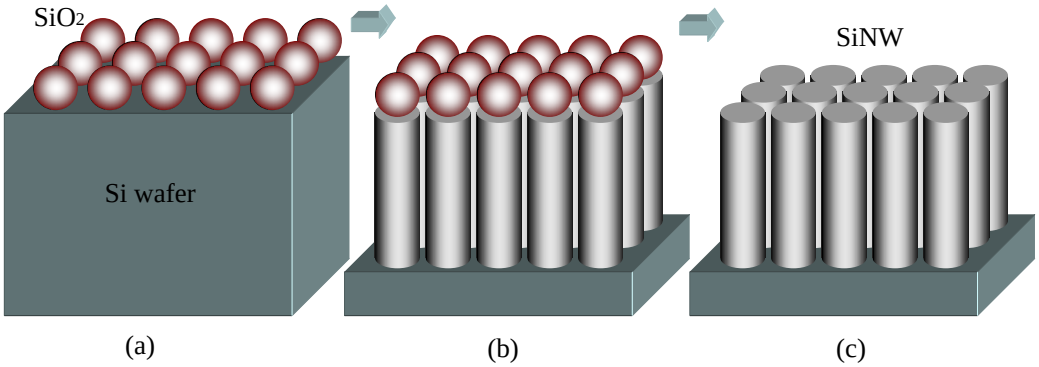

Figure I.4 – Schematic illustration of a micro fabrication process of Si NWs. Three steps are involved in this procedure. (a) Step one: deposition of a mono layer of SiO_2 nanoparticles by the Langmuir-Blodgett technique on a Si wafer. (b) Step two: anisotropic etching of Si into NWs by deep reactive ion etching. (c) Step three: removal of SiO_2 nanoparticles by hydrofluoric acid etching.

I.2.2 "Bottom-up" approach

The "bottom-up" approach for Si NW fabrication is a self-assembly process using Si atoms. The "bottom-up" approach is suitable to make smaller Si NWs than via the "top-down" approach and it can also reduce the fabrication costs. The smallest Si NW elaborated until now shows a diameter of 1.3 nm [30]. However, the synthesis of Si NWs with this approach is very complex and difficult to control. Different mechanisms for "bottom-up" growth of Si NWs are proposed in the literature. For example, Vapor-Liquid-Solid (VLS) mechanism [31-35], Solid-Liquid-Solid (SLS) mechanism [36-39], Vapor-Solid-Solid (VSS) mechanism [40, 41], electrodeposition mechanism [42], Self Catalytic Growth (SCG) mechanism [43, 44] and Oxide-Assisted Growth (OAG) mechanism [45-48]. In this work, VLS and SLS mechanisms are applied to grow Si NWs. These two mechanisms will be described in the next paragraph.

I.2.2.1 Vapor-Liquid-Solid (VLS)

The VLS mechanism is widely used. Although this mechanism has been described more than forty years ago [31], the number of research on its basic understanding and applications increased extensively during these last two decades. Two steps are involved for

NW fabrication in this mechanism. Step one is the deposition of catalyst droplets on a substrate. Step two is the introduction of Si atoms, coming from a gas like silane or from the evaporation of Si bulk, into the catalyst heated at a given temperature. Several experimental methods such as CVD [20], plasma enhanced CVD [49, 50], MBE [51], Electron Beam Evaporation (EBE) [52] and Chemical Beam Epitaxy (CBE) [53] have been developed based on the VLS mechanism. According to this mechanism, the Si NW growth can be sketched as in Figure I.5. This growing mechanism involves three contributions of Si atoms: Si atoms as holder (Si^H), Si atoms as provider (Si^P) and Si atoms as receiver (Si^R). Si^H are atoms from the substrate that hold Si NWs and are usually chosen as Si [111] [54] or Si [100] [55] oriented wafers. Si^P are Si atoms provided to the system and usually from gas like SiH_4 [54, 56], Si_2H_6 [57, 58], $SiCl_4$ [31, 59] or from Si bulk [51, 60]. Si^R are atoms from a metallic alloy (catalyst + Si) that will accept or receive additional (supersaturation) Si atoms. The catalyst is often chosen as Au [61, 62], Al [63-65], Cu [66, 67], Ti [68, 69], Fe [32], Pt [70] and catalyst-free at specific condition [71]. Before Si NW growth, Si^R exist on Si^H when the system is heated in the growth chamber, at, for example, 500 ℃. Si^P is then introduced into the chamber. The growing mechanism relies then on a three-step process: 1) Si atoms are produced from the decomposition of Si^P gas; 2) Si atoms produced from the gas decomposition are introduced into the catalyst (Si^P atoms becomes Si^R) and 3) the excess of Si atoms in the catalyst crystallizes at the interface with Si^H. A single Si NW or a carpet of Si NWs can thus be grown at the surface of Si^H.

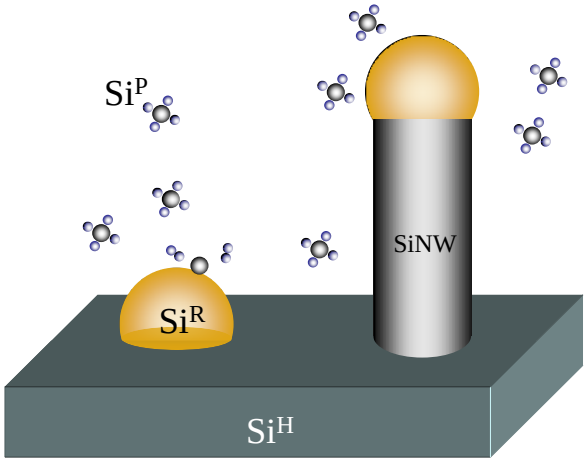

Figure I.5 – Schematic view of the VLS mechanism for the Si NW growth. This mechanism involves three states of the Si: solid state for Si atom holder (Si^H- the substrate), Si atom receiver (Si^R- supersaturated liquid-solid alloy) and Si atom provider (Si^P- Si-based gas)). Si^P atoms coming from the decomposition of the gas are incorporated into droplet (Si^R) and then crystallize at the interface of Si^R and Si^H.

In conclusion, the VLS mechanism is the key mechanism for NW growth. The advantage of VLS mechanism as a "bottom-up" approach is its variability to fabricate the intended NW size. Compared to other mechanism, the doping of NW synthesized by the VLS mechanism can be easily realized. The inconvenient of this mechanism is its difficulty to control the NW growth effectively due to the complexity of NW growth. In this work, two VLS mechanism-based growth methods, namely, CVD and MBE are used and will be described in the chapter II.

I.2.2.2 Solid-Liquid-Solid (SLS)

The SLS mechanism is also a process involving three steps as in the VLS mechanism. These steps are illustrated in Figure I.6 [38]. Step one (Figure I.6 (a)) is the formation of catalyst droplets (e.g. In or Sn) on an Indium-Tin-Oxide (ITO) substrate, for example. Step two (Figure I.6 (b)) is the deposition of a thin amorphous Si:H (a-Si:H) layer with a typical thickness in the range of 20 to 50 nm. Step three (Figure I.6 (c)) is the heating of the specimen at a given temperature. This promotes the growth of the Si NWs on the ITO substrate (not perpendicular as in the VLS mechanism). The liquid catalyst droplet leads the in-plane NW by consuming and transforming the surrounded thin a-Si:H layer. The driving force for the Si NW growth is the chemical potential difference between the a-Si:H layer (E_a) and the crystalline Si NW (E_c) with $E_a - E_c = 0.12 \sim 0.15$ eV owing to references [72, 73]. The catalyst droplets "adsorb" Si atoms from the amorphous layer and "desorb" a crystalline Si structure (NW) at its back interface.

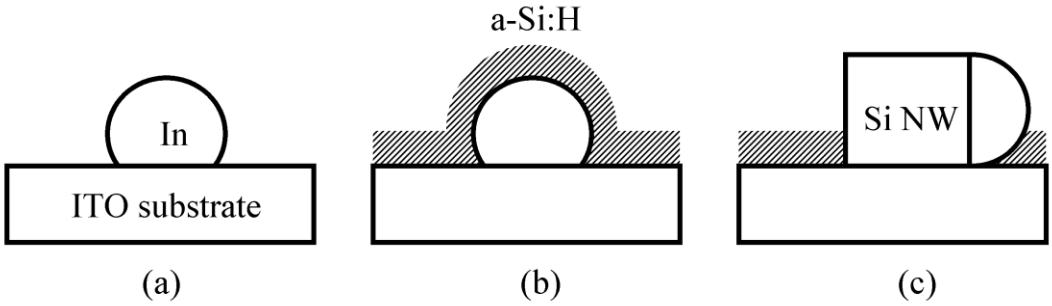

Figure I.6 – Schematic illustration of a Si NW grown by solid-liquid-solid mechanism. Three steps are involved in this mechanism. (a) Step one: preparation of catalyst droplet (e.g. In) on Indium-Tin-Oxide (ITO) substrate. (b) Step two: deposition a thin amorphous Si:H layer with a typical thickness between 20 ~ 50 nm. (c) Step three: heating the specimen at a given temperature.

As a conclusion, the NW size from this mechanism can also been controlled as in the VLS case. Moreover, this growth mechanism provides the new opportunity of large scale integration of two-dimensional NW-based planar devices. The experimental instrument concerning this mechanism will be presented in chapter II.

I.3 Si nanowire applications

Semiconductor NWs exhibit good properties and can be chosen as candidates in lot of domains. Si NWs can be used alone as functional nanostructures in the domain of nanoelectronics such as transistors [2, 74, 75], sensors [76-78], batteries [79-81] and solar cells [29, 82]. Si NW can also be applied in transistors together with graphene [83, 84] or carbon nanotubes [85] and in solar cells together with carbon nanotubes [86] or with nanoparticles [87-89]. In this work, research focuses on Si NWs and it should be noted here that the studies will be restricted to the characterization of "a single" Si NW rather than Si NW "forest". The two main applications of Si NWs are given briefly in the following part.

The Metal-Oxide-Semiconductor Field-Effect Transistors (MOSFETs) are the elementary building blocks for electronics. It has been shown in the literature that the MOSFETs can be formed using Si NWs [90]. Figure I.7 (a) is the top view of a SEM image of 100 nm Si NW grown against the oxide surface between source (S) and drain (D). Figure I.7 (b) is the cross-section view of a TEM image of a Si NW with gate oxide and a top Ti gate electrode. It shows that Si NW is in contact with the oxide layer. The on-off current ratio (I_{on}/I_{off}), the inverse subthreshold slope (S), the mobility, and the threshold voltage (V_T) are electrically tested using this Si NW based MOSFETs. Figure I.7 (c) shows the drain (I_{DS} - V_{DS}) characteristics for $-1.35\ V < V_G < 0\ V$ and gate (I_{DS} - V_{GS}) characteristics at $V_{DS} = 0.1\ V$ for a two NWs device. The gate characteristics show I_{on}/I_{off} ratio of ~ 104 and an inverse subthreshold slope of ~ 155 mV/decade (Figure I.7 (d)). The high value of I_{on}/I_{off} ratio enables low energy consumption and the reasonable value of S shows the low interface state density.

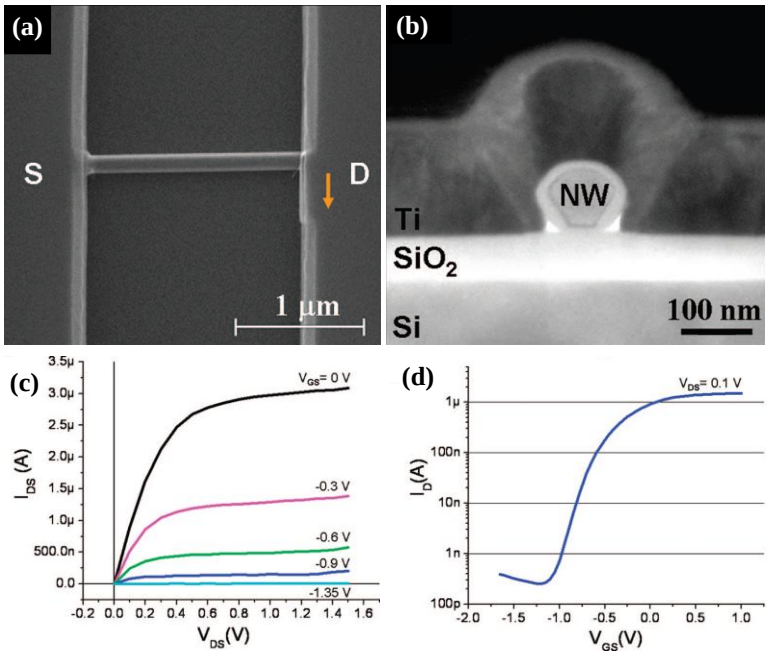

Figure I.7 – (a) Top view of a scanning electron microscopy image of a Si NW grown against the oxide surface between source (S) and drain (D) (b) Cross-section view of a transmission electron microscopy image of Si NW heterostructure. (c) Transistor characteristics of drain characteristics measured with gate voltages V_G from 0 to -1.35 V and the substrate at 0 V. (d) Transistor gate characteristics measured at drain voltage V_D = 0.1 V and the substrate at 0 V, showing I_{on}/I_{off} ratio of ~ 104 and inverse subthreshold slope of ~ 155 mV/decade. Adapted from [90].

Another example of Si NW application is the solar cell. The NW geometry, namely, the microscopic surface (used as photon collector) and the nanoscopic cross section (used as minority carrier collector), make NWs an excellent candidate for photovoltaic [91]. The first advantage of NW-based solar cell can be found in the anti-reflection property of an array of Si NWs that enhances the solar absorption [92, 93]. For photovoltaic applications, Si NWs are needed to be turn into p-i-n junctions with a doping process. Two geometries of dopant-modulated structures can be proposed: axial [94, 95] or radial [57, 96]. For axial p-i-n junctions, one possibility to modulate the doping structure is to switch the dopant precursor during the NW growth [97]. For radial p-i-n junctions, one possibility is the radial deposition of layer i and p by increasing the growth temperature and lowering the gas pressure after the growth of the n-type Si NW [94]. A SEM image of axial p-i-n Si NW is given in Figure I.8 (a) before and (b) after wet chemical etching [94]. For radial p-i-n Si NW, SEM images before and after wet chemical etching are presented in Figure I.8 (c) and (d) respectively [96]. The photovoltaic characteristics of axial and radial p-i-n Si NW are investigated at the standard

condition of one sun (100 mW/cm^2) with AM 1.5 G (Air Mass 1.5 Global)[1]illumination. Figure I.8 (e) is the current-voltage (I–V) curves recorded under illumination from axial p-i-n Si NW devices, with i length = 0 μm (red), 2 μm (green), and 4 μm (black). The illumination intensity is 100 mW/cm^2, AM 1.5 G. The result reveals a systematic improvement in V_{oc} and I_{sc} while increasing i-segment length [94]. Figure I.8 (f) is the dark and light I–V curves of a radial Si NW device [96]. The maximum output power for the single radial p-i-n Si NW is about 72 pW with an efficiency of 3.4 % at one sun illumination, whereas it is only 4.6 pW of maximum output power with an efficiency of 0.5 % for the single axial p-i-n Si NW. The reason, given by the authors, is that the minority carrier collection length for radial p-i-n Si NW is much shorter than for axial p-i-n Si NW. In the radial p-i-n Si NW, the photon collection direction and the minority carrier collection direction are orthogonal. An efficiency of 11 % for Si NW based solar with radial junction cell can be achieved according to the theoretical calculation [98]. The radius of Si NWs should not exceed the minority carrier diffusion length (the average distance that the electron-pair can diffuse before their recombination). The diffusion length is given by the relation of $L = \sqrt{D\tau}$, where D is the diffusion constant and τ is the recombination lifetime [99]. τ is inverse to the Si trap density. The diffusion length can vary from several hundreds of nanometers to several micrometers or even millimeters according to the trap density. From a diffusion length point of view, it is not necessary to elaborate Si NWs with very small diameter for solar cells. It should be noted here that NW light absorption has large dependence on incident light angle and NW diameter (NW with small diameter absorbs shorter wavelength whereas NW with large diameter absorbs higher wavelength [100]. Moreover, there is photonic coupling between the neighboring Si NWs [101]. Due to these phenomena, it is important and necessary to control precisely the diameter and density of NWs.

[1] One sun is equal to be the irradiance of one solar constant which is defined as the irradiance of the sun on the outer atmosphere at a distance of one astronomical unit.

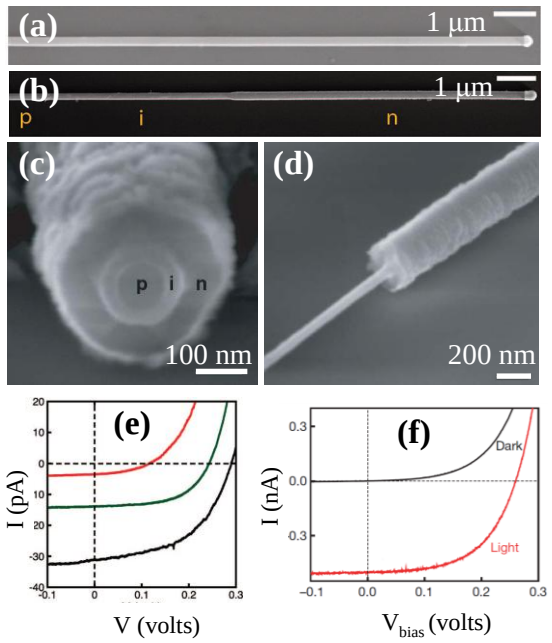

Figure I.8 – Scanning electron microscopy images of p-i-n axial Si NW (a) before and (b) after wet chemical etching. Scanning electron microscopy images of p-i-n radial Si NW (c) before (cross-section view) and (d) after wet chemical etching. (e) I–V curves recorded under illumination from an axial p-i-n Si NW, with i length = 0 µm (red), 2 µm (green), and 4 µm (black) devices with illumination intensity of 100 mW/cm^2, AM 1.5 G. (f) Dark and light I–V curves recorded from a radial Si NW device. Adapted from [94, 96].

Considering the application of Si NWs, the individual Si NWs can be designed into a transistor by a wrapped-around gate [102, 103] or transferred from the substrate and integrated as the functional building block for nano device. As the Si NWs are considered to be the building block, "to harvest" Si NWs is also a key factor for the mass production, especially for Si NWs grown by VLS mechanism. In the recent years, several harvest and integration techniques have been proposed and the NW-based electrical devices have been manufactured with mass production, for example, the Langmuir-Blodgett [104, 105], the ac electric fields [106], the optical trapping [107, 108], the bubble film [109], the contact printing [110], the knocking down approach [111], the dielectrophoresis [112] and the vertical transfer by crack formation [113].

I.4 Basic concepts for Si nanowire growth

The formation of Si NWs by the "bottom up" approach is a more complicated process compared to the "top-down" approach. In this section, the formation of Si NWs from the "bottom-up" approach, namely, Si NW growth is studied. From the large experimental feedback, when NW growth is investigated, several important aspects such as the nucleation in catalyst droplet [114, 115], the NW growth direction [116, 117], the evolution of the catalyst droplet form [118, 119], the sidewall surface [120, 121], the NW surface density [122, 123], the kinking [124] and the NW growth rate (length) [125-127] can be considered. Although numerous works, from theory to experience, have been done in recent years concerning these aspects, the NW growth processes are still not fully understood. In this section, these aspects are briefly presented and they will be developed in the different models when needed in this work. When a Si NW is growing, either via VLS or SLS mechanisms, three different phases are involved. Among these phases, the liquid phase (the heated catalyst droplet with excess of Si atoms) is the dominant one. It can greatly influence the NW growth. For example the catalyst droplet influences the NW diameter [128] and its evolution during growth [126, 129], the diffusion of metallic atoms can induce the faceting of the Si NW sidewall [130] and the growing direction of the NW is somewhere under the influence of the droplet surface energy [131].

I.4.1 Nucleation of Si atoms in catalyst droplet

Nucleation is the process of formation of nuclei attracting more atoms to precipitate. It is defined as the formation of a new thermodynamic phase. In the VLS system, after exposing the pre-deposited catalyst droplets (Au in our case) to the Si atmosphere (Si atoms coming from the decomposition of the Si precursors such as silane or the evaporation of Si atoms from Si bulk), Si atoms can incorporate the catalyst droplet (at 363 ℃) and form the eutectic liquid alloy $Au_{82}Si_{18}$ with Au atoms as shown in the conventional binary phase (illustrated in Figure I.9) [132].

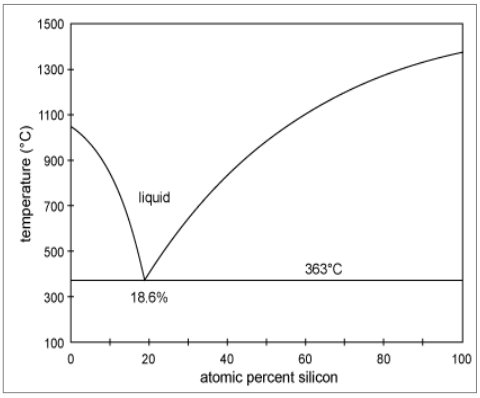

Figure I.9 – Phase diagram for Au-Si system. Adapted from [132].

It should be noted here that the equilibrium composition are extracted from the equilibrium phase diagram. However the nanoscale dimensions of the droplet (small volume, small curvature, large surface) may modify the position of liquidus and solidus lines from the phase diagram [133-135]. With the continuous adsorption of Si atoms into the Au-rich droplet, and thus, the increases of the Si supersaturation, nucleation occurs at the liquid/solid inter phase (substrate or NW). Three types of nucleation process can be found in the literature [136]: Volmer-Weber (island formation), Frank-van der Merwe (layer-by-layer) and Stranski-Krastanov (layer-plus-island). In the case of Si NW, nucleation is believed to follow the layer-by-layer growth as suggested in references [115, 137, 138]. Whatever is the model, the knowledge of the location where the first nuclei appears is also very important. The calculation shows that the heterogeneous nucleation on the Three Phases Boundary (TPB) or triple line is preferential. It, indeed, lowers the formation energy of nuclei [139, 140]. It is also experimentally found that the first nucleus occurs at TPB using the *in-situ* TEM [114, 135, 141]. Figure I.10 shows *in-situ* TEM images of Si precipitation in a Au-rich droplet. These pictures are extracted from a video at separate times: 0s, 65s and 84s [114]. Figure I.10 (a)-(c) shows respectively the Au droplets before the incorporation of Si atoms, the Au-rich droplets during the incorporation and the nucleation of Si atoms at the TPB (this is evidenced with arrows on Figure I.10 (c)). The crystalline Si precipitation initiated at the TPB grows along the interface of the droplet and the substrate. The accumulation of these crystalline layers leads to the Si NW growth. In the case of SLS mechanism, the location of the first nucleus is also at the TPB as reported in the literature [142].

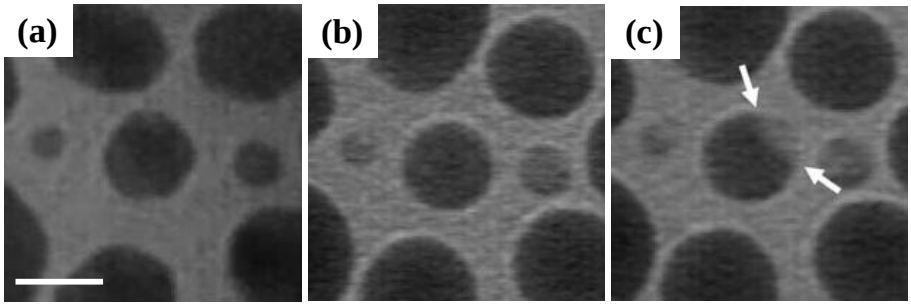

Figure I.10 – Transmission electron microscopy images of the nucleation of crystalline Si from Au particles. The scale bar is 10 nm. (a) Au particles before introducing the precursor (b) Formation of the liquid Au/Si alloy acquired after 65 s. (c) Appearance of a Si nucleus at the three phase boundary of droplets acquired after 84 s. Adapted from [114].

I.4.2 Migration of atoms from catalyst droplet

During the VLS growth mechanism, it is a common phenomenon that the volume of the catalyst droplet changes during the NW growth. First of all, before the addition of precursors, the heating of the substrate initiates the Ostwald ripening process [143, 144] that influence the size distribution of the droplets. Also, the growth of Si NWs is always accompanied by the surface migration of catalyst atoms. Au atoms from the Au catalyst droplet can migrate toward sidewall and substrate [35, 145-148] or migrate from the smaller catalyst droplet on the top of a NW to a bigger one on the top of another NW [20, 149]. The atom migration from the smaller catalyst droplet to the bigger one during Si NW growth has been investigated using the *in-situ* TEM experiment [20]. Figure I.11 are images of *in-situ* TEM experiment recorded at different times (a) 14.540 s, (b) 16.640 s and (c) 17.060 s. The volume of catalyst droplet labeled as A increases, whereas the volume of catalyst droplet labeled as B decreases and disappears eventually. The Au surface migration during Si NW growth is a very complicated process and it is still studied intensively. It is shown that the Au surface migration can be effectively inhibited by changing the experimental growth conditions such as the precursor pressure [150], the total pressure [151], the NW number density [152] and the addition of oxygen [153].

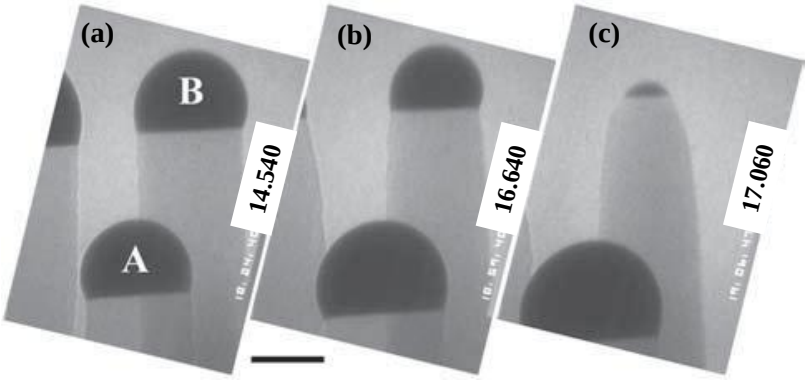

Figure I.11 – In-situ transmission electron microscopy images of Au catalyst droplets. Their volumes evolve during the NW growth. The three pictures are recorded at three different times (a) 14.540 s, (b) 16.640 s and (c) 17.060 s. The volume of catalyst droplet labeled as A increases, whereas the volume of catalyst droplet labeled as B decreases and disappears eventually. The scale bar is 50 nm. Adapted from [20].

I.4.3 Growth direction

The NW growth direction (crystal orientation) is a very important factor because of its influence on the electrical and optical properties [15]. Lots of experimental conditions affect Si NW growth direction, for example: the NW diameter [131] and the gas pressure during the growth process [154]. Considering the diameter-dependent growth direction, it is shown that for the Si NW with diameter D > 20 nm, 10 nm < D < 20 nm and D < 10 nm, the dominant Si NW growth directions are [111], [112] and [110] respectively [131]. This is the result of the minimization of free energies of the droplet/NW interface and NW interfacial edge [155]. According to the literature [155], the free energy F can be expressed in terms of the NW edge tension and the droplet/NW interfacial tension: $F=\varepsilon C+\sigma_{ls}S$. The edge tension $\varepsilon=\sigma_s\Delta z$ is given by the Si surface tension with Δz being the interfacial thickness on the Si side, C is the NW circumference, σ_{ls} is the droplet/NW interfacial tension and S is the interfacial area. Si NWs can be grown with the combination of several growth directions by controlling the experimental conditions. The kinked Si NWs with equal arm segment length grown out of plane by VLS is shown in Figure I.12 (a). This kind of structure is realized by changing the Si composition in the Au catalyst droplet during the NW growth [156]. Figure I.12 (b) is the kink Si NWs grown in plan by SLS because of the energy competition between droplet/NW interface and liquid droplet surface [39].

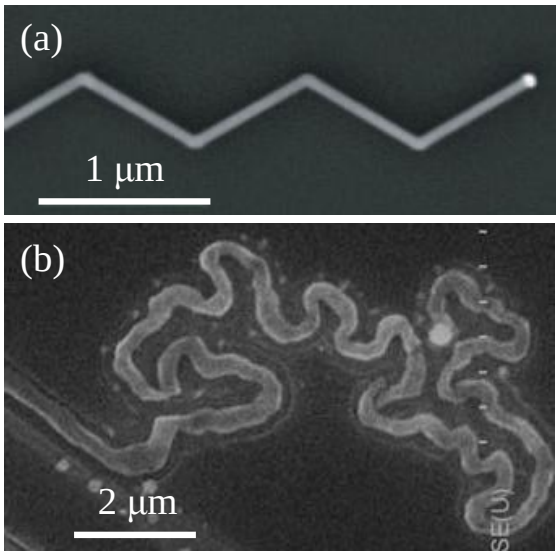

Figure I.12 – Scanning electron microscopy images of non linear Si NWs grown by (a) VLS mechanism and (b) SLS mechanism. Adapted from [156] and [37].

The kink of NWs normally should be avoided considering the integration of NW in the nano device. However, the kink of NWs provides the possibility of fabrication of the "self-labelled" two-dimensional NW structures if the kink can be controlled effectively.

I.4.4 Sidewall surface

In general, in order to simplify the growth modelling, the geometrical form of Si NW can be viewed as a cylinder (if no tapering occurs) or a cone (if tapering occurs), although the exact shape of the NW cross section is rather hexagonal depending on the NW growth direction [157] and growth temperature [158]. The geometrical form of a Si NW is complex and a specific attention must be paid to it. Indeed a NW shows a great surface to volume ratio and it affects the NW properties [159, 160].

The presence of contamination by catalyst atoms such as Au, for example, can on one hand, has deleterious effects on electrical properties of the NW due to the creation of deep level traps. Therefore, it must be avoided [161]. On the other hand, Si NW sidewall surface can be intentionally decorated with different kinds of nanoparticles, for example: the decoration with Pt nanoparticles for photovoltaic [89], the coverage with Ag nanoparticles for antimicrobial [162], DNA-coated surface [163] and all surface modification for medicinal application [164]. In these cases, the functionalization of the NW sidewall surface gives new properties to NWs.

Ideally, the sidewall surface of a Si NW is smooth without any surface defects. However, as far as one sidewall surface of Si NW is considered, it can exhibit facets [121, 165]. Si NW sidewall surface can exhibit a saw tooth facet at high growth temperature and under high vacuum. One of the possible reason for this saw tooth facet formation is the change (widening or narrowing) of the TPB angle during NW growth [165], in other words, a change of the droplet shape. The existence of Au atoms on the Si surface is also the key factor for facet formation [166, 167] due to the formation of an Au-induced surface reconstruction. According to the model proposed in the literature [165], if the NW grows wider as shown in Figure I.13 (a), the Au-Si droplet will stretch thinner and meets the Si at a steeper angle (θ_d in Figure I.13 (a)). This introduces an inward force promoting the formation of a smaller drop diameter, creating thus a kink on the surface (Figure I.13 (b)). Conversely, as shown in Figure I.13 (b), decreasing the diameter of the NW produces an outward force, promoting the formation of larger facet (Figure I.13 (c)). The alternation of this phenomenon gives rise to the saw tooth facets.

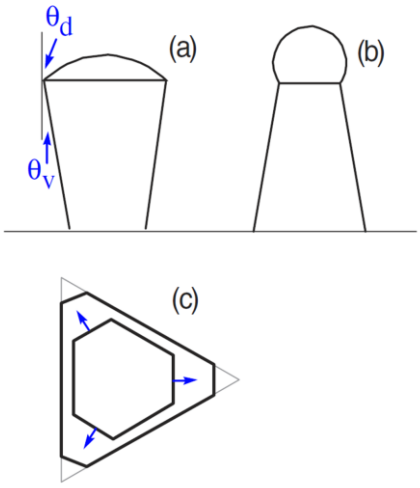

Figure I.13 – Schematic illustration of facet modeling. Adapted from [165].

A model, taking into account these effects has been derived by Ross [165]. The change of the free energy (dE) per unit of length of NW (dZ) can be given by the following expression:

$$\frac{dE}{dz} = L\xi + \Psi$$

where ξ is the supersaturation of Si in the droplet during the NW growth and

$$\Psi = \frac{\gamma_v}{\cos\theta_v} + (\gamma_d \sin\theta_d + \gamma_i)\sin\theta_v$$

is the surface energy contribution. L is the total length of the NW, ν is an index marking the

various stable facets, γ_ν is the surface energy of the facet ν and θ_ν its angle (as described in Figure I.13), γ_d is the surface energy of the droplet and θ_d its contact angle, γ_i is the interfacial energy between the droplet and the NW. Close to equilibrium, the NW growth will occur for the most energetically favorable facet, that is to say corresponding to the minimization of Ψ. For a widening wire ($\theta_\nu > 0$, as in Figure I.13 (a)), the angle θ_d and hence Ψ increase as the wire grows. While this raises Ψ when ν is a widening fact, it lowers Ψ for a narrowing facet. Eventually, the facet having $\theta_\nu < 0$ will become more favorable. Then the new facet is introduced, and the NW thereafter becomes narrower as it grows, until the growth process is reversed.

I.4.5 Growth rate (length)

The growth rate (dL/dt with L the length of the NW) of NWs is important to control for their use and integration in the different processes as described above. Several relations for the growth rate depending on experimental conditions have been found and reported in the literature, for example: the increase of growth rate with the diameter of the NW for CVD-grown Si NWs [125, 168, 169], its decrease with NW diameter for MBE-grown Si NWs [51], temperature dependence [170] and increase with growth pressure [171]. Several models are proposed to study these phenomena. For example, thermally activated self-diffusion model [172, 173], gradient of chemical potential model [174] and pressure-involved model [169]. These models will be described and used or modified in the chapter III for purpose of this work.

I.5 Doping of Si nanowire

I.5.1 General concepts

Doping can be defined as the process to introduce impurities into intrinsic semiconductor materials, such as Si, in order to change and control their electrical properties. Doping Si crystal increases its number of free charges (free electrons (e^+) for the so called n-type Si and free holes (h^+) for the p-type Si) that can be "moved" by applying an external voltage. There are two different types of doping, namely, positive type (p-type) and (negative type) n-type. As Si belongs to the group IV elements, elements of group III such as B, Ga and In can be chosen as the p-type doping source. This is illustrated on Figure I.14 (a). Similarly, for n-type doping of Si, the dopant can be chosen from the elements of group V such as P and As (Figure I.14 (b)).

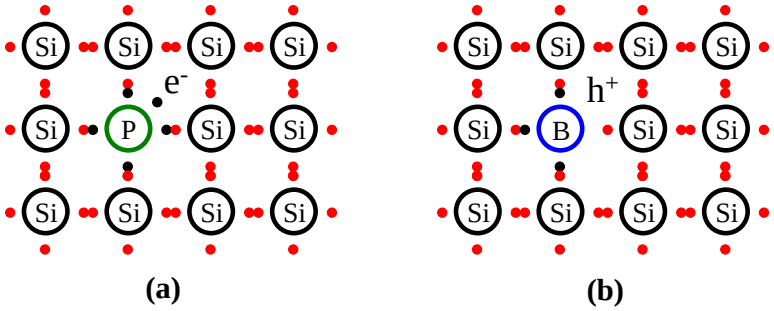

Figure I.14 – Schematic illustration of (a) n-type and (b) p-type doping of Si using P and B as electron donor (e^-) and hole acceptor (h^+) respectively.

As indicated in paragraph I.2, there are two types of Si NWs, namely, Si NWs fabricated by "top-down" and "bottom-up" approaches. The doping of the "top-down" Si NW can be easily realized when the substrate is already doped before lithography. When considering the Si NWs grown by "bottom-up", two doping methods can be applied, namely, the "*ex-situ*" ion implantation [95] and the "*in-situ*" doping during Si NW growth [175]. One can note that the ex-situ doping can also be applied to the "top-down" NWs when elaborated from intrinsic Si. For ion implantation, different ions such as B or P ions can be chosen for Si NW doping [176]. It must be noted that using this process a specific isotope of the chemical specie is implanted in the system. For the realization of doping during Si NW growth, a dopant "provider" (dopant precursor or dopant layer) can be used. For example, concerning p-type Si NW doping, one can choose diborane [177, 178] or trimethylboron [179, 180] and for n-type Si NW doping, one can chose phosphine [181, 182], arsenic [183] and indium (which also serve as the growth catalyst) [37]. The metrology of dopants of NWs will be a part of this work.

I.5.2 Characterization techniques

The information about dopant concentrations and their distributions in semiconductor NWs are necessary when one wants to identify which incorporation pathway is dominant during semiconductor NW doping process. In order to characterize dopants in semiconductor NWs, several techniques can be used. For example, the Kelvin probe force microscopy [184, 185], the Raman spectroscopy [186, 187], the electrical measurement [188-190], the electron holography [191], the atom probe tomography [192-195], the electrodeless Time-Resolved Microwave Conductivity technique (TRMC) [196] and the scanning photocurrent microscopy [197]. All these techniques are applied for characterization of dopants in individual NW

except the TRMC technique. In the following part, three representative techniques including: i) Kelvin probe force microscopy, ii) Electrical measurement and iii) Atom probe tomography are briefly presented. These three techniques are widely used to characterize the dopant in semiconductor materials. The techniques i) and ii) only characterize the active dopants in NWs, whereas, the technique iii) characterize all dopants (active or not) in NWs. It should be also noted here that techniques i) and iii) are destructive techniques.

I.5.2.1 Kelvin probe force microscopy

Kelvin Probe Force Microscopy (KPFM) is a noncontact variant of the Atomic Force Microscopy (AFM). It can determine quantitatively the specimen surface potential in non-conducting materials and the work function in conducting materials with a nanometer resolution. KPFM is based on AFM setup and the Kelvin method. The Kelvin method measures the surface potential in non-metals and the work function in metals. A Contact Potential Difference (CPD) between the tip and specimen can be created due to the difference of Fermi level. The Kelvin method works on the principle of applying an external voltage to balance CPD which is equal to the work function or the surface potential. For measuring the radial potential of a single n-type Si NW, KPFM needs to conduct the measurement of work function of Si NW sidewall layer-by-layer [185]. In order to do so, a Si NW sidewall surface treatment process is involved, namely, conformal wet chemical etching of NW. Figure I.15 (a-d) is the cross-section and top view of one portion of Si NW during etching. The potential difference then can be measured before and after etching. Figure I.15 (e) shows the calculated radial phosphorus profile for $D = 1 \times 10^{-15}$ cm^2/s (solid line) and simulated current density (symbols in the graph and inset image) for a NW under a bias voltage of 0.1 V. The radial P concentration profile decreases with of almost two orders of magnitude from the NW surface to its core for a Si NW without tapering. It should be noted here that only the active dopants in Si NWs can be measured using this technique. An advantage of KPFM is that it ensures almost zero tip-induced band bending. The potential maps on a very small surface can be obtained which allows the characterization with high resolution. Moreover, the maps can be easily interpreted in comparison to the pure spectroscopic method such as Raman. The resolution is similar to the AFM with about 1 nm laterally and 0.1 mV. This technique can be also applied to measure the potential profile of biased p-n junction and map the defects in carbon nanotubes [198]. The disadvantage of this technique is that it can not be used in the biological relevant condition.

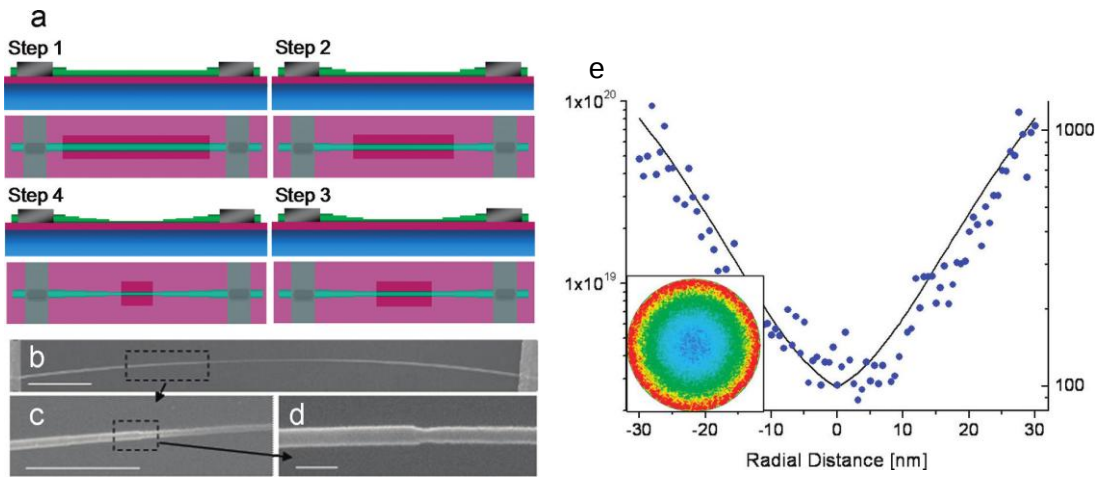

Figure I.15 – (a) Schematic illustration of four etching steps. (b)-(d) The scanning electron microscopy images of the NW after the etching steps. The scale bars are 1 μm, 1 μm and 100 nm respectively. (e) Calculated radial phosphorus profile for D = 1 × 10^{-15} m^2/s (solid line) and simulated current density (symbols in the graph and inset image) for a NW under a bias voltage of 0.1 V. Adapted from [185].

I.5.2.2 Electrical measurement

The information about active dopant in Si NWs can also be obtained by measuring the electrical transport properties. In order to apply this to a NW, a conformal layer-by-layer removal of Si from the Si NW must be performed just as in the case of KPFM measurement. The assessment of active dopant in Si NWs can be realized by electrical measurement using this layer-by-layer removal technique [189]. The electrical measurement for individual NW can also be done with the capacitance-voltage (C-V) technique without the involvement of NW material removal [190]. The C-V technique uses a p-n junction (device) to create a depletion region with its ionized charges inside behaving as a capacitance. The depletion width can modulate by changing the voltage applied. The dependence of depletion width on the applied voltage can provide the information such as doping profile, carrier lifetime and active defect density. The dopant (B) profile of NW can be extracted from the high frequency C-V curve. Figure I.16 is the radial B profile for an individual Si NW [190]. N_a-diffusion represents the simulated boron diffusion profile owing to the experimental doping condition. The associated majority carrier distribution can be calculated from the dopant profile using the finite element modeling electrostatic simulations (Comsol Multiphysics). p(r)-simulation and p(r)-experimental represent the extracted majority carrier profile from the ideal and experimental C-V curve. It can be seen from Figure I.16 that a very low concentration

detection limit can be achieved (≈ 10^{17} at./cm^3) using this technique. The disadvantage of this technique for measuring NW doping profile is that there is the influence of the device contact. However, this technique can be used to study the effect of contact on NW electrical property.

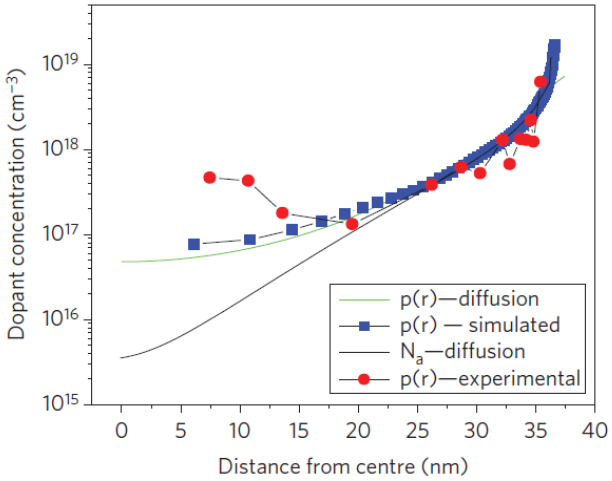

Figure I.16 – Radial B profile. The red circles represent the radial B profile which is extracted from the capacitance-voltage curve. The blue squares are the carrier concentration extracted from the theoretical capacitance-voltage curve. The black and green curves represent the B diffusion profile from simulation and the majority carrier redistribution from calculation. Adapted from [190].

I.5.2.3 Atom probe tomography

The principle of the APT is based on the field evaporation of atoms. A conventional APT is based on the basic principle that an atom can be evaporated from a specimen surface with the use of a high voltage (HV) pulse: this is the field evaporation. However, for a bad conductive material such as semiconductor NWs, the HV could not be effectively transmitted to the specimen tip. Thus, another energy source except HV is needed to create a sufficient evaporation field and assist the evaporation. The semiconductor material can be successfully evaporated with the assistance of a femtosecond laser. This is the so called laser-assisted APT. The laser-assisted APT is a three dimensional high resolution analytical microscope that can map the distribution of atoms in materials at the atomic scale. The laser pulse frequency triggers the evaporation of atoms from the surface of the specimen towards the position sensitive detector. Measuring the time of flight of individual atoms allows the identification of the chemical nature of evaporated ions and their impact positions on the detector allows calculating their initial position at the surface of the specimen. This information is used for

the three dimensional reconstruction of the material at the atomic scale. A detailed description of laser-assisted APT will be given in the experimental technique of chapter II.

The laser-assisted APT has been recently applied successfully for the investigation of P-doped Ge NWs grown by CVD method using Au, GeH_4 and PH_3 as catalyst, precursor and dopant reactor respectively [194]. Ge NWs are grown on micro pillar array substrates fabricated from high conductivity Si (111) wafers using a deep reactive ion etching process. Figure I.17 (a) shows a SEM image of p-type Ge NW with very high tapering effect. It should be pointed here that this kind of NWs with very big tapering effect is intentionally grown at low growth pressure and high growth temperature for APT investigation. In the inset of Figure I.17 (a) the Au catalyst droplet can be seen at the tip of the Ge NW. Figure I.17 (b) displays the reconstruction of a p-type Ge NW with a Au droplet on the top. Au, Ge and P atoms are presented in yellow, blue and gray dots respectively. Figure I.17 (c) shows the radial plot of P concentration for Ge NW grown at 380 °C and PH_3:GeH_4 ratios of 1:1000 (triangles) and 1:500 (squares). A higher NW shell phosphorus concentration can be found compared to its core value. This technique has been intensively used in this present work. The details of the advantages and disadvantages will be given in chapter II.

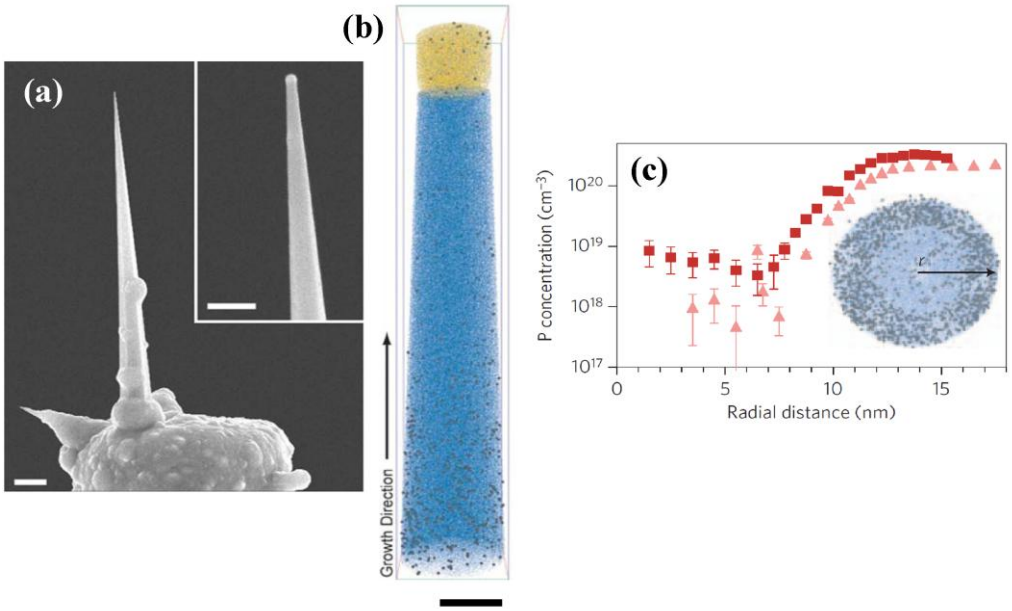

Figure I.17 – (a) Scanning electron microscopy image of p-type Ge NW with very high tapering effect grown on a silicon micro pillar for APT studies. The scale bar is 1 µm. The Au catalyst droplet can be seen at the top of Ge NW as shown in the inset of Figure I.17 (a). The scale bar is 200 nm. (b) Three dimensional reconstruction of p-type Ge NW. Au, Ge and P atoms in Ge NWs are represented by yellow, blue and gray dots respectively. The scale bar is 20 nm. (c) Radial phosphorus concentration profile for Ge NW grown at 380 °C and

PH_3:GeH_4 ratios of 1:1000 (triangles) and 1:500 (squares). The inset shows concentration measurement path. Adapted from [194].

All the three techniques above are able to give information on the dopant in NWs. However, the information is different and often complementary. The first two techniques (KPFM and electrical measurement) give indirect evidence of the dopant distribution. For example, the KPFM characterization of NW is the measurement of the work function which is relevant to the doping in NW. The electrical measurement is based on the measurement of capacitance relevant to dopant density in NW. Compared to other techniques, APT can provide a clear picture of the dopant (active or not) and impurity distribution in NW. Moreover, the APT characterization can be conducted on an as-grown NW.

I.6 Conclusion and scope

Si NWs are typical one-dimensional semiconductor nanostructures and they have been studied extensively in the very recent years. It is believed that Si NWs can be chosen as future candidates in many domains such as electronics, sensors and photovoltaics because they exhibit lots of new or enhanced properties compared to Si bulk. For example, the photon adsorption is enhanced in Si NW-based solar cell compared to planar structure. As far as the application of Si NWs is considered, it is an important and necessary issue to understand and control effectively the Si NW growth as well as Si NW doping. A large number of research works has been done since the discovery of VLS mechanism by Wagner and Ellis in 1964. Si NWs are investigated from different aspects concerning the individual Si atom behaviour (e.g. the nucleation in catalyst droplet), the single Si NW (e.g. the sidewall surface) and the entirety of Si NW (e.g. photon adsorption). However, there are still several aspects that are not fully understood. This present work is realized at these backgrounds and it is divided into two parts. The first part is the investigation of growth rate and morphology of NW synthesized at different conditions. The second part is the incorporation mechanisms of impurities (catalysts and dopants) in Si NWs from different mechanisms (etching, VLS and SLS), different structures (p-type and n-type) and different catalysts (Au and In). As far as the impurity characterization is considered, the impurity metrology in individual Si NWs is performed by APT. It should be noted here that HRTEM (collaboration with other laboratories) is used as the coupling technique to compare the results with APT. The APT results provide the

information of concentration and distribution of dopant in NWs. Meanwhile, the HRTEM results provide the atomic structure of NWs.

Bibliography of chapter I

[1] R. Rurali, Rev. Mod. Phys., 82, 427 (2010)
[2] J.-P. Colinge, C.-W. Lee, A. Afzalian, N. D. Akhavan, R. Yan, I. Ferain, P. Razavi, B. O'Neill, A. Blake, M. White, A.-M. Kelleher, B. McCarthy, and R. Murphy, Nat. Nanotechnol., 5, 225 (2010)
[3] R. Yan, D. Gargas, and P. Yang, Nat. Photonics, 3, 569 (2009)
[4] R. He, and P. Yang, Nat. Nanotechnol., 1, 42 (2006)
[5] A. I. Hochbaum, R. Chen, R. D. Delgado, W. Liang, E. C. Garnett, M. Najarian, A. Majumdar, and P. Yang, Nature, 451, 163 (2008)
[6] M. Law, L. E. Greene, J. C. Johnson, R. Saykally, and P. Yang, Nat. Mater., 4, 455 (2005)
[7] Z. L. Wang, and J. Song, Science, 312, 242 (2006)
[8] C. Xu, X. Wang, and Z. L. Wang, J. Am. Chem. Soc., 131, 5866 (2009)
[9] L. Vayssieres, Adv. Mater., 15, 464 (2003)
[10] Z. W. Pan, Z. R. Dai, and Z. L. Wang, Science, 291, 1947 (2001)
[11] X. Wang, C. J. Summers, and Z. L. Wang, Nano Lett., 4, 423 (2004)
[12] Z. W. Pan, S. Dai, C. M. Rouleau, and D. H. Lowndes, Angewandte Chemie, 117, 278 (2005)
[13] X. Y. Kong, and Z. L. Wang, Nano Lett., 3, 1625 (2003)
[14] X. Y. Kong, Y. Ding, R. Yang, and Z. L. Wang, Science, 303, 1348 (2004)
[15] M. S. Gudiksen, L. J. Lauhon, J. Wang, D. C. Smith, and C. M. Lieber, Nature, 415, 617 (2002)
[16] C. Colombo, M. Heibeta, M. Gratzel, and A. Fontcuberta i Morral, Appl. Phys. Lett., 94, 173108 (2009)
[17] C. Soci, X.-Y. Bao, D. P. R. Aplin, and D. Wang, Nano Lett., 8, 4275 (2008)
[18] M. C. Plante, and R. R. LaPierre, J. Cryst. Growth, 286, 394 (2006)
[19] H. Shtrikman, R. Popovitz-Biro, A. Kretinin, and M. Heiblum, Nano Lett., 9, 215 (2008)
[20] J. B. Hannon, S. Kodambaka, F. M. Ross, and R. M. Tromp, Nature, 440, 69 (2006)
[21] I. Lombardi, A. I. Hochbaum, P. Yang, C. Carraro, and R. Maboudian, Chem. Mater., 18, 988 (2006)
[22] N. D. Zakharov, P. Werner, G. Gerth, L. Schubert, L. Sokolov, and U. Gösele, J. Cryst. Growth, 290, 6 (2006)
[23] C.-M. Hsu, S. T. Connor, M. X. Tang, and Y. Cui, Appl. Phys. Lett., 93, 133109 (2008)
[24] K. Trivedi, H. Yuk, H. C. Floresca, M. J. Kim, and W. Hu, Nano Lett., 11, 1412 (2011)
[25] K. Seo, M. Wober, P. Steinvurzel, E. Schonbrun, Y. Dan, T. Ellenbogen, and K. B. Crozier, Nano Lett., 11, 1851 (2011)
[26] J. Kim, H. Han, Y. H. Kim, S.-H. Choi, J.-C. Kim, and W. Lee, ACS Nano, 5, 3222 (2011)
[27] T. Martensson, P. Carlberg, M. Borgstrom, L. Montelius, W. Seifert, and L. Samuelson, Nano Lett., 4, 699 (2004)
[28] S. Chen, J. G. Bomer, W. G. van der Wiel, E. T. Carlen, and A. van den Berg, ACS Nano, 3, 3485 (2009)
[29] E. Garnett, and P. Yang, Nano Lett., 10, 1082 (2010)
[30] D. D. D. Ma, C. S. Lee, F. C. K. Au, S. Y. Tong, and S. T. Lee, Science, 299, 1874 (2003)
[31] R. S. Wagner, and W. C. Ellis, Appl. Phys. Lett., 4, 89 (1964)

[32] A. M. Morales, and C. M. Lieber, Science, 279, 208 (1998)
[33] S. Hoffmann, I. Utke, B. Moser, J. Michler, S. H. Christiansen, V. Schmidt, S. Senz, P. Werner, U. Gosele, and C. Ballif, Nano Lett., 6, 622 (2006)
[34] Y. Zhu, F. Xu, Q. Qin, W. Y. Fung, and W. Lu, Nano Lett., 9, 3934 (2009)
[35] P. Madras, E. Dailey, and J. Drucker, Nano Lett., 10, 1759 (2010)
[36] D. P. Yu, Y. J. Xing, Q. L. Hang, H. F. Yan, J. Xu, Z. H. Xi, and S. Q. Feng, Physica E, 9, 305 (2001)
[37] L. Yu, M. Oudwan, O. Moustapha, F. Fortuna, and P. Roca i Cabarrocas, Appl. Phys. Lett., 95, 113106 (2009)
[38] L. Yu, P.-J. Alet, G. Picardi, and P. Roca i Cabarrocas, Phys. Rev. Lett., 102, 125501 (2009)
[39] L. Yu, and P. R. i Cabarrocas, Phys. Rev. B, 81, 085323 (2010)
[40] J. L. Lensch-Falk, E. R. Hemesath, D. E. Perea, and L. J. Lauhon, J. Mater. Chem., 19, 849 (2009)
[41] C. Y. Wen, M. C. Reuter, J. Tersoff, E. A. Stach, and F. M. Ross, Nano Lett. (2009)
[42] J. Mallet, M. Molinari, F. Martineau, F. Delavoie, P. Fricoteaux, and M. Troyon, Nano Lett., 8, 3468 (2008)
[43] M. He, and S. N. Mohammad, The Journal of Chemical Physics, 124, 064714 (2006)
[44] S. N. Mohammad, The Journal of Chemical Physics, 125, 094705 (2006)
[45] N. Wang, Y. F. Zhang, Y. H. Tang, C. S. Lee, and S. T. Lee, Appl. Phys. Lett., 73, 3902 (1998)
[46] R. Q. Zhang, T. S. Chu, H. F. Cheung, N. Wang, and S. T. Lee, Materials Science and Engineering: C, 16, 31 (2001)
[47] R. Q. Zhang, Y. Lifshitz, and S. T. Lee, Adv. Mater., 15, 635 (2003)
[48] Y. Yao, F. Li, and S.-T. Lee, Chem. Phys. Lett., 406, 381 (2005)
[49] T. I. Kamins, R. S. Williams, D. P. Basile, T. Hesjedal, and J. S. Harris, J. Appl. Phys., 89, 1008 (2001)
[50] F. Iacopi, P. M. Vereecken, M. Schaekers, M. Caymax, N. Moelans, B. Blanpain, O. Richard, C. Detavernier, and H. Griffiths, Nanotechnology, 18, 505307 (2007)
[51] L. Schubert, P. Werner, N. D. Zakharov, G. Gerth, F. M. Kolb, L. Long, U. Gosele, and T. Y. Tan, Appl. Phys. Lett., 84, 4968 (2004)
[52] A. Irrera, E. F. Pecora, and F. Priolo, Nanotechnology, 20, 135601 (2009)
[53] A. I. Persson, M. W. Larsson, S. Stenstrom, B. J. Ohlsson, L. Samuelson, and L. R. Wallenberg, Nat. Mater., 3, 677 (2004)
[54] J. Westwater, D. P. Gosain, S. Tomiya, S. Usui, and H. Ruda, Journal of Vacuum Science & Technology B, 15, 554 (1997)
[55] S. Akhtar, A. Tanaka, K. Usami, Y. Tsuchiya, and S. Oda, Thin Solid Films, 517, 317 (2008)
[56] O. Moutanabbir, S. Senz, Z. Zhang, and U. Gösele, Nano Today, 4, 393 (2009)
[57] E. C. Garnett, and P. Yang, J. Am. Chem. Soc., 130, 9224 (2008)
[58] J. Huo, and et al., Nanotechnology, 15, 1848 (2004)
[59] Y. Wu, R. Fan, and P. Yang, Nano Lett., 2, 83 (2002)
[60] B. Fuhrmann, H. S. Leipner, H.-R. Hoche, L. Schubert, P. Werner, and U. Gosele, Nano Lett., 5, 2524 (2005)
[61] R. S. Wagner, W. C. Ellis, K. A. Jackson, and S. M. Arnold, J. Appl. Phys., 35, 2993 (1964)
[62] G. A. Bootsma, and H. J. Gassen, J. Cryst. Growth, 10, 223 (1971)
[63] Y. Wang, V. Schmidt, S. Senz, and U. Gosele, Nat. Nanotechnol., 1, 186 (2006)
[64] M. Jeon, and K. Kamisako, J. Alloys Compd., 476, 84 (2009)

[65] Y. Ke, X. Weng, J. M. Redwing, C. M. Eichfeld, T. R. Swisher, S. E. Mohney, and Y. M. Habib, Nano Lett., 9, 4494 (2009)
[66] V. T. Renard, M. Jublot, P. Gergaud, P. Cherns, D. Rouchon, A. Chabli, and V. Jousseaume, Nat. Nanotechnol., 4, 654 (2009)
[67] S. W. Boettcher, J. M. Spurgeon, M. C. Putnam, E. L. Warren, D. B. Turner-Evans, M. D. Kelzenberg, J. R. Maiolo, H. A. Atwater, and N. S. Lewis, Science, 327, 185 (2010)
[68] T. I. Kamins, R. Stanley Williams, T. Hesjedal, and J. S. Harris, Physica E, 13, 995 (2002)
[69] Q. Tang, X. Liu, T. I. Kamins, G. S. Solomon, and J. S. Harris, J. Cryst. Growth, 251, 662 (2003)
[70] E. C. Garnett, and P. Y. W. Liang, Adv. Mater., 19, 2946 (2007)
[71] B.-S. Kim, T.-W. Koo, J.-H. Lee, D. S. Kim, Y. C. Jung, S. W. Hwang, B. L. Choi, E. K. Lee, J. M. Kim, and D. Whang, Nano Lett., 9, 864 (2009)
[72] S. Roorda, S. Doorn, W. C. Sinke, P. M. L. O. Scholte, and E. van Loenen, Phys. Rev. Lett., 62, 1880 (1989)
[73] I. Stich, R. Car, and M. Parrinello, Phys. Rev. B, 44, 11092 (1991)
[74] L. Wei, X. Ping, and C. M. Lieber, Electron Devices, IEEE Transactions, 55, 2859 (2008)
[75] K. E. Moselund, H. Ghoneim, H. Schmid, M. T. Björk, E. Lörtscher, S. Karg, G. Signorello, D. Webb, M. Tschudy, R. Beyeler, and H. Riel, Nanotechnology, 21, 435202 (2010)
[76] D. R. Kim, C. H. Lee, and X. Zheng, Nano Lett., 9, 1984 (2009)
[77] G. Zheng, X. P. A. Gao, and C. M. Lieber, Nano Lett., 10, 3179 (2010)
[78] K. Takei, T. Takahashi, J. C. Ho, H. Ko, A. G. Gillies, P. W. Leu, R. S. Fearing, and A. Javey, Nat. Mater., 9, 821 (2010)
[79] L.-F. Cui, Y. Yang, C.-M. Hsu, and Y. Cui, Nano Lett., 9, 3370 (2009)
[80] Y. Yang, M. T. McDowell, A. Jackson, J. J. Cha, S. S. Hong, and Y. Cui, Nano Lett., 10, 1486 (2010)
[81] L. Hu, H. Wu, S. S. Hong, L. Cui, J. R. McDonough, S. Bohy, and Y. Cui, Chem. Commun., 47, 367 (2011)
[82] V. Sivakov, G. Andra, A. Gawlik, A. Berger, J. Plentz, F. Falk, and S. H. Christiansen, Nano Lett., 9, 1549 (2009)
[83] L. Liao, Y.-C. Lin, M. Bao, R. Cheng, J. Bai, Y. Liu, Y. Qu, K. L. Wang, Y. Huang, and X. Duan, Nature, 467, 305 (2010)
[84] T. Cohen-Karni, Q. Qing, Q. Li, Y. Fang, and C. M. Lieber, Nano Lett., 10, 1098 (2010)
[85] G. Agnus, A. Filoramo, S. Lenfant, D. Vuillaume, J. P. Bourgoin, and V. Derycke, Small, 6, 2659 (2010)
[86] Q. Shu, J. Wei, K. Wang, H. Zhu, Z. Li, Y. Jia, X. Gui, N. Guo, X. Li, C. Ma, and D. Wu, Nano Lett., 9, 4338 (2009)
[87] Hernandez-Martinez, P. L., Govorov, and A. O., Phys. Rev. B, 78, 035314 (2008)
[88] S. Lu, Z. Lingley, T. Asano, D. Harris, T. Barwicz, S. Guha, and A. Madhukar, Nano Lett., 9, 4548 (2009)
[89] K.-Q. Peng, X. Wang, X.-L. Wu, and S.-T. Lee, Nano Lett., 9, 3704 (2009)
[90] N. J. Quitoriano, and T. I. Kamins, Nano Lett., 8, 4410 (2008)
[91] M. D. Kelzenberg, S. W. Boettcher, J. A. Petykiewicz, D. B. Turner-Evans, M. C. Putnam, E. L. Warren, J. M. Spurgeon, R. M. Briggs, N. S. Lewis, and H. A. Atwater, Nat. Mater., 9, 239 (2010)
[92] K. Peng, Y. Xu, Y. Wu, Y. Yan, S.-T. Lee, and J. Zhu, Small, 1, 1062 (2005)
[93] Y. K. Cheng, G. Chie, and T. D. Bau, Sol. Energy Mater. Sol. Cells, 95, 154 (2011)

[94] T. J. Kempa, B. Tian, D. R. Kim, J. Hu, X. Zheng, and C. M. Lieber, Nano Lett., 8, 3456 (2008)
[95] S. Hoffmann, J. Bauer, C. Ronning, T. Stelzner, J. Michler, C. Ballif, V. Sivakov, and S. H. Christiansen, Nano Lett., 9, 1341 (2009)
[96] B. Tian, X. Zheng, T. J. Kempa, Y. Fang, N. Yu, G. Yu, J. Huang, and C. M. Lieber, Nature, 449, 885 (2007)
[97] C. Yang, Z. Zhong, and C. M. Lieber, Science, 310, 1304 (2005)
[98] B. M. Kayes, H. A. Atwater, and N. S. Lewis, J. Appl. Phys., 97, 114302 (2005)
[99] R. F. Pierret, Semiconductor Fundamentals, Prentice Hall, 99 (1988)
[100] L. Cao, J. S. White, J.-S. Park, J. A. Schuller, B. M. Clemens, and M. L. Brongersma, Nat. Mater., 8, 643 (2009)
[101] L. Cao, P. Fan, and M. L. Brongersma, Nano Lett., 11, 1463 (2011)
[102] V. Schmidt, H. Riel, S. Senz, S. Karg, W. Riess, and U. Gösele, Small, 2, 85 (2006)
[103] L. Yu, W. H. Chen, G. Patriarche, S. Bouchoule, P. Pareige, R. Rogel, A. C. Salaun, L. Pichon, and P. Roca i Cabarrocas, Applied Physics Letters 99 (20), 203104 (2011).
[104] D. Whang, S. Jin, Y. Wu, and C. M. Lieber, Nano Lett., 3, 1255 (2003)
[105] S. Jin, D. Whang, M. C. McAlpine, R. S. Friedman, Y. Wu, and C. M. Lieber, Nano Lett., 4, 915 (2004)
[106] D. L. Fan, F. Q. Zhu, R. C. Cammarata, and C. L. Chien, Appl. Phys. Lett., 85, 4175 (2004)
[107] R. Agarwal, K. Ladavac, Y. Roichman, G. Yu, C. Lieber, and D. Grier, Opt. Express, 13, 8906 (2005)
[108] P. J. Pauzauskie, A. Radenovic, E. Trepagnier, H. Shroff, P. Yang, and J. Liphardt, Nat. Mater., 5, 97 (2006)
[109] G. Yu, A. Cao, and C. M. Lieber, Nat. Nanotechnol., 2, 372 (2007)
[110] Z. Fan, J. C. Ho, Z. A. Jacobson, R. Yerushalmi, R. L. Alley, H. Razavi, and A. Javey, Nano Lett., 8, 20 (2007)
[111] A. Pevzner, Y. Engel, R. Elnathan, T. Ducobni, M. Ben-Ishai, K. Reddy, N. Shpaisman, A. Tsukernik, M. Oksman, and F. Patolsky, Nano Lett., 10, 1202 (2010)
[112] E. M. Freer, O. Grachev, and D. P. Stumbo, Nat. Nanotechnol., 5, 525 (2010)
[113] J. M. Weisse, D. R. Kim, C. H. Lee, and X. Zheng, Nano Lett., 11, 1300 (2011)
[114] B. J. Kim, J. Tersoff, S. Kodambaka, M. C. Reuter, E. A. Stach, and F. M. Ross, Science, 322, 1070 (2008)
[115] F. M. Ross, Rep. Prog. Phys., 73, 114501 (2010)
[116] C. X. Wang, M. Hirano, and H. Hosono, Nano Lett., 6, 1552 (2006)
[117] V. A. Sivakov, G. Bronstrup, B. Pecz, A. Berger, G. Z. Radnoczi, M. Krause, and S. H. Christiansen, J. Phys. Chem. C, 114, 3798 (2010)
[118] N. Li, T. Y. Tan, and U. Gösele, Appl. Phys. A, 86, 433 (2007)
[119] K. W. Schwarz, and J. Tersoff, Phys. Rev. Lett., 102, 206101 (2009)
[120] C. Wiethoff, F. M. Ross, M. Copel, M. Horn-von Hoegen, and F.-J. Meyer zu Heringdorf, Nano Lett., 8, 3065 (2008)
[121] F. Oehler, P. Gentile, T. Baron, P. Ferret, M. Den Hertog, and J. Rouviere, Nano Lett., 10, 2335 (2010)
[122] Y. Kim, H. J. Joyce, Q. Gao, H. H. Tan, C. Jagadish, M. Paladugu, J. Zou, and A. A. Suvorova, Nano Lett., 6, 599 (2006)
[123] M. T. Borgstrom, G. Immink, B. Ketelaars, R. Algra, and P. A. M. BakkersErik, Nat. Nanotechnol., 2, 541 (2007)
[124] P. Madras, E. Dailey, and J. Drucker, Nano Lett., 9, 3826 (2009)
[125] J. Kikkawa, Y. Ohno, and S. Takeda, Appl. Phys. Lett., 86, 123109 (2005)
[126] D. Kashchiev, Cryst. Growth Des., 6, 1154 (2006)

[127] I. Avramov, Nanoscale Res. Lett., 2, 235 (2007)
[128] S. N. Mohammad, J. Appl. Phys., 106, 104311 (2009)
[129] Y. Cui, L. J. Lauhon, M. S. Gudiksen, J. Wang, and C. M. Lieber, Appl. Phys. Lett., 78, 2214 (2001)
[130] T. Xu, J. P. Nys, A. Addad, O. I. Lebedev, A. Urbieta, B. Salhi, M. Berthe, B. Grandidier, and D. Sti évenard, Phys. Rev. B, 81, 115403 (2010)
[131] Y. Wu, Y. Cui, L. Huynh, C. J. Barrelet, D. C. Bell, and C. M. Lieber, Nano Lett., 4, 433 (2004)
[132] H. Baker, and H. Okamoto, ASM Handbook: Volume 3: Alloy Phase Diagrams, ASM International, 2·76 (1992)
[133] E. J. Schwalbach, and P. W. Voorhees, Nano Lett., 8, 3739 (2008)
[134] E. Sutter, and P. Sutter, Nano Lett., 8, 411 (2008)
[135] B. J. Kim, J. Tersoff, C. Y. Wen, M. C. Reuter, E. A. Stach, and F. M. Ross, Phys. Rev. Lett., 103, 155701 (2009)
[136] D. T. J. Hurle, handbookof crystal growth Volume 2: bulk crystal growth, ELSEVIER (1993)
[137] V. G. Dubrovskii, and N. V. Sibirev, Phys. Rev. E, 70, 031604 (2004)
[138] C.-Y. Wen, M. C. Reuter, J. Bruley, J. Tersoff, S. Kodambaka, E. A. Stach, and F. M. Ross, Science, 326, 1247 (2009)
[139] F. Glas, J.-C. Harmand, and G. Patriarche, Phys. Rev. Lett., 99, 146101 (2007)
[140] B. A. Wacaser, K. A. Dick, J. Johansson, M. T. Borgstr öm, K. Deppert, and L. Samuelson, Adv. Mater., 21, 153 (2009)
[141] S. Hofmann, R. Sharma, C. T. Wirth, F. Cervantes-Sodi, C. Ducati, T. Kasama, R. E. Dunin-Borkowski, J. Drucker, P. Bennett, and J. Robertson, Nat. Mater., 7, 372 (2008)
[142] L. Yu, and P. Roca i Cabarrocas, Phys. Rev. B, 80, 085313 (2009)
[143] W. Ostwald, Engelmann: Leipzig, Germany, Vol. 2 (1896)
[144] I. M. Lifshitz, and V. V. Slyozov, J. Phys. Chem. Solids, 19, 35 (1961)
[145] U. Gosele, Nature, 440, 34 (2006)
[146] L. Cao, B. Garipcan, J. S. Atchison, C. Ni, B. Nabet, and J. E. Spanier, Nano Lett., 6, 1852 (2006)
[147] A. Bailly, O. Renault, N. Barrett, L. F. Zagonel, P. Gentile, N. Pauc, F. Dhalluin, T. Baron, A. Chabli, J. C. Cezar, and N. B. Brookes, Nano Lett., 8, 3709 (2008)
[148] E. Dailey, P. Madras, and J. Drucker, J. Appl. Phys., 108, 064320 (2010)
[149] V. A. Sivakov, and et al., Nanotechnology, 20, 405607 (2009)
[150] M. I. den Hertog, J.-L. Rouviere, F. Dhalluin, P. J. Desr é, P. Gentile, P. Ferret, F. Oehler, and T. Baron, Nano Lett., 8, 1544 (2008)
[151] T. Kawashima, T. Mizutani, T. Nakagawa, H. Torii, T. Saitoh, K. Komori, and M. Fujii, Nano Lett., 8, 362 (2008)
[152] W. H. Chen, R. Larde, E. Cadel, T. Xu, B. Grandidier, J. P. Nys, D. Stievenard, and P. Pareige, J. Appl. Phys., 107, 084902 (2010)
[153] S. Kodambaka, J. B. Hannon, R. M. Tromp, and F. M. Ross, Nano Lett., 6, 1292 (2006)
[154] A. Lugstein, M. Steinmair, Y. J. Hyun, G. Hauer, P. Pongratz, and E. Bertagnolli, Nano Lett., 8, 2310 (2008)
[155] V. Schmidt, S. Senz, and U. Gosele, Nano Lett., 5, 931 (2005)
[156] B. Tian, P. Xie, T. J. Kempa, D. C. Bell, and C. M. Lieber, Nat. Nanotechnol., 4, 824 (2009)
[157] R. Q. Zhang, Y. Lifshitz, D. D. D. Ma, Y. L. Zhao, T. Frauenheim, S. T. Lee, and S. Y. Tong, The Journal of Chemical Physics, 123, 144703 (2005)
[158] R. S. Wagner, J. Appl. Phys., 38, 1554 (1967)

[159] J. Jie, W. Zhang, K. Peng, G. Yuan, C. S. Lee, and S.-T. Lee, Adv. Funct. Mater., 18, 3251 (2008)
[160] X. Xu, and P. Servati, Nano Lett., 9, 1999 (2009)
[161] A. J. Tavendale, and S. J. Pearton, J. Phys. C: Solid State Phys., 16, 1665 (1983)
[162] M. Lv, S. Su, Y. He, Q. Huang, W. Hu, D. Li, C. Fan, and S.-T. Lee, Adv. Mater., 22, 5463 (2010)
[163] T. J. Morrow, M. Li, J. Kim, T. S. Mayer, and C. D. Keating, Science, 323, 352 (2009)
[164] K. Jiang, D. Fan, Y. Belabassi, G. Akkaraju, J.-L. Montchamp, and J. L. Coffer, ACS Appl. Mat. Interfaces, 1, 266 (2008)
[165] F. M. Ross, J. Tersoff, and M. C. Reuter, Phys. Rev. Lett., 95, 146104 (2005)
[166] L. Seehofer, S. Huhs, G. Falkenberg, and R. L. Johnson, Surf. Sci., 329, 157 (1995)
[167] H. Minoda, K. Yagi, F. J. Meyer zu Heringdorf, A. Meier, auml, D. hler, and M. Horn von Hoegen, Phys. Rev. B, 59, 2363 (1999)
[168] E. I. Givargizov, J. Cryst. Growth, 31, 20 (1975)
[169] Z. Chen, and C. Cao, Appl. Phys. Lett., 88, 143118 (2006)
[170] F. Dhalluin, T. Baron, P. Ferret, B. Salem, P. Gentile, and J. C. Harmand, Appl. Phys. Lett., 96, 133109 (2010)
[171] H. Zhao, S. Zhou, Z. Hasanali, and D. Wang, J. Phys. Chem. C, 112, 5695 (2008)
[172] J. Johansson, C. P. T. Svensson, T. Martensson, L. Samuelson, and W. Seifert, J. Phys. Chem. B, 109, 13567 (2005)
[173] V. G. Dubrovskii, N. V. Sibirev, G. E. Cirlin, I. P. Soshnikov, W. H. Chen, R. Larde, E. Cadel, P. Pareige, T. Xu, B. Grandidier, J. P. Nys, D. Stievenard, M. Moewe, L. C. Chuang, and C. Chang-Hasnain, Phys. Rev. B, 79, 205316 (2009)
[174] V. Schmidt, S. Senz, and U. Gosele, Phys. Rev. B, 75, 045335 (2007)
[175] Y. Cui, X. Duan, J. Hu, and C. M. Lieber, J. Phys. Chem. B, 104, 5213 (2000)
[176] A. Colli, A. Fasoli, C. Ronning, S. Pisana, S. Piscanec, and A. C. Ferrari, Nano Lett., 8, 2188 (2008)
[177] L. Pan, K.-K. Lew, J. M. Redwing, and E. C. Dickey, J. Cryst. Growth, 277, 428 (2005)
[178] C.-Y. Meng, B.-L. Shih, and S.-C. Lee, J. Nanopart. Res., 7, 615 (2005)
[179] K.-K. Lew, L. Pan, T. E. Bogart, S. M. Dilts, E. C. Dickey, J. M. Redwing, Y. Wang, M. Cabassi, T. S. Mayer, and S. W. Novak, Appl. Phys. Lett., 85, 3101 (2004)
[180] L. Tsakalakos, J. Balch, J. Fronheiser, B. A. Korevaar, O. Sulima, and J. Rand, Appl. Phys. Lett., 91, 233117 (2007)
[181] Y. Wang, K.-K. Lew, T.-T. Ho, L. Pan, S. W. Novak, E. C. Dickey, J. M. Redwing, and T. S. Mayer, Nano Lett., 5, 2139 (2005)
[182] H. Schmid, M. T. Bjork, J. Knoch, S. Karg, H. Riel, and W. Riess, Nano Lett., 9, 173 (2009)
[183] Q. Tang, T. I. Kamins, X. Liu, D. E. Grupp, and J. S. Harris, Electrochem. Solid-State Lett., 8, G204 (2005)
[184] E. Koren, Y. Rosenwaks, J. E. Allen, E. R. Hemesath, and L. J. Lauhon, Appl. Phys. Lett., 95, 092105 (2009)
[185] E. Koren, N. Berkovitch, and Y. Rosenwaks, Nano Lett., 10, 1163 (2010)
[186] S. Hofmann, C. Ducati, R. J. Neill, S. Piscanec, A. C. Ferrari, J. Geng, R. E. Dunin-Borkowski, and J. Robertson, J. Appl. Phys., 94, 6005 (2003)
[187] G. Imamura, T. Kawashima, M. Fujii, C. Nishimura, T. Saitoh, and S. Hayashi, Nano Lett., 8, 2620 (2008)
[188] O. Gunawan, L. Sekaric, A. Majumdar, M. Rooks, J. Appenzeller, J. W. Sleight, S. Guha, and W. Haensch, Nano Lett., 8, 1566 (2008)

[189] P. Xie, Y. Hu, Y. Fang, J. Huang, and C. M. Lieber, Proceedings of the National Academy of Sciences, 106, 15254 (2009)
[190] E. C. Garnett, Y.-C. Tseng, D. R. Khanal, J. Wu, J. Bokor, and P. Yang, Nat. Nanotechnol., 4, 311 (2009)
[191] M. I. den Hertog, H. Schmid, D. Cooper, J.-L. Rouviere, M. T. Bjork, H. Riel, P. Rivallin, S. Karg, and W. Riess, Nano Lett., 9, 3837 (2009)
[192] J. E. Allen, E. R. Hemesath, D. E. Perea, J. L. Lensch-Falk, LiZ.Y, F. Yin, M. H. Gass, P. Wang, A. L. Bleloch, R. E. Palmer, and L. J. Lauhon, Nat. Nanotechnol., 3, 168 (2008)
[193] T. Xu, J. P. Nys, B. Grandidier, D. Sti évenard, Y. Coffinier, R. Boukherroub, R. Larde, E. Cadel, and P. Pareige, Journal of Vacuum Science & Technology B, 26, 1960 (2008)
[194] D. E. Perea, E. R. Hemesath, E. J. Schwalbach, J. L. Lensch-Falk, P. W. Voorhees, and L. J. Lauhon, Nat. Nanotechnol., 4, 315 (2009)
[195] W. H. Chen, R. Larde, E. Cadel, T. Xu, B. Grandidier, J. P. Nys, D. Stievenard, and P. Pareige, Physica Status Solidi (c), 8, 771 (2011)
[196] D. H. K. Murthy, T. Xu, W. H. Chen, A. J. Houtepen, T. J. Savenije, L. D. A. Siebbeles, J. P. Nys, C. Krzeminski, B. Grandidier, D. Stievenard, P. Pareige, F. Jomard, G. Patriarche, and O. I. Lebedev, Nanotechnology, 22, 315710 (2011)
[197] J. E. Allen, D. E. Perea, E. R. Hemesath, and L. J. Lauhon, Adv. Mater., 21, 3067 (2009)
[198] T. Umesaka, H. Ohnaka, Y. Ohno, S. Kishimoto, K. Maezawa, and T. Mizutani, Jpn. J. Appl. Phys., 46, 2496 (2007)

Chapter II

II Experimental techniques

In this chapter, the experimental techniques used in this work are presented. It is divided into two sections dealing with the elaboration techniques and the characterization techniques, respectively. The first section presents the basic principles of the etching processes, the Vapor-Solid-Liquid (VLS) mechanism-based techniques (Chemical Vapor Deposition (CVD) and Molecular Beam Epitaxy (MBE)) and the Solid-Liquid-Solid (SLS) mechanism-based technique. The second section presents the basic principles of Scanning Electron Microscopy (SEM), Focused Ion Beam (FIB) based milling, Transmission Electron Microscopy (TEM) and Atom Probe Tomography (APT). Several specimen preparation methods of NWs for APT characterization developed in this work are given in detail.

II.1 Elaboration techniques

In the domain of Si NW elaboration, different growth methods can be used. Indeed, the top-down approach consists in using etching processes such as the Deep Reactive Ion Etching (DRIE) and the bottom-up approach consists in using either chemical or physical vapor deposition methods. In this section, different fabrication processes used in both approaches are described.

II.1.1 Si nanowires obtained by etching

Deep Reactive Ion Etching (DRIE) is a highly anisotropic etching process using chemically reactive plasma (high energy ions) to remove materials [1]. It is often applied for fabricating nanostructures with high aspect ratio of 20:1 or even more. There are two methods of DRIE, namely, cryogenic and Bosch [2]. In the cryogenic method, the low temperature of the specimen (-110 ℃) can slow down the chemical reaction but ions continue to etch the surface of a sample. The Bosch method is based on the alternation of a passivation step by C_4F_8 and an etching step thanks to a mixture of SF_6/O_2. The passivation layer of C_4F_8 protects the entire substrate from further chemical attack and can also prevent further etching. The Bosch method can provide a nanostructure with a depth of 150 μm. In this work, the Bosh method was used for the Si NW fabrication. Figure II.1 (a) is the photography of system used

at IEMN (Lille). Figure II.1 (b) is the schematic illustration of the deep reactive ion etching chamber.

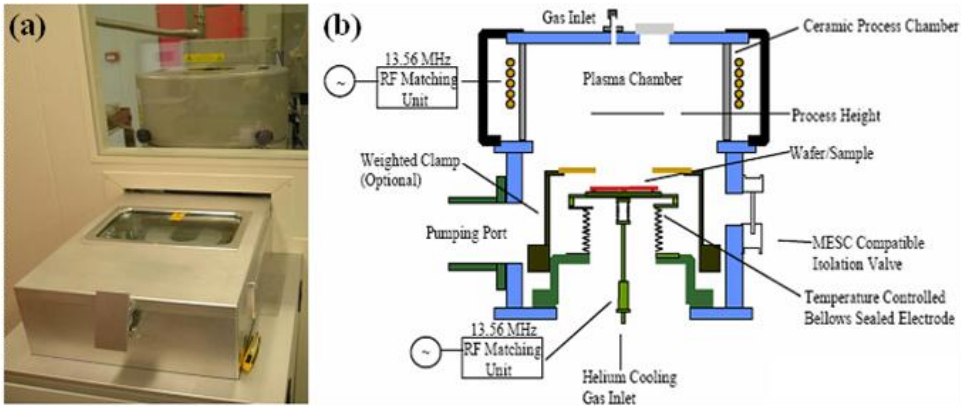

Figure II.1 – (a) Photography of surface technology system at IEMN (Lille). (b) Schematic illustration of deep reactive ion etching chamber.

II.1.2 Si nanowires grown by Vapor-Liquid-Solid (VLS) mechanism-based methods

As discussed in chapter I.2, several Vapor-Liquid-Solid (VLS) mechanism-based methods can be applied for growing Si NWs. In this work, two main growth methods, namely, CVD and MBE were used.

II.1.2.1 Chemical Vapor Deposition (CVD)

In the CVD process, a chemical reaction transforms a molecular gas (precursor such as SiH_4) into a high purity and high performance solid materials in the form of thin film, powder or NWs (e.g. Si NWs) that grow on a substrate. For example, in the case of the Si NW growth, the involved chemical reaction is the following: $SiH_4 = Si + 2H_2$ [3]. There are two main types of CVD: low pressure CVD and plasma enhanced CVD.

The low pressure CVD operates at the sub atmospheric pressure. The low pressure can keep the unwanted gas reaction and the uniformity of specimen deposited. This reaction depends on the thermal energy. Therefore, a high temperature is needed for the low pressure CVD to accelerate the chemical reaction.

The plasma enhanced CVD operates also at low pressure. This reaction depends not only on the thermal energy but also on the plasma energy and can thus be operated at lower temperature.

In this work, a high temperature and low pressure CVD reactor was used for growing Si NWs. The photography of this reactor is shown in Figure II.2 (a). As illustrated in Figure

II.2 (b), the CVD reactor is composed of three parts: the gas distribution for providing NW growth precursors (e.g. SiH_4, B_2H_6 and PH_3) and carrier gas (e.g. H_2 and Ar); the furnace with a quartz tube (T_{max} = 1150 ℃) and the pumping system with an Alcatel dry pump providing a pressure from 10^{-3} to 500 mbar. The pumping system is equipped with a Boc Edwards scrubber system for purification of the exhaust gas.

The CVD-grown Si NWs were synthesized in this reactor on a Si substrate using Au as catalyst. Silane, hydrogen, diborane and phosphine were used as the precursor, carrier gas and dopant reactants respectively. Different pressures were used to grow Si NWs.

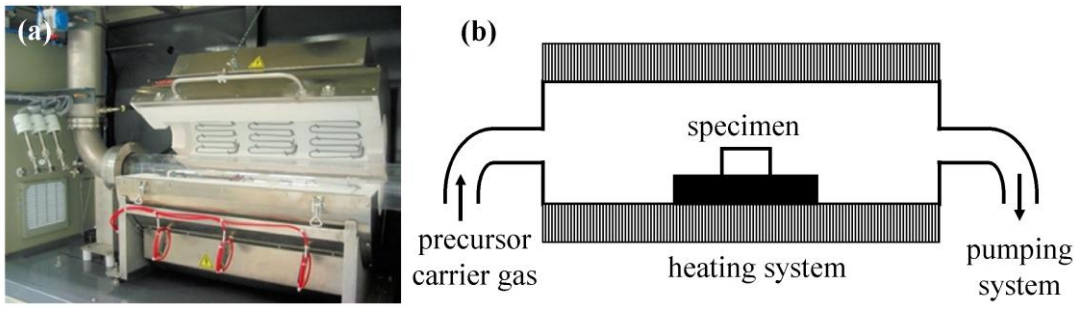

Figure II.2 – (a) High temperature and low pressure industry chemical vapor deposition reactor at IEMN (Lille). (b) Schematic illustration of a low pressure chemical vapor deposition reactor.

II.1.2.2 Molecular Beam Epitaxy (MBE)

MBE is a widely used deposition technique for the epitaxial growth of thin films. It consists in sublimating, in Ultra High Vacuum (UHV), ultra-pure elements heated in separate Knudsen effusion cells. The molecular vapor beams condenses into a substrate with a very low deposition rate [4]. In this work, a Komponenten GmbH effusion cell integrated UHV was used. The base pressure in the UHV growth chamber can be maintained below 10^{-10} mbar. The UHV system contains additional surface analysis tools, such as a Low Energy Electron Diffraction (LEED) for the electron diffraction characterization, a Scanning Tunneling Microscope (STM) to image surfaces in real space and an electron analyzer for Auger spectroscopy, as shown in Figure II.3 (a). The schematic of the MBE growth stage is illustrated in Figure II.3 (b). One element such as Si or Ge can be evaporated in the effusion cell.

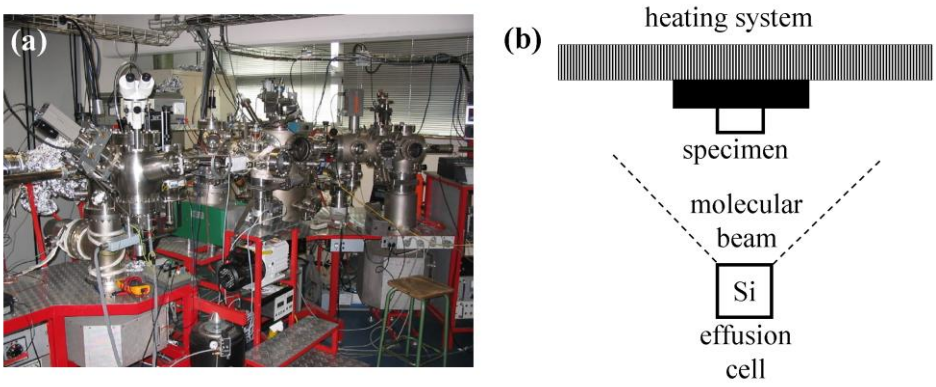

Figure II.3 – (a) Ultra high vacuum system for molecular beam epitaxy at IEMN (Lille). (b) Schematic illustration of molecular beam epitaxy.

II.1.3 Si nanowires grown by Solid-Liquid-Solid (SLS) mechanism-based method

For growing the in-plane Si NWs by SLS, the plasma enhanced CVD reactor at LPICM (Palaiseau) was used. Figure II.4 (a) is the photograph of the plasma enhanced CVD chamber and its schematic illustration is presented in Figure II.4 (b). All the steps that lead to the formation of Si NWs, starting with the formation of catalyst droplets to the NW growth can be done in this chamber. The plasma (H_2) can be used for the deposition of the catalyst droplets on the substrate. After the deposition of an amorphous Si:H layer, the Si NWs can be grown by heating the substrate at certain temperature. For the realization of *in-situ* deposition and growth, the plasma enhanced CVD is equipped with an *in-situ* spectroscopic ellipsometer module as shown in Figure II.4 (a).

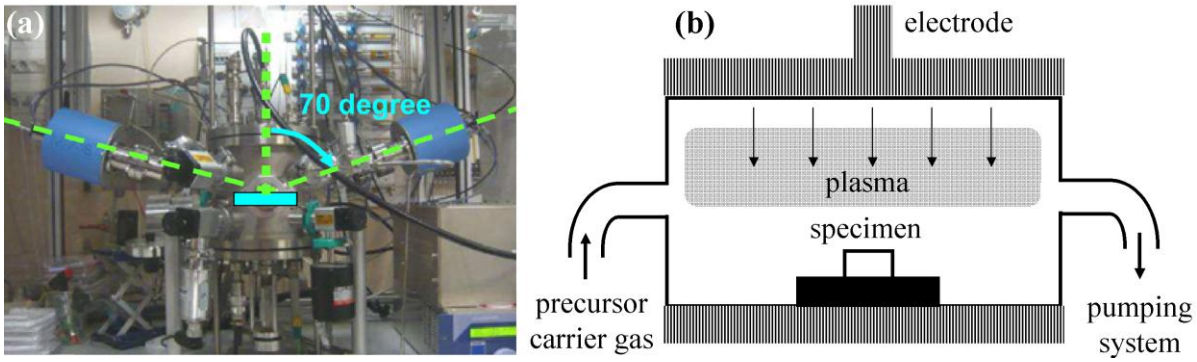

Figure II.4 – (a) Plasma enhanced chemical vapor deposition reactor equipped with an in-situ spectroscopic ellipsometer at LPICM (Palaiseau). (b) Schematic illustration of plasma enhanced chemical vapor deposition reactor.

II.2 Characterization techniques

II.2.1 Scanning Electron Microscope and Focus Ion Beam

II.2.1.1 Scanning Electron Microscope (SEM)

Scanning Electron Microscope (SEM) is a typical electron microscope which is widely used in material sciences [5, 6]. The first SEM image was observed by Knoll Max in 1935 [7]. SEM can image the specimen surface with a relative high accelerating voltage ranging from < 1 keV to 30 keV. SEM is composed of several parts: the electron gun, the lenses, the apertures, the controls of specimen position and the area of beam/specimen interaction. All of these parts above are maintained at high vacuum. Considering the incident electron source, three types of electron guns are used: Tungsten hairpin, Lanthanum hexaboride (LaB_6) and Field Emission Gun (FEG). Imaging with SEM is realized thanks to the interactions of incident electrons with the specimen atoms [8]. From these interactions, different kinds of signals are generated from specimen such as Secondary Electrons (SE) with energies < 50 eV, Back Scattered Electrons (BSE), X-Rays and so on as illustrated in Figure II.5. Based on the detection of these different signals, SEM can work with several modes. The SE imaging is the most common operation mode. The resolution of 0.5 nm can be achieved with recent generation of FEG-SEM [9].

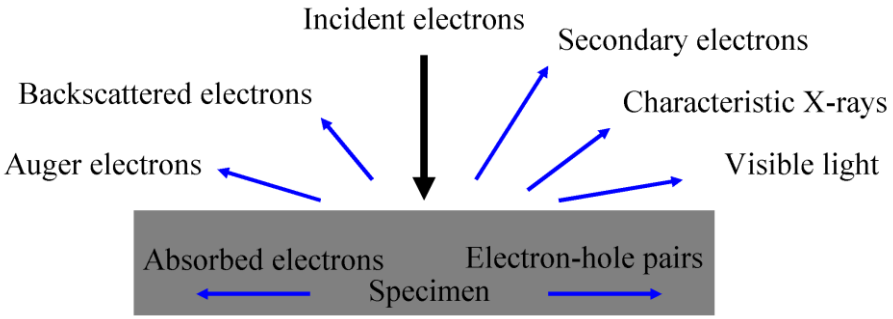

Figure II.5 – Schematic illustration of signals generated when the incident electrons interact with the specimen atoms. The arrows indicate the relative direction and intensity of signals.

II.2.1.2 Focused Ion Beam (FIB)

Focused Ion Beam (FIB) was developed for specific site analysis, deposition and sputtering of materials [10, 11]. A basic FIB instrument consists of a liquid ion source, an ion column, a specimen stage, detectors, a gas delivery system and a control system, which is very similar to SEM. Ga metal ion sources is the most commonly used liquid ion source for commercial FIB. FIB is based on the interaction of incident ions with atoms constituting the

specimen [12]. The most accepted model of ion and material interaction of FIB is the collision cascade [13]. Several types of signals and particles will be generated when the Ga ion beam hits the specimen surface as illustrated in Figure II.6. The signal of secondary electrons and secondary ions can be collected for imaging. But the resolution of FIB imaging is lower than SEM because of the ion beam (10 nm [14]) can not be focused finely enough as an electron beam (5 nm [15]). Considering the sputtering process, the quantity of specimen sputtered by ion beam is related to ion beam current. For sputtering the materials, FIB works in a high ion beam current and a high acceleration voltage (30 keV), this is so called the milling process of sample preparation. Whereas, at low ion beam current and low acceleration voltage (2 keV), only a small of amount of material can be sputtered, this is so called the cleaning process of sample preparation. The limited feature size of direct milling of FIB is about 10 nm [16]. Its is worth mentioning here that the Ga ions can be implanted into the specimen inducing damages (e.g. point defects or loops) during imaging and milling [17]. For this reason, a protective layer is deposited (e.g. Pt and W) before FIB imaging and milling.

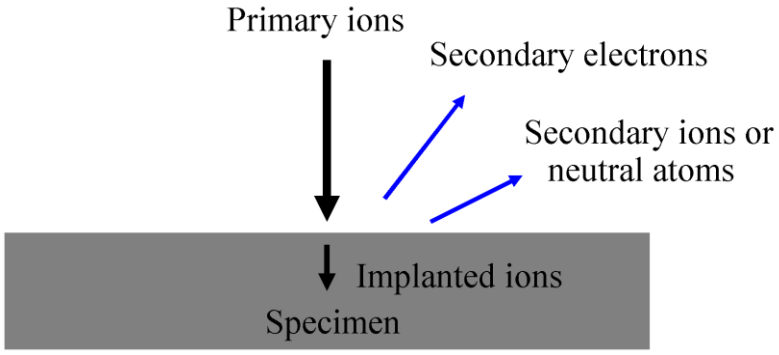

Figure II.6 – Schematic diagram of imaging and sputtering process of FIB. The arrows indicate the relative direction and intensity of signals.

In this work, two kinds of dual-beam SEM-FIB work station are used: LEO FE 1530 and NVISION 40 ZEISS SMT. These instrument platforms combine a SEM-FEG column and a FIB column (Figure II.7) [18, 19].

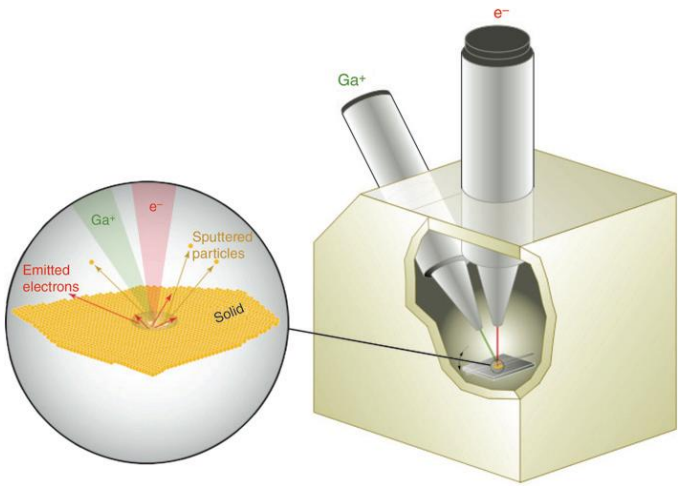

Figure II.7 – Schematic illustration of a typical dual-beam FIB–SEM system. Expanded image shows the electron and ion beam specimen interaction. Adapted from [19].

FIB and SEM can be used to deposit material at specific regions combining the Gas Injection System (GIS) for local CVD and specimen preparation [20, 21]. GIS can work in two different modes: Ion beam-induced deposition (IBID) [22] and Electron beam-induced deposition (EBID) [23, 24] respectively. IBID is a process of decomposing gaseous molecules such as (Me_3)MeCpPt with a chemical reaction by ion beam to induce a Pt deposition, for instance. Other materials such as C, W and SiO_2 can also be deposited. Thus, by choosing appropriate parameters such as ion beam current and the size of the deposition surface, metallic or insulating thin layers can be deposited by IBID. EBID is a similar deposition process as IBID by changing ion beam to electron beam. In both cases, it is the secondary electrons that induce the deposition [25]. The advantage of IBID is the high efficiency compared to EBID. However, there is always the risk of sputtering material during IBID. For a nano scale deposition such as deposition on a Si NW, EBID is a more appropriate deposition choice. In addition to SEM, FIB and GIS, the dual-beam platform is equipped with a micro manipulator for realizing a versatile manipulation to obtain specific views of the sample, remove matter, transfer samples and weld materials. In this work, the dual-beam SEM-FIB work station is equipped with a micro manipulator (Kleindiek, nanotechnik, Germany).

II.2.2 Transmission Electron Microscope (TEM)

Transmission Electron Microscope (TEM) is another kind of electron microscope [26]. The first TEM was built by Ruska in 1934 [27]. Compared to the electron beam of SEM, a super high energy of electron beam with a kinetic energy ranging from 100 keV to 400 keV is

used in TEM. When this high energy electron beam interacts with a very thin specimen, a variety of signals can be produced as illustrated in Figure II.8. The electrons can be scattered elastically or inelastically when they pass through the thin specimen. The electron scattering is the underlying physic of TEM. Considering TEM characterization, there are three different types: diffraction, imaging and spectroscopy. The electrons elastically scattered are used for diffraction. The images collected from transmitted (centre region) and diffracted (edge region) signals referred to bright field and dark field images respectively. The elastically scattered electron signal can contribute to the formation of high-resolution bright-field image. Electrons which are scattered to very large angles are utilized for Z-contrast (atomic number) annular dark field imaging. The inelastically scattered electrons can be used to characterize the specimen composition by Electron Energy Loss Spectroscopy (EELS). The detection of characteristic X-rays can be also used as the Energy Dispersive Spectroscopy (EDS) with a resolution up to 0.2 nm.

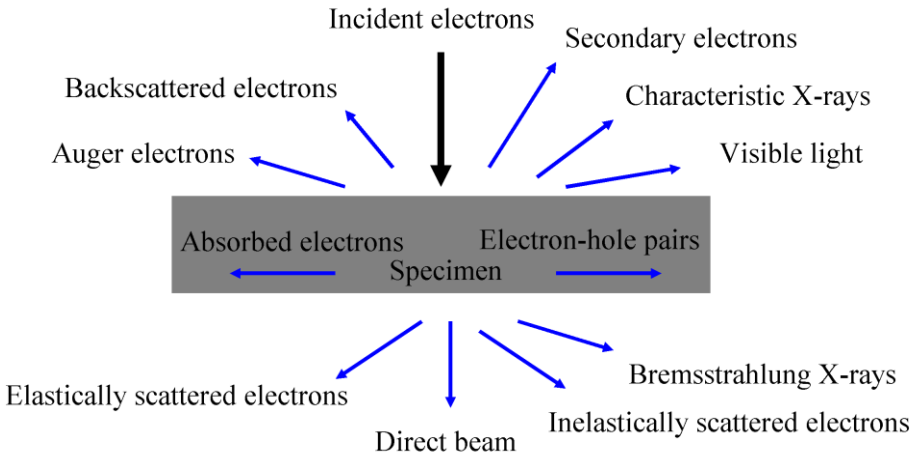

Figure II.8 – Schematic illustration of different types of signals generated when the high energy beam of incident electrons interacts with a very thin specimen. The arrows indicate the relative direction and intensity of signals.

Different operating modes can be distinguished. Among them, High-Resolution Transmission Electron Microscopy (HRTEM) and Scanning Transmission Electron Microscopy (STEM) are widely used.

- The High-Resolution Transmission Electron Microscopy (HRTEM) is a high-resolution mode of TEM for characterization of specimen crystallographic structure with atomic scale (~ 0.1 nm). HRTEM use the phase contrast imaging which is result from interference of several beams (diffracted and transmitted electron waves) compared to the detection of only one type of beams (diffracted or transmitted) in the conventional TEM.

Generally, the more beams are collected, the higher the resolution of HRTEM is. The HRTEM contrast arises from the difference of electron waves scattered from the specimen. The crystallographic structure, defects and accumulation of atoms can be clearly characterized and determined with the quantitative recording and suitable imaging process. The greatest challenge of HRTEM is to reach a correct interpretation of the image.

- The Scanning Transmission Electron Microscopy (STEM) is a special TEM mode where the electron beam is focused as a small spot (4~5 nm) and scans the specimen. It should be noted here that the scanning electron beam in STEM must not change direction when the beam is scanned, unlike in SEM where the scanning beam simply pivots about a point above the specimen. During the same single scan of the incident electron beam over the thin specimen, the bright-field and dark-field images and images with secondary radiations can be obtained. The bright-field STEM images can be obtained with the zero-loss electrons from the central beam of the pattern. The dark-field mages can be obtained by selecting electrons that have lost the few electron volts or with the many-electron-volt losses due to the inner-shell electron excitations characteristic of the various elements present in the specimen. The different contrast related to very large atomic number such as Au and In compared to Si can be clearly distinguished with an atomic resolution using the High Angle Annular Dark Field STEM (HAADF STEM).

Considering the specimen preparation for TEM, several methods can be proposed such as mechanical and electrochemical polishing [28] or FIB milling [29, 30]. The specimen prepared for TEM should be transparent for electron. A series of specimen preparation methods can be found in the literature [31]. In this work, the TEM characterization is realized by Dr. G. Patriarche at LPN, Marcoussis.

II.2.3 Atom Probe Tomography (APT)

Atom Probe Tomography (APT) is a three dimensional analytical high resolution microscope. Its principle is based on the evaporation by field effect of surface atoms from a sample with a very sharp tip. This technique found its origin in the invention of the field ion microscope (1951) and atom probe (1968) by E. Müller. The first atom probe is allowed to measure the chemical composition of a sample [32]. For such analysis, the sample has to be prepared in a very sharp tip shape with a radius of curvature less than 50 nm. It is then placed in UHV, cooled down under 80K and positively polarized with a high electric potential (V) of several kV. It results in the appearance of a high electric field (E) at the apex of the tip whose

intensity is inversely proportional to the radius of curvature R of the tip (tip effect) (Equation II.1).

$$E = \frac{V}{\beta R} \qquad \text{(Equation II.1)}$$

where β is a numerical factor due to the cone angle of the tip (β ~ 2-8), V is he voltage applied on the tip and R is its radius. The small value of R (≈ 50 nm) allows to reach a high electric field intensity of several tens V/nm, which causes the ionization and evaporation of surface atoms of the sample. The evaporated atoms are then accelerated and collected by an ion detector which is placed in the front of the tip. The chemical nature of each evaporated atom is then accessible with mass spectrometry where the ion mass-to-charge ratio is determined via a time measurement (Time of Flight (ToF) mass spectrometry). By evaporating the sample atomic layer by atomic layer, the chemical composition at different depth of the sample can be obtained. The tomographic aspect of atom probe was developed in the early 1990s. The ion detector initially constituting the mass spectrometer has been replaced by a position sensitive ion detector. This type of detector can not only measure ToF, but also record the impact position (X, Y) of each ion. This information allows to calculate the initial position of atoms on the surface of the sample by reverse projection and to reconstruct in three dimensions (3D) the analyzed volume of the sample. APT allows to observe the structure of matter at the atomic scale in 3D and in the real space [33, 34]. A detailed description of atom probe can be found in the literature [35, 36].

II.2.3.1 Time of flight mass spectrometry: chemical identity of atoms

Measuring ToF of an evaporated atom requires knowing the moment of departure and arriving time. It is therefore essential to control the evaporation of atoms. For this purpose, a direct electric potential V_0 slightly below the evaporation threshold is applied to the tip. In order to trigger the evaporation, an ultra-short electric (V_p) or laser pulses are superimposed at a frequency of several tens of kHz. It should be noted that the use of laser pulses was developed to characterize semiconductor and insulator materials. Pulses can trigger a timer which will stop when the evaporated atoms are collected by the ion detector located in front of the sample (Figure II.9). The ToF and the correlated value of the potential applied to the tip are then used to calculate from the conservation of energy the mass to charge ratio of detected atoms. Indeed, using the assumption that the acceleration time of the evaporated atom is negligible compared to the duration of the time of flight, it can be deduced that:

$$ne(V_0 + V_P) = \frac{M\upsilon^2}{2} \qquad \text{(Equation II.2)}$$

where M is the mass of the ion, υ is the velocity, n is the charge state, e is the electron charge, V_0 is the direct voltage and V_p is the pulsed potential respectively. The mass to charge ratio can be then written as:

$$\frac{M}{n} = 2e(V_0 + V_P)\left[\frac{t_\upsilon}{L}\right]^2 \qquad \text{(Equation II.3)}$$

Where, t_v is the time of flight and L the flight distance. Note that by using laser pulses, V_p is replaced by zero in Equations II.2 and II.3. The value of M/n allows to identify the nature of the detected ions.

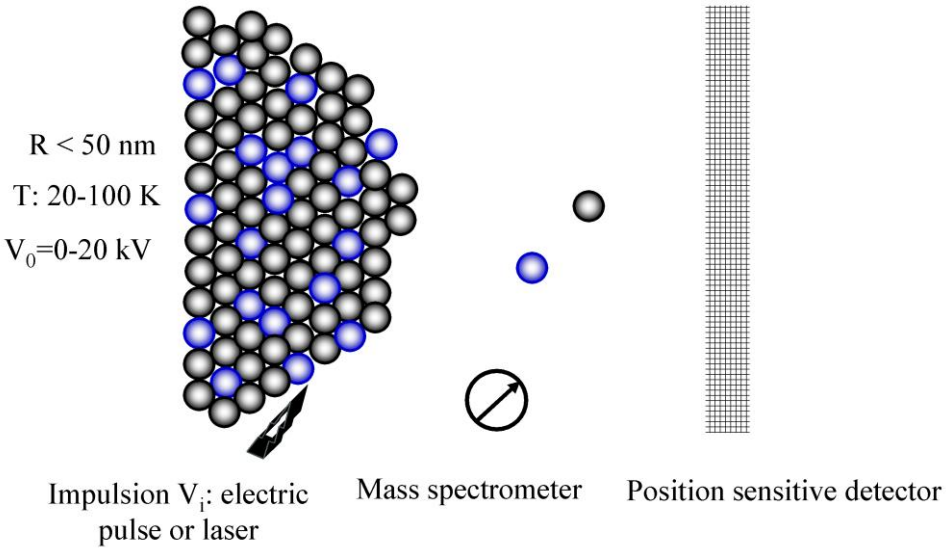

Figure II.9– Principle of the atom probe tomography. Dots with two colors: black and blue represents different elements.

During the specimen analysis, a mass spectrum is obtained and allows the identification of each chemical element constituting the sample and the number of atoms. The atomic concentration C of each element in the analyzed volume are simply obtained by counting the number of atoms in each peak of mass spectrum which is given as the mass-to-charge state ratio in unit of atomic mass (u.m.a.). The statistical incertitude of measurement is given as:

$$2\sigma = \Delta C = 2\sqrt{\frac{C(1-C)}{N}} \qquad \text{(Equation II. 4)}$$

Where, N is the total atom number.

II.2.3.2 Analyzed volume

The methods to reconstruct a volume analyzed by APT were detailed in the past [37]. APT is a projection microscope and the evaporated atoms can be considered as coming from the projection point located at a depth (1 + m) R of the surface of the tip, where m is a dimensionless geometric factor as illustrated in Figure II.10 (chosen to be 0.6 in this work). The coordinates of the ion impacts on the detector allow to calculate by reverse projection the original position of atoms on the surface of the tip. The depth of each atom is determined from their order of arrival. We can reconstruct the volume analyzed in three dimensions with a magnification η of the order of 10^7. The magnification η is given by Equation II.5:

$$\eta = \frac{L}{(1+m)R} \qquad \text{(Equation II. 5)}$$

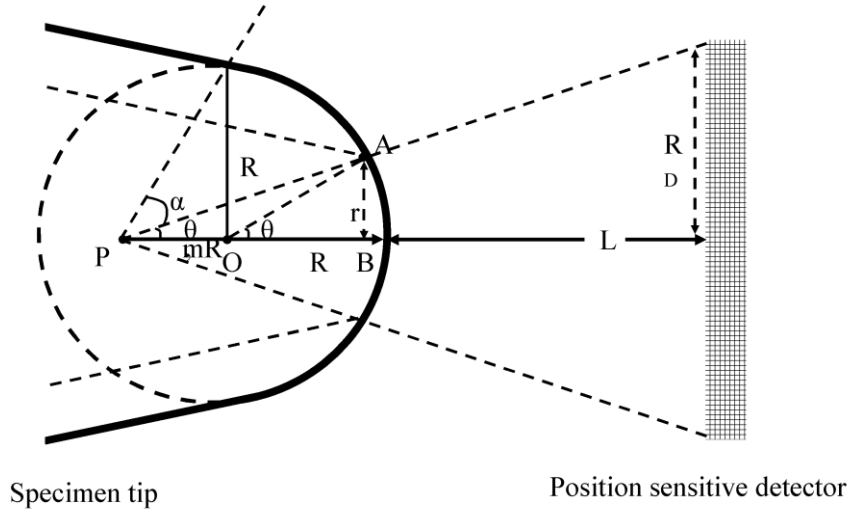

Figure II.10 – Schematic illustration of specimen projection and analyzed volume of APT when the specimen tip is perpendicular to position sensitive detector. At work distance d for APT with conventional configuration, the projection and analyzed volume is presented with black dot dashed line.

The analyzed volume of tip represents the maximum volume that APT can investigate at a certain experimental conditions. APT being a projection microscope, the analyzed volume is directly related to the analyzed surface which depends on the tip radius and the distance L. Several protocols have been designed for APT reconstruction [37, 38]. The standard global reconstruction technique of APT is based on a protocol designed by Bas et al.[37]. This model is based on the point projection and geometry model. Considering the geometry of a typical specimen (illustrated in Figure II.10), the following relation is obtained:

$$OB\tan\theta = (PO + OB)\tan\theta' \qquad \text{(Equation II. 6)}$$

$$\frac{\tan\theta}{\tan\theta'} = \frac{PO + OB}{OB} = \frac{PO}{OB} + 1 = \frac{mR}{R\cos\theta} + 1 \qquad \text{(Equation II.7)}$$

θ’ and θ are very small, thus,

$$\tan\theta = (m+1)\tan\theta'$$

$$\theta = (m+1)\theta'$$

From the point projection, the launch angle θ’ is given by the following expression, as illustrated in Figure II.10:

$$\tan\theta' = \frac{R_D}{(m+1)R + L} \approx \frac{R_D}{L} \qquad \text{(Equation II. 8)}$$

where R_D is the radius of detector. Thus, the radius of analyzed volume r can be written as

$$r = R\sin\theta = R\sin[(m+1)\theta'] = R\sin\left[(m+1)\arctan\frac{R_D}{L}\right] \qquad \text{(Equation II. 9)}$$

From the Equation II.9, there are two possibilities to increase the analyzed volume considering the instrumentation parameters, namely, decrease the working distance L and increase the radius of detector R_D. However, it is not always practicable because the mass resolution will decrease during the decrease of working distance which is related to the ToF. For example, the most suitable working distance in our APT (CAMEACA LAWATAP) is chosen to be 98 mm with a detector radius of 38.5 mm by taking into account of both the analyzed volume and the detection limit compared to the working distance of 90 mm for other APT with a detector radius of 38 mm (CAMEACA LEAP 3000X Si). It should be noted that the working distance of APT is fixed not as in the condition of electron microscope. Thus, it is not so practical to change the instrumentation parameter to increase the analyzed volume for having the specimen surface information. From Equation II.9, the radius r of analyzed volume is calculated to be 0.56 R.

It is worth noting that when the specimen tip is perpendicular to position sensitive detector, the analyzed volume is only one portion compared to the entire specimen tip volume as shown in Figure II.11. Therefore the sidewall surface of the tip can not be analyzed. The practical way to obtain information about the surface of the specimen is to incline it as illustrated in Figure II.11. In this tip configuration, one portion of the tip surface can be analyzed by APT (the shadow region). The analysis of the sidewall surface of NWs by APT is based on this idea.

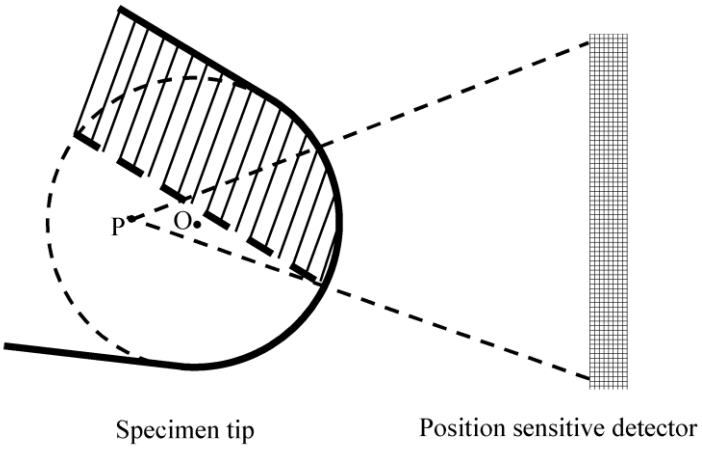

Figure II.11 – Schematic illustration of specimen projection and analyzed volume of APT when the specimen tip is inclined to position sensitive detector. The shadow region represents the analyzed volume which includes the tip surface information.

In order to investigate the specimen surface, the minimum inclined angle α (illustrated in Figure II.10) can be calculated as follows:

$$\tan\alpha = \tan[(\alpha+\theta')-\theta'] = \frac{\tan(\alpha+\theta')-\tan\theta'}{1+\tan(\alpha+\theta')\tan\theta'} = \frac{1/m - R_D/L}{1+R_D/mL} \qquad \text{(Equation II. 10)}$$

Where, m, R_D and L are equal to 0.6, 3.85 and 9.8 cm respectively. Then, α is 38 °. If one wants to analyze the specimen sidewall surface, the inclined angle must thus be larger than 38 °.

After data treatment, the spatial distribution of atoms in the analyzed volume can be observed in 3D at the atomic scale. Figure II.12 presents an example of 3D reconstruction obtained on a pulsed laser deposition-grown $Zn_{0.9}Co_{0.1}O$ thin films [39].

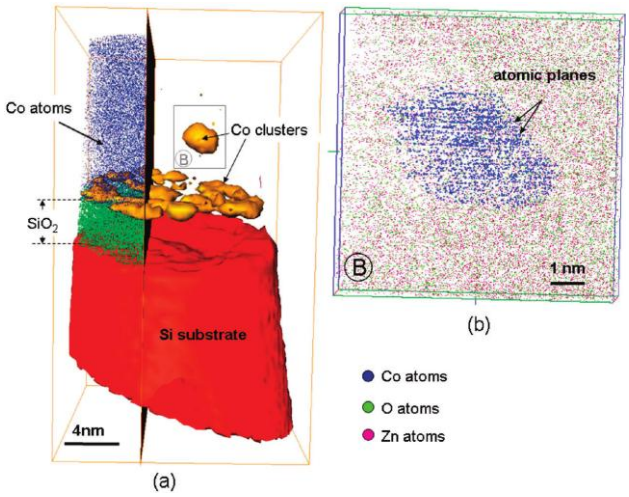

Figure II.12 – 3D Image of the cluster decoration of the Zn(Co)O/substrate interface (in yellow, iso-concentration surface at 30 Co at.%), (b)magnification of the Co cluster in region B. Adapted from [39].

II.2.3.3 Laser-Assisted Wide Angle Tomographic Atom Probe (LAWATAP)

To investigate semiconductor or insulator materials by APT, a nano second or femtosecond laser impulsion source need to be used for replacing the electric pulses [40]. The choice of a laser pulse with very short duration (femtosecond laser) increases the APT mass resolution [41]. However, the mechanism of interaction between laser and material is not fully understood.

In this work, LAWATAP (CAMECA) was used for Si NW investigation. The laser system is an Ytterbium-doped laser with the impulsion of 400 fs. The total laser power reaches 1 W with 100 KHz. Three wavelengths were chosen, namely, infrared ($\lambda \sim 1030$ nm), green ($\lambda \sim 515$ nm) and ultraviolet ($\lambda \sim 343$ nm). It has been found that at UV work condition, the characterization of Si NWs have higher success rate with a good mass resolution ($(M/\Delta M)_{50\%} = 348$).

Considering the temperature of investigation, LAWATAP can work in the range of 20 K to 80 K. In this work, four different temperatures were tested, namely, 20 K, 40 K, 60 K and 80 K at UV laser source. No temperature dependent impurity (e.g. B and In) concentration of Si NW is found. It should be noted here that the evaporation voltage applied on tip at higher temperature (80 K) is smaller than the one at lower temperature (20 K) with the other experimental condition kept the same. With these conditions, the specimen can be investigated successfully without rupture at smaller applied voltages. Thus, in this work, all the NW investigations are performed at 80K.

The laser power is also an important parameter which should be chosen appropriately. The choice of an appropriate laser power is done by choosing the pulse fraction. The pulse fraction can be defined as:

$$\frac{V_T - V_0}{V_0} \qquad \text{(Equation II. 11)}$$

Where V_T is the voltage necessary for atom evaporation without laser pulse and V_0 is the voltage applied on the specimen tip. In this work, all the Si NW investigations are performed by using the laser power which has a pulse fraction about 20 %.

The multi material characterization techniques such as FIB, SEM, TEM and APT are used in this work. For a general view, a schematic illustration of resolution and analyzed volume for each technique is presented in Figure II.13. Each technique has its advantages and limitations. For example, APT characterization gives excellent results for the distribution and concentration of atoms but it gives little information of the material structure. Conversely, TEM gives useful and valuable structure information. Considering the specimen preparation for APT and TEM, the combined use of FIB and SEM dual beam work platform is essential. In this work, the results of these multi techniques for Si NW characterization are compared and discussed.

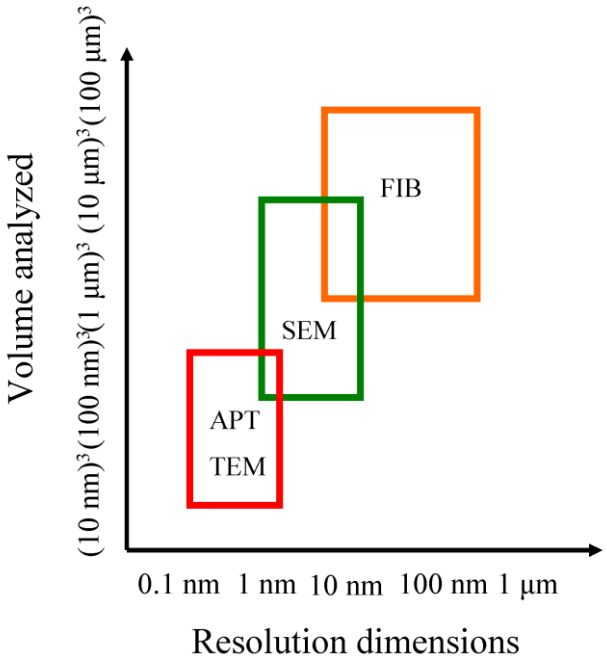

Figure II.13 – Schematic representation of resolution and volume analyzed of four types of characterization tools.

II.2.4 Development of sample preparations for atom probe

The main difficulty for the analysis of a single NW using the APT technique is related to the specimen preparation. Indeed, in our study, the LAWATAP instrument requires to mount a single NW at the top of a support tip. Moreover, the analyses of specific areas of the NW required much attention. Thus, the development of specimen preparation methods for APT investigation was the key point in this work. Three different types of specimen preparation methods for NW characterization by APT were developed and are described in this part. It should be noted here that these three specimen preparation methods are developed specially for LAWATAP series of CAMECA not for other APT series such as LEAP of CAMECA.

II.2.4.1 Si nanowires grown on Si pillars

The concept of this preparation method consists in the growth of a single Si NW on a micro pillar which is subsequently manipulated in the SEM-FIB work station. This method includes three steps. The first step consists in the deposition of few catalyst droplets on the top of an array of Si micro pillars. The arrays of Si micro pillars (6×6 μm^2 and 54 μm in height) are fabricated from Si wafers with a [111] orientation,(n-type doped (0.03-0.05 Ω·m)), using the conventional micro fabrication process [42]. The second step consists in the growth of the Si NWs in a CVD growth chamber. These steps are similar to the one described in the literature [43-45]. The purpose of these two steps is to grow a single NW on the top surface of a micro pillar. In the final step which is developed specially for LAWATAP, a single micro pillar with Si NWs at the top is manipulated and mounted on a pre-prepared W support tip.

In order to be able to analyze a single Si NW located at the top of a micrometric silicon pillar, the number density of NWs must be controlled during the growth. In the present case, Si NWs are grown from Au catalyst droplets. Thus, the control of the number density of Au droplets allows the control of the number density and diameter range of Si NWs. Several methods can be used for Au droplets deposition on Si substrate, for example, using Au colloids [46, 47] and Au thin film annealing [48, 49]. In this work, an in-situ Au evaporation method was used. In order to obtain different Au droplet number densities, the gold droplets were formed directly by gold deposition on a heated Si (111) surface in Ultra High Vacuum (UHV). Three different substrate temperatures were used: 400 ℃, 430 ℃ and 460 ℃ using the same deposition pressure of 8-8.6 $\times 10^{-10}$ mbar. The Au droplet density and their diameters can

be controlled by the Au evaporation rate and the substrate temperature via the Ostwald ripening process. Following these three conditions, three different densities of gold droplets were obtained. It was shown that the condition with T = 430 ℃ is the optimal one for the Au droplet deposition (Figure II.14 (a)). Indeed, using this condition, few Au droplets are successfully formed on the top of Si micro pillars, allowing the subsequent Si NWs growth for APT analysis. Si NWs can be successfully grown on these Si micro pillars (Figure II.14 (b)).

The final step of the procedure is the manipulation of the micro pillar itself. This is performed using the conventional lift-out dual beam method. This *in-situ* process is realized in a SEM-FIB dual-beam platform. The process can be described as follows. Step one: choosing a suitable Si micro pillar using micro tweezers (Figure II.14 (c)). Step two: cutting the Si pillar by using the SEM-FIB dual beam (Figure II.14 (d)). Step three: welding of a Si pillar on a pre-prepared W support tip with GIS by depositing Pt as the solder in IBID mode (Figure II.14 (e)). A Si pillar with several Si NWs can be prepared using this method (Figure II.14 (e)). For the purpose of APT analysis (only a single Si NW on the Si pillar), the best Si NW (best orientation and length) can be kept and the others have to be eliminated using FIB. It should be noted here that a great attention must be paid to the Si NWs during the FIB process because of the risk of introduction of Ga atoms and their related damages. The as-prepared specimen is then introduced in the APT chamber for analysis. This method is very time consuming due to the involvement of several difficulties such as the low density of Si NWs grown on a single pillar and the manipulation of the Si pillars. Moreover, the APT characterization will begin from the end growth region of Si NW which is a specific region non representative of the whole Si NW due to unstable growth conditions during the stop of the gas precursor and the slow down of the temperature.

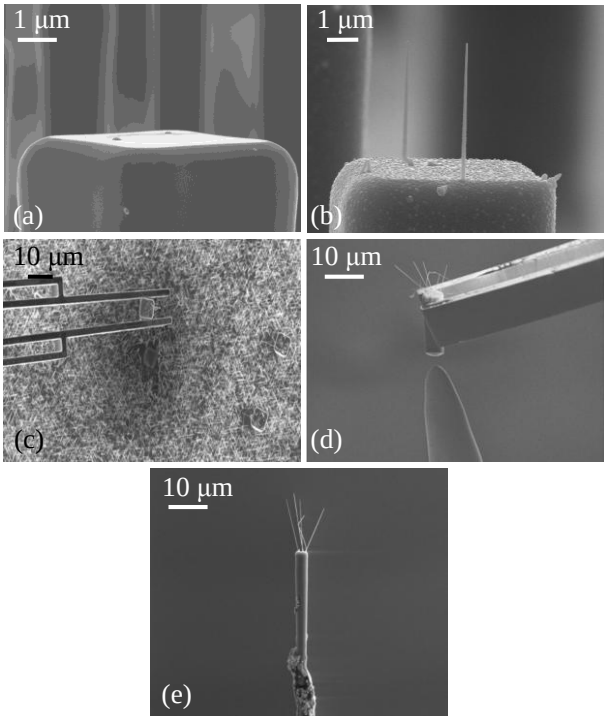

Figure II.14 – Scanning electron microscopy images of specimen preparation with Si NWs grown on Si micro pillars. (a) Au droplets on Si micro pillar surface. Two Au droplets are deposited successfully on a Si pillar at T = 430 ℃. (b) Growth of Si NWs on Si micro pillar using CVD process. The Si NWs are perpendicular to the Si (111) pillar. (c) Lift-out of a Si micro pillar with Si NWs grown on the top. Selection of a Si pillar with micro tweezers and cutting the Si pillar from the substrate by FIB. (d) Welding the Si pillar with a pre-prepared W tip by GIS using Pt as solder. (e) Image of the whole structure consisting of NWs, a Si pillar and a W tip.

II.2.4.2 Mounting of a single Si nanowire on a support tip

In this part, an efficient specimen preparation method is presented, namely, the direct welding of a single Si NW on a tungsten (W) support tip without the intermediate *in-situ* lift-out technique. Compared to the previous one and with the feedback of experience, this method is more convenient and efficient. Only two steps are involved in this method. The first step consists in catching a single Si NW with a W tip under optical microscopy (OM). With this method, either the top end or bottom end can be chosen to perform analysis of Si NW. Indeed, as the morphology of Si NWs is not a perfect cylinder but rather a cone due to tapering effect during the growth [50-52], the top or bottom ends are easily distinguished by

Si NW iridescence as shown in Figure II.15. Figure II.15 is an image of Si NWs scratched from the growing Si substrate.

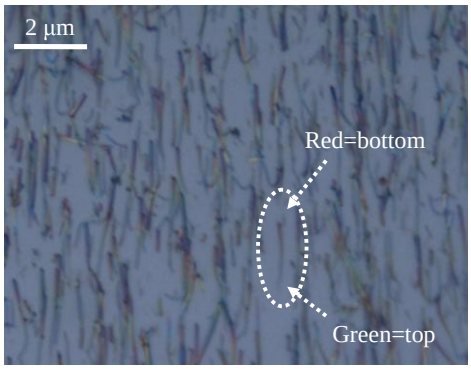

Figure II.15 – Optical microscopy image of horizontal Si NWs scratched on a Si substrate. The change of color along an individual Si NW can be clearly observed because of light iridescence. The colors at top end (Au droplet) and at bottom end are green and red respectively.

The second step is the welding of Si NW with the W support tip. The selection of an individual Si NW, in specific direction, is performed with a W tip. The contact between the Si NW and the W tip then needs to be reinforced because of the high electrostatic force applied to the Si NW during APT analysis. The reinforcement process is realized by Pt deposition in EBID mode with GIS. Figure II.16 (a) and (b) present SEM views of Si NW before and after welding by GIS. In this case, the bottom end of the Si NW has been chosen for APT analysis.

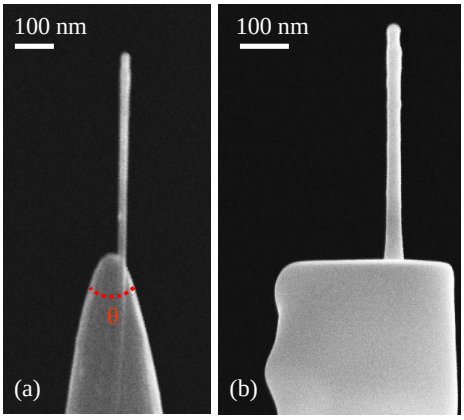

Figure II.16 – Scanning electron microscopy view of a Si NW welded on a W tip. (a) Before and (b) after Pt deposition by GIS. The bottom end of Si NW is at the top of the specimen.

Si NWs prepared from this method are usually inclined with respect to the APT detector because of the apex angle of W support tip. Whether Si NW is perpendicular or inclined to APT detector depends on the W tip apex angle θ (Figure II.16 (a)). A very small

apex angle allows Si NWs to be perpendicular to the detector, whereas, a relative large angle allows a Si NW to be inclined with respect to the detector. The W tip apex angle is roughly controlled during the electropolishing of support tip. Using this convenient and efficient method, NW volume or surface characterization and NW bottom or top characterization by APT are easily performed. Moreover, this method can be applied to NWs grown not only by VLS but also by SLS.

II.2.4.3 Horizontal Si nanowires for radial characterization

The previous method is efficient for preparing NW for APT. However, it does not allow the radial characterization of a NW. The preparation method to analyze the radial direction is also based on the conventional lift-out method but it is more complicated and time-consuming. The procedure of this method is described as follows. Step one: A single Si NW is deposited horizontally on a flat Si substrate (Figure II.17 (a)). Step two: Deposition of Pt and W as protective layers on top of the Si NW as in the conventional lift-out method (Figure II.17 (b)). The deposition of different materials such as Pt and W is used as the mark layer. Both deposition processes (Pt and W) is achieved by GIS in dual-beam platform. Step three: the conventional lift-out of a block including the single Si NW (Figure II.17 (c)). Step four: welding the block with a pre-prepared W support tip. As indicated in Figure II.17 (d), a single Si NW is found in the centre region of block. Figure II.17 (e) is a cross-section zoom of a Si NW covered with W. The Si NW cross-section is found to be a hexagon. Step five: annular milling of block using FIB. Figure II.17 (f) presents a multilayer structure comprising Si, W, Si NW, Pt and W from top to bottom. Si NW must be kept in the centre region during FIB process. But this is a very difficult process because of the great difference of Ga atom sputter yields between Si and W at 30 keV Ga ion beam [53]. For this reason, the final milling process is not homogeneous any more. There is a great risk of milling the Si NW. Figure II.17 (g) represents one portion of the Si NW after milling. It should be noted here that this specimen method is still under development. The main difficulty is to place the NW in the centre of the APT specimen tip without any contamination of Ga atoms.

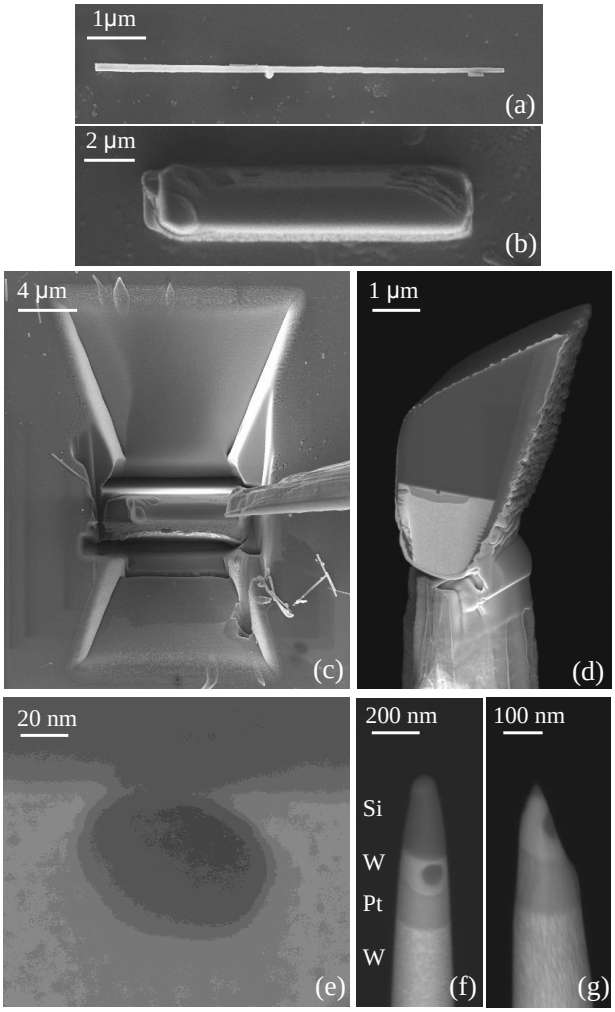

Figure II.17 – Scanning electron microscopy images of the processes required for a radial Si NW characterization (a) Deposition of a single Si NW on a Si substrate. (b) Using GIS deposition system, a Pt layer is deposited on the Si NW as a protective layer during the lift-out process. (c) Lift-out of the block containing the single Si NW (d) Welding of the block with a pre-prepared W tip. (e) Cross-section view of the Si NW (f) Scanning electron microscopy image of the block after annular milling. The Si NW must always be kept in the centre region of the block during milling. (g) Scanning electron microscopy image of the block with a portion of the Si NW.

In this chapter, we have presented in detail the different experimental techniques (elaboration and characterization) used in this work. Concerning the characterization techniques, APT is chosen as the major technique in this work. Especially, the specimen preparation methods of NWs for APT are given with great details. To characterize a single NW by APT, we have developed several specimen preparation methods which are an important issue in this work.

Bibliography of chapter II

[1] A. A. Ayon, R. L. Bayt, and K. S. Breuer, Smart Mater. Struct., 10, 1135 (2001)
[2] C. Hibert, CMI Annual Review, 18 May (2004)
[3] M. L. Hitchman, and K. F. Jensen, Chemical Vapor Deposition: Principles and Applications, Academic Press (1993)
[4] M. A. Herman, and H. Sitter, Molecular Beam Epitaxy: Fundamentals and Current Status, Springer (1996)
[5] C. W. Oatley, J. Appl. Phys., 53, R1 (1982)
[6] J. Goldstein, D. E. Newbury, D. C. Joy, C. E. Lyman, P. Echlin, E. Lifshin, L. Sawyer, and J. R. Michael, Scanning Electron Microscopy and X-ray Microanalysis, Springer, 3rd edition 537 (2003)
[7] M. Knoll, Zeitschrift für technische Physik 16, 467 (1935)
[8] M. Nastasi, J. Mayer, and J. K. Hirvonen, Ion-Solid Interactions: Fundamentals and Applications, Cambridge University Press (1996)
[9] N. Yao, and Z. L. Wang, Handbook of Microscopy for Nanotechnology, Springer, 326 (2005)
[10] J. Orloff, L. Swanson, and M. W. Utlaut, High resolution focused ion beams: FIB and applications, Springer, 205 (2002)
[11] L. A. Giannuzzi, and F. A. Stevie, Introduction to focused ion beams, Springer, 143 (2004)
[12] J. Melngailis, Journal of Vacuum Science & Technology B: Microelectronics and Nanometer Structures, 5, 469 (1987)
[13] P. Sigmund, Phys. Rev., 184, 383 (1969)
[14] J. Orloff, Rev. Sci. Instrum., 64, 1105 (1993)
[15] S. Amelinckx, D. V. Dyck, J. V. Landuyt, and G. V. Tendeloo, Electron Microscopy: Principles and Fundamentals, Wiley-VCH (1997)
[16] L. Frey, C. Lehrer, and H. Ryssel, Applied Physics A: Materials Science & Processing, 76, 1017 (2003)
[17] S. Rubanov, and P. R. Munroe, Journal of Microscopy, 214, 213 (2004)
[18] L. A. Giannuzzi, and F. A. Stevie, Introduction to focused ion beams, Springer, 247 (2004)
[19] C. A. Volkert, and A. M. Minor, Materials Research Society, 32, 389 (2007)
[20] D. W. Saxey, J. M. Cairney, D. McGrouther, T. Honma, and S. P. Ringer, Ultramicroscopy, 107, 756 (2007)
[21] B. V. Leer, L. A. Giannuzzi, and Y. C. Wang, Microsc. Microanal., 15, 336 (2009)
[22] E. S. Sadki, S. Ooi, and K. Hirata, Appl. Phys. Lett., 85, 6206 (2004)
[23] L. van Kouwen, A. Botman, and C. W. Hagen, Nano Lett., 9, 2149 (2009)
[24] E. U. Donev, and J. T. Hastings, Nano Lett., 9, 2715 (2009)
[25] S. J. Randolph, J. D. Fowlkes, and P. D. Rack, Crit. Rev. Solid State Mater. Sci., 31, 55 (2006)
[26] M. D. Graef, Introduction to Conventional Transmission Electron Microscopy, Cambridge University Press, 136 (2003)
[27] E. Ruska, Zeitschrift für Physik A Hadrons and Nuclei, 87, 580 (1934)
[28] J. Ayache, L. Beaunier, J. Boumendil, G. Ehret, and D. Laub, Sample Preparation Handbook for Transmission Electron Microscopy: Techniques, Springer, 37 (2010)
[29] L. A. Giannuzzi, and F. A. Stevie, Micron, 30, 197 (1999)
[30] L. A. Giannuzzi, and F. A. Stevie, Introduction to focused ion beams, Springer, 201 (2004)

[31] D. B. Williams, and C. B. Carter, Transmission Electron Microscopy: A Textbook for Materials Science, Spinger, 2nd edition, 190 (2008)
[32] E. W. Müller, Zeitschrift für Physik A Hadrons and Nuclei, 131, 136 (1951)
[33] D. Blavette, B. Deconihout, A. Bostel, J. M. Sarrau, M. Bouet, and A. Menand, Rev. Sci. Instrum., 64, 2911 (1993)
[34] A. Cerezo, T. J. Godfrey, and G. D. W. Smith, Rev. Sci. Instrum., 59, 862 (1988)
[35] T. T. Tsong, Atom-Probe Field Ion Microscopy, Cambridge University Press, Cambridge (1990)
[36] M. K. Miller, Atom Probe Tomography: Analysis at the Atomic Level, Spinger (2000)
[37] P. Bas, A. Bostel, B. Deconihout, and D. Blavette, Appl. Surf. Sci., 87-88, 298 (1995)
[38] B. P. Geiser, D. J. Larson, E. Oltman, S. Gerstl, D. Reinhard, T. F. Kelly, and T. J. Prosa, Microsc. Microanal., 15, 292 (2009)
[39] R. Lardé, E. Talbot, P. Pareige, H. Bieber, G. Schmerber, S. Colis, V. Pierron-Bohnes, and A. Dinia, J. Am. Chem. Soc., 133, 1451 (2011)
[40] G. L. Kellogg, and T. T. Tsong, J. Appl. Phys., 51, 1184 (1980)
[41] B. Deconihout, F. Vurpillot, B. Gault, G. Da Costa, M. Bouet, A. Bostel, D. Blavette, A. Hideur, G. Martel, and M. Brunel, Surf. Interface Anal., 39, 278 (2007)
[42] H. J. Levinson, Principles of Lithography, SPIE Press (2005)
[43] D. E. Perea, J. L. Lensch, S. J. May, B. W. Wessels, and L. J. Lauhon, Appl. Phys. A, 85, 271 (2006)
[44] D. E. Perea, E. Wijaya, J. L. Lensch-Falk, E. R. Hemesath, and L. J. Lauhon, J. Solid State Chem., 181, 1642 (2008)
[45] R. A. Schlitz, D. E. Perea, J. L. Lensch-Falk, E. R. Hemesath, and L. J. Lauhon, Appl. Phys. Lett., 95, 162101 (2009)
[46] J. H. Woodruff, J. B. Ratchford, I. A. Goldthorpe, P. C. McIntyre, and Chidsey, Nano Lett., 7, 1637 (2007)
[47] F. Li, P. D. Nellist, and D. J. H. Cockayne, Appl. Phys. Lett., 94, 263111 (2009)
[48] C.-Y. Meng, B.-L. Shih, and S.-C. Lee, J. Nanopart. Res., 9, 657 (2007)
[49] F. Dhalluin, T. Baron, P. Ferret, B. Salem, P. Gentile, and J. C. Harmand, Appl. Phys. Lett., 96, 133109 (2010)
[50] P. Aella, S. Ingole, W. T. Petuskey, and S. T. Picraux, Adv. Mater., 19, 2603 (2007)
[51] H. Schmid, M. T. Bjork, J. Knoch, H. Riel, W. Riess, P. Rice, and T. Topuria, J. Appl. Phys., 103, 024304 (2008)
[52] W. H. Chen, R. Larde, E. Cadel, T. Xu, B. Grandidier, J. P. Nys, D. Stievenard, and P. Pareige, Physica Status Solidi (c), 8, 771 (2011)
[53] M. Nastasi, J. Mayer, and J. K. Hirvonen, Ion-Solid Interactions: Fundamentals and Applications, Cambridge University Press Appendix A (1996)

Chapter III

III Modeling the growth of group IV semiconductor nanowires

For NW applications, it is important to control precisely the different aspects of NW geometry such as NW length and growth orientation. Among these aspects, the NW length has more importance. For example, the growth of NWs with narrow length distribution can ensure a uniform contact when an array is grown. It also helps in collecting photons as far as the solar cell is considered. It should also be noted here that the growth of NWs with enough length is necessary for the APT analysis. For these reasons, we will concentrate on the study of the NW length in this chapter. Different parameters such as NW diameter and growth pressure can influence the NW length. Therefore, finding the physical rules that allow to predicting the NW length from the initial catalyst size at different growth conditions is essential for the future.

In this chapter, two different phenomena of VLS-grown NWs are presented and discussed as follows:

- As the length of the NWs is related to the growth rate, modeling the growth rate is described for NWs synthesized via the Chemical Vapor Deposition (CVD) and the Molecular Beam Epitaxy (MBE) respectively. Several models, with a gradual increase in complexity takes into account the different atomic pathways that can lead to the incorporation of atomic species into the NWs. From these models, a solution will emerge to narrow NW length distribution.

- NWs are generally observed to be tapered. We will investigate the growth parameters that govern a transformation from cylindrical NWs to conical NWs.

III.1 Experimental conditions

Au catalyst preparation

Si NWs are fabricated by the CVD method using Au droplets as catalyst according to the VLS mechanism [1]. In order to obtain Au droplets with different densities, the Au droplets are formed directly by Au deposition on a heated Si (111) surface in Ultra High Vacuum (UHV). For the process performed in UHV, two different temperatures are used, namely 430 ℃ and 460 ℃ keeping the same Au deposition pressure of 8-8.6 $\times 10^{-10}$ mbar. The

density and the diameter of Au droplets are determined by the evaporation flux rate and the temperature of the samples. Based on both temperatures, two different densities of Au droplets are obtained (Figure III.1): at high temperature, the density of Au droplets is smaller than the one obtained at low temperature, but the average droplets diameter is larger: 90 nm versus 55 nm at low temperature. For the preparation of Au droplets with a wider range of diameters, Au droplets are also prepared by evaporating a 2 nm thick layer of gold on an H-Si (111) chemically passivation surface. Regarding the gold droplet formation from the Au thin film, the sample was annealed at 700 ℃ for five minutes in the CVD chamber prior to NWs growth to lead to the dewetting of the film.

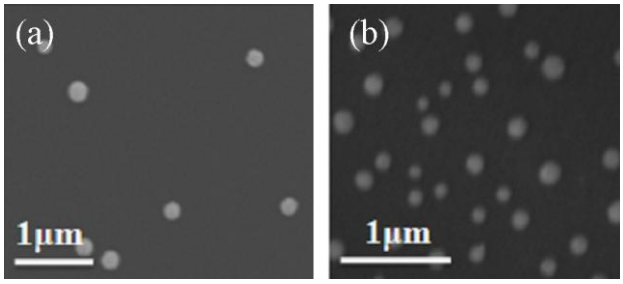

Figure III.1 – Scanning electron microscopy images of Au droplets on Si substrate with two different densities. Au droplets are fabricated with same evaporation flux but at two different temperatures: (a) 400 ℃ and (b) 430 ℃.

Si nanowire growth conditions

In the next step, Si NWs are grown by the CVD method at a temperature of 500 ℃ for 30 min. Silane and hydrogen are used as the precursor gas and the carrier gas respectively. Under what will be subsequently called a high pressure condition (Table III.1 (a)), the SiH_4 precursor with a flux rate of 50 Standard Cubic Centimeter per Minute (SCCM), is diluted in a mixture of H_2 with a flux rate of 50 SCCM in order to set the total pressure and the silane partial pressure in the CVD chamber to 0.8 mbar and 0.4 mbar respectively. As to the low pressure condition, SiH_4 is diluted in H_2 with a ratio of 12:150 (see Table III.1 (b)). The flux rate of SiH_4 is 12 SCCM and the total pressure is kept at 1.1 mbar, yielding a silane partial pressure of 0.08 mbar.

(a)

Pressure (mbar)	T (℃)	SiH_4 (sccm)	H_2 (sccm)	Time (min)
1.1	500	50	50	30

(b)

Pressure (mbar)	T (℃)	SiH_4 (sccm)	H_2 (sccm)	Time (min)
1.1	500	12	150	30

Table III.1 – Growth experimental conditions of Si NWs without dopant at (a) high silane partial pressure and (b) low silane partial pressure. Silane and hydrogen are chosen as the precursor and the carrier gas respectively.

SEM images are performed with a LEO FE 1530 microscope and examples of SEM images are shown in Figure III.2 (a,b,c). In order to precisely measure the base diameter of the Si NWs for the growth rate modeling and the investigations of the tapering effects, similar NW growths are performed on micro pillars. The micro pillars are fabricated from Si (111) wafers, n-type doped (0.03-0.05 Ω·m), using a standard lithography method [2]. Figure III.2 shows the same types of NWs grown either on a substrate (left column) or on a micro-pillar (right column)

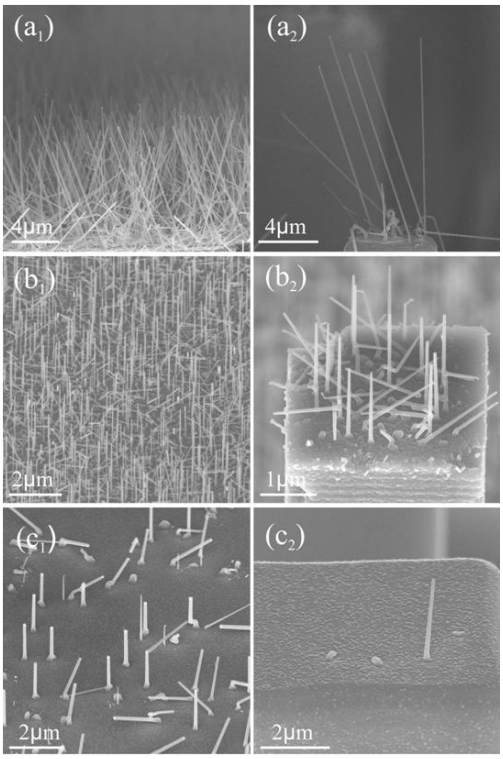

Figure III.2 – (a_1), (a_2); (b_1), (b_2) and (c_1), (c_2) Scanning Electron Microscopy images corresponding to the three different series of growth conditions on Si substrates (left) and Si

pillars (right) respectively. The silane partial pressure and the average catalyst diameter for growing the Si NWs are (a) 0.4 mbar, 55 nm; (b) 0.08 mbar, 55 nm and (c) 0.08 mbar, 90 nm respectively.

The measurement of different geometry parameters such as the length and the diameter are illustrated in Figure III.3, where a single Si NW grown with low pressure at low density is seen. The Au droplet is clearly visible on top of the NW shaft. Only NWs that show the Au droplet on top of the shaft are considered in the statistical analyses that are described later. In this case, the cross-section of Si NW is an irregular hexagonal with a faceted sidewall. This irregular hexagonal cross-section is usually approximated as a disk. L, D and d represent the NW length, its base diameter and its top diameter respectively. It should also be noted that the tilted angle of SEM platform during the measurement is also taken into account for the determination of the length.

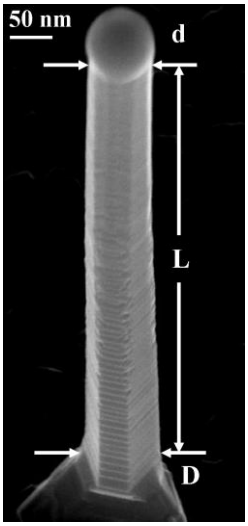

Figure III.3 – Scanning electron microscopy image where key geometrical parameters are defined. L, D and d represent the NW length, its base diameter and its top diameter respectively.

III.2 Growth rate (length) modeling

Generally, Si atoms for Si NW growth come from the decomposition of silane in CVD or the evaporation of Si atoms in MBE. The growth of NWs in the VLS mode requires that the majority of the Si atoms crystallize at the NW/droplet interface.

In the typical VLS growing system, the driving force of the growth process for a NW is the difference between the chemical potential of Si in the gas phase (precursor) μ_{Si}^{G} and in

the solid phase (NW) μ_{Si}^{NW} [3]. Due to the Gibbs-Thomson effect, for a NW with d as its diameter, the chemical potential of a NW can be written as follows [4]:

$$\mu_{Si}^{NW} = \mu_{Si}^{substrate} + \frac{4\Omega\gamma}{d} \qquad \text{(Equation III. 1)}$$

where Ω and γ are the specific volume of Si atom and the specific surface free energy of NW sidewall surface. Therefore, a relation concerning the chemical potential difference can be established as follows:

$$\Delta\mu_{Si} = \mu_{Si}^{G} - \mu_{Si}^{NW} = \mu_{Si}^{G} - \mu_{Si}^{substrate} - \frac{4\Omega\gamma}{d} \qquad \text{(Equation III.2)}$$

where $\mu_{Si}{}^{j}$ are the chemical potentials in the gas, NW and substrate respectively. Ω, γ and d are the specific volume of Si atom, the specific surface free energy and the diameter of NW respectively. At high precursor gas pressure, the comparison of the magnitude of the chemical potentials in the gas phase (G), the liquid droplet (L), on the NW sidewalls and on the substrate yields:

$$\mu_{Si}^{sub} \leq \mu_{Si}^{NW} \leq \mu_{Si}^{L} \leq \mu_{Si}^{G} \qquad \text{(Equation III.3)}$$

The chemical potential of the Si adatoms on the substrate and the sidewall has to be considered when the diffusion of Si adatoms is involved. If diffusion contributes to the growth rate, normally the catalyst droplet will collect the adatoms and this is achieved when the following relation is satisfied:

$$\mu_{Si}^{L} \leq \mu_{Si}^{adatom} \qquad \text{(Equation III.4)}$$

However, this relation can be reverse at certain NW growth condition. In that case, the Au-rich droplet is not a reservoir of Si atoms any more. In contrast, the NW will be decomposed by the Au-rich droplet and the species atoms will migrate outwards. This is a very special case and will be discussed in detail in chapter III.2.2.2.

Whatever the NW elaboration method is, CVD or MBE, the Au-rich droplet generally favors the growth causing the formation of a one-dimensional structure. The Si supersaturation generated in the Au-rich droplet induces the crystallization of Si atoms at the NW/droplet interface. An interesting and important question is through which pathway these Si atoms can be incorporated into the Au droplet. Considering the geometry of Au-rich catalyst droplets, there are two interfaces (vapor/droplet interface and NW/droplet interface) and one boundary, the Three Phase Boundary (TPB). All the main Si atom activities take place at these two interfaces and one boundary. As far as the Si atom transport is considered, the Si atoms that crystallized at the NW/droplet interface come from two principal pathways, namely, the impingement via the vapor/droplet interface and the diffusion from the sidewalls

through the TPB. Taking into account of these mechanisms, the growth rate of a Si NW is described by the following equation:

$$\frac{\pi d^2}{4\Omega}\frac{dL}{dt} = \frac{\pi d^2}{2} J_{impingment} + \pi d J_{diffusion} \qquad \text{(Equation III.5)}$$

The left term in Equation III.5 represents the Si atom crystallization. The first and second right terms represent the flows of atoms that are related to impingement and diffusion respectively. While L is the length of the Si NW, dL/dt represents the Si NW average growth rate. $J_{impingement}$ and $J_{diffusion}$ represent the impingement flux through the Au-rich droplet and the diffusion flux through the TPB respectively. The processes involved in $J_{impingment}$ may include the adsorption of the Si atoms onto the droplet, the desorption of Si atoms from the droplet to gas and the diffusion of adatoms on droplet surface. The quantity $J_{diffusion}$ contains Si atoms that diffuse after the adsorption of Si atoms to the sidewalls and substrate, before they have desorbed from the sidewalls or substrate.

III.2.1 Chemical Vapor Deposition (CVD)

The CVD synthesis is a complex process which involves the chemical reaction of precursors. Two surfaces need to be considered for the decomposition of the precursors: the Au droplet surface and the NW sidewall surface. The decomposition of silane occurs preferentially at the surface of the catalyst droplet but can also take place on the NW sidewall depending on the growth conditions. However, more silane molecules are supposed to be decomposed on the Au droplet surface than on the sidewall or the substrate. The decomposition of precursor is believed to be homogeneous due to the uniform heating in the growth chamber. The chemical reation of the silane decomposition has the following form:

$$SiH_4 \overset{T}{=} Si + 2H_2$$

At first, the sidewall diffusion of Si adatoms for CVD-grown NW is discussed at two growth conditions: low silane partial pressure and high silane partial pressure. If NWs are synthesized under low silane partial pressure, it was shown that Au atom diffusion away from the Au-rich catalyst droplet towards the NW sidewall can induce facetted sidewalls and form small clusters [5]. These small Au clusters can further act as nano catalyst droplets to decompose silane, favoring the adsorption of Si atoms on the NW sidewalls. These Si adatoms can move along the NW sidewall and take part in $J_{diffusion}$ or directly absorb on the NW sidewalls to induce a lateral growth. Because of the roughness of the sidewalls due to the presence of numerous facets, the diffusion of Si adatoms is generally small and can be

neglected for the NW growth rate in CVD. As for the high silane partial pressure, the Au atoms are not found to migrate on the NW sidewalls except at the end of the NW that corresponds to the interruption of the gas flux in the growth chamber and the gradual decreases of the Si partial pressure [6]. It is believed that the Si dangling bonds are saturated by silane molecules or byproducts (e.g. H_2) of the silane decomposition, preventing Au from migrating along the surface of the NW sidewalls. As a result, few Si atoms can absorb on the NW sidewalls and their diffusion can not significantly contribute to the growth rate of NW in CVD. Thus, in the CVD growth mode, the sidewall diffusion of Si atoms towards the catalyst droplet through TPB can be neglected compared to the direct impingement of Si atoms into the Au-rich droplet via the vapor/droplet interface.

The growth of the NW is predominantly related to the incorporation of Si atoms in the droplet from the reaction of silane with the droplet, yielding the simplified equation:

$$\frac{\pi d^2}{4\Omega}\frac{dL}{dt} = \frac{\pi d^2}{2} J_{impingment} \qquad \text{(Equation III. 6)}$$

The corresponding schematic illustration for the NW growth mechanism is illustrated in Figure III.4. The solid and hollow arrows represent the impingement through the Au-rich droplet surface and the crystallization at the interface between Au-rich droplet and NW respectively.

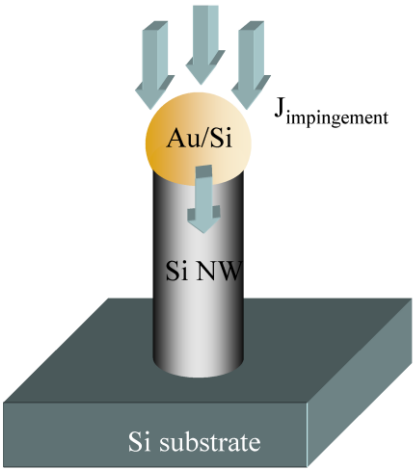

Figure III.4 – Schematic illustration of the crystallization of the Si NW from the incorporation of Si atoms from the droplet only.

The contribution of $J_{impingement}$ can be done in two ways, based on an empirical model or on a pressure-based model.

III.2.1.1 Empirical model

The empirical model has been proposed by Givargizov to fit the experimental data obtained from CVD-grown Si NWs [3]. The growth rate was considered proportional to the square of the effective supersaturation of the vapor relative to a NW. It took into account the Gibbs-Thomson effect. The empirical expression [$dL/dt = k(\Delta\mu_{G\text{-}S}/k_BT)^2 = k(\Delta\mu_0/k_BT - 4\Omega\gamma/dk_BT)^2$] has been used to fit the data set of this work. The best fit curves obtained are plotted in Figure III.5 (violet and grey curves). The fitting parameters are k = 17 nm/s and $\Delta\mu_0/k_BT$ = 0.43 at low silane partial pressure and k = 17 nm/s, $\Delta\mu_0/k_BT$ = 0.8 at high silane partial pressure. The value of supersaturation $\Delta\mu_{G\text{-}S}$ depends on the growth pressure whereas the coefficient of crystallization k depends on the growth temperature. It can be concluded from Figure III.5 that a good agreement between the experimental data and the model occurs for NWs with diameters above 100 nm but not for the ones with smaller diameters. In this growth model, the growth rate is related to the variation of the Si chemical potential between the gas phase and Si NWs. However, the growth rate should be kinetically controlled by the decomposition of silane at the surface of the Au-Si rich droplet as proposed by Wagner [1]. In such a case, the expression of the growth rate becomes:

$$\frac{dL}{dt} = \exp\left[A\left(\frac{\Delta\mu_{Si}^{G-L^{\infty}}}{k_BT} - \frac{4\Omega\gamma_{GL}}{dk_BT} \right) \right] \qquad \text{(Equation III.7)}$$

Again, the right hand term corresponds to the incorporation of Si atoms into the droplet. L^{∞} is a liquid droplet with an infinite radius. A is the coefficient of crystallization (nm/s) and $4\Omega\gamma_{GL}/k_BT$ is related to the Gibbs-Thomson effect, where γ_{GL} is the specific surface free energy of droplet surface which is assumed to be 0.85 J/m^2 [7]. The value of T and Ω are 773 K and 0.02 nm^3 respectively.

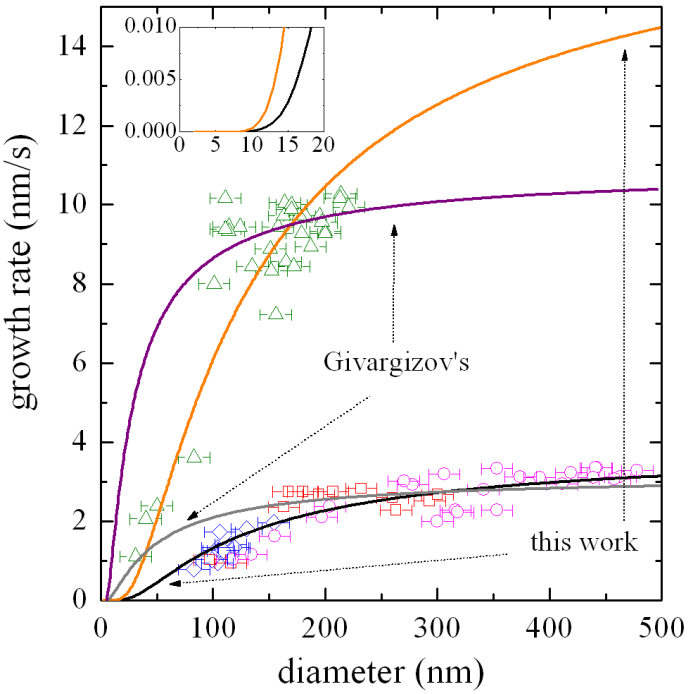

Figure III.5 – Comparison of growth rates of Si NWs as a function of the NW diameter for different CVD conditions: same growth temperature but different silane partial pressures. The triangles (△) correspond to a silane partial pressure of 0.4 mbar, whereas the squares (□), diamonds (◇) and circle (○) correspond to a silane partial pressure of 0.08 mbar. The Au droplets for triangle, square and diamond conditions are obtained by Au deposition in UHV. The density of Au droplets for the triangle and diamond conditions is higher than for the square condition. The Au droplet for the circle condition is obtained by annealing a Au thin film. The violet and grey curves correspond to the fit with Givargizov's model [3]. The yellow and black curves correspond to the empirical model proposed in this work (Equation III.6).

The best fit to the experimental data (yellow and black curves in Figure III.5) is obtained for A = 17 nm/s and $\Delta\mu_{Si}^{G-L^\infty}/k_BT$ = 0.08 at low silane partial pressure and A = 17 nm/s, $\Delta\mu_{Si}^{G-L^\infty}/k_BT$ = 0.17 at high silane partial pressure. In both cases, the fitting parameter A which is the crystallization rate is kept constant because the dominant mechanism for Si NW axial growth rate is the incorporation of Si atoms into the droplet. As the supersaturation is defined by the difference of chemical potential between the gas supply phase and the liquid droplet collector, increasing the gas pressure leads to the increase of the supersaturation, consistent with the variation of $\Delta\mu_{Si}^{G-L^\infty}$ deduced from the fitting procedure.

For comparison, Equation III.7 has also been applied to the Givargizov's data extracted from the literature [3]. Figure III.6 shows the data sets and the curves using

Equation III.7. The coefficient of crystallization A is kept constant to 37nm/s. This value is larger than the one (17 nm/s) used for fitting our experimental data, because the coefficient of crystallization A depends on the growth temperature. The growth temperature used in this work was 1000 ℃ instead of 500 ℃ in our work. It is clearly observed that the growth rate for small and large diameters is well reproduced using Equation III.7. The constant growth rate for large diameters strongly supports the hypothesis of this empirical model: the diffusion mechanism may not need to be taken into account. It is consistent with the data of Figure III.5 (yellow curve).

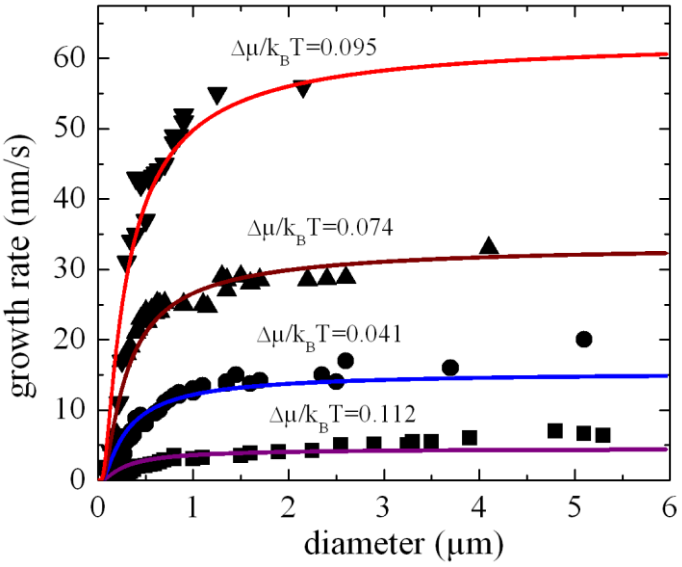

Figure III.6 –Data extracted from Givargizov's work [3] and fitted with the model presented in this work. These four curves have the same value of A= 37 nm/s. The supersaturation $\Delta\mu_{Si}^{G-L^{\infty}}/k_BT$ *for each condition has the value following: 0.041; 0.074; 0.095 and 0.112.*

In conclusion, the experimental data of CVD-grown Si NWs are well fitted with a model that takes into account of the effect of curvature of the lateral surface. Both experimental data and growth model reveal that the growth rate of CVD-grown NW increases with its diameter and will reach a saturation value at a certain diameter due to the weakening of the Gibbs-Thomson effect. In addition, a higher chemical potential in the catalyst droplet favors the growth of longer NWs. While the variation of the chemical potential is related to the magnitude of the pressure, the quantity $J_{impingement}$ can be expressed as a function of the pressure, as described in the next paragraph.

III.2.1.2 Pressure-based model

During the NW growth, the precursor related to silane can be assumed to be an ideal gas because of its low pressure. According to Hertz-Knudsen equation, the incident Si atom flux $J_{impingment}$ can be written as follows:

$$J_{impingment} = \frac{P_{effective}}{\sqrt{2\pi m k_B T}} = \frac{P_{Si} - P_L}{\sqrt{2\pi m k_B T}} = \frac{\alpha P_V - P_L}{\sqrt{2\pi m k_B T}} \qquad \text{(Equation III.8)}$$

where $P_{effective}$ is the effective vapor pressure, P_{Si} is the surrounding Si atom pressure, P_V is the silane partial pressure with α as the sticking coefficient and P_L is the equilibrium liquid droplet pressure. m, k_B and T are the Si atom mass, the Boltzmann constant and the NW growth temperature respectively. For the droplet, the chemical potential $\Delta\mu_L$ follows the Gibbs-Thomson equation:

$$\Delta\mu_L = k_B T \ln\frac{P_L}{P_\infty} = \frac{4\Omega\gamma}{d} \qquad \text{(Equation III.9)}$$

where Ω and γ are the specific volume of Si atom and the specific surface free energy of NW sidewall surface. P_∞ is the vapor pressure for a droplet with infinite diameter which is a constant at certain temperature.

A derivation of Equation III.8 can be obtained by using Equation III. 9

$$J_{impingment} = \frac{\alpha P_V - P_\infty \exp\frac{4\Omega\gamma}{dk_B T}}{\sqrt{2\pi m k_B T}} \qquad \text{(Equation III.10)}$$

Thus, using Equation III.6 and 10, the Si NW growth rate for CVD method can be written as:

$$\frac{dL}{dt} = \frac{2\Omega\left(\alpha P_V - P_\infty \exp\frac{4\Omega\gamma}{dk_B T}\right)}{\sqrt{2\pi m k_B T}} \qquad \text{(Equation III.11)}$$

According to Equation III.11, at an unstable equilibrium state (dL/dt=0), the critical diameter can be calculated as:

$$d_C = \frac{4\Omega\gamma}{k_B T}\ln\frac{P_\infty}{\alpha P_V} \qquad \text{(Equation III.12)}$$

Then, using the Equation III.12, the Equation III.11 can be written as:

$$\begin{aligned}\frac{dL}{dt} &= \frac{2\Omega\alpha P_V}{\sqrt{2\pi m k_B T}}\left[1 - \exp\left(\frac{4\Omega\gamma}{k_B T}\left(\frac{1}{d} - \frac{1}{d_C}\right)\right)\right] \\ &\approx \frac{2\Omega\alpha P_V}{\sqrt{2\pi m k_B T}} \times \frac{4\Omega\gamma}{d_C k_B T}\left(1 - \frac{d_C}{d}\right) = K\left(1 - \frac{d_C}{d}\right)\end{aligned} \qquad \text{(Equation III.13)}$$

with $K = \frac{2\Omega\alpha P_V}{\sqrt{2\pi m k_B T}} \times \frac{4\Omega\gamma}{d_C k_B T}$ which equals to the growth rate when the NW diameter d→∞ where the Gibbs-Thomson effect can be neglected. The parameter K clearly indicates that the NW growth rate increases with the growth pressure (as observed in this work and in the literature [8]) and decreases with the growth temperature [9, 10].

Integration of the Equation III.13 at the total NW growth time t leads to

$$\int dL = \int K(1-\frac{d_C}{d})dt \qquad \text{(Equation III.14)}$$

We can obtain $Ld=Kt(d-d_C)$. The critical diameter d_C then can be deduced from the fitting of experimental data (Figure III.7) and d_C is equal to 23 nm and 76 nm at high (0.4 mbar) and low (0.08 mbar) silane partial pressure respectively. It should be noted that the critical diameter in this work is larger than the one reported in the literature (d_C=25 nm at a silane partial pressure of 0.054 mbar) [11]. The critical diameter is a value that deduced from the fitting of experimental data. Therefore, the very large value of critical diameter in this work is due to the lack of experimental data of NWs with small diameter (no catalyst droplet with small diameter is prepared).

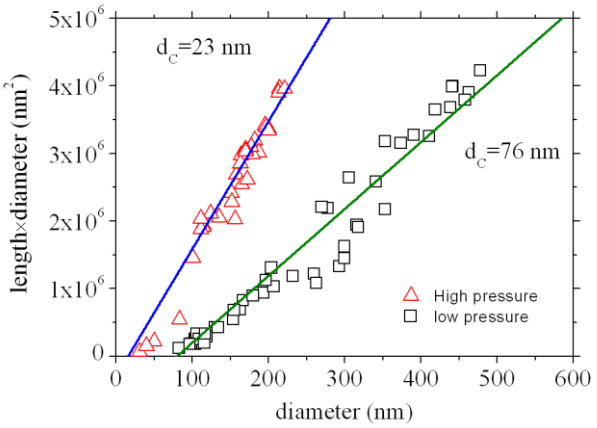

Figure III.7 – The variation of Si NW length multiplied with diameter on function of diameter. The fitting lines are obtained from $Ld=K(d-d_C)t$.

Then, using Equation III.13, we can fit our experimental data as shown in Figure III.8. The best fit is obtained by choosing α to be 8.2×10^{-3} and 1.4×10^{-3} at high and low silane pressure respectively. The Si saturation vapor P_∞ can be calculated to be 7.1×10^{-4} mbar either at high or low silane pressure. This value is much smaller than the one in the literature (10^{-20} mbar) at the temperature of 500 ℃ [12].

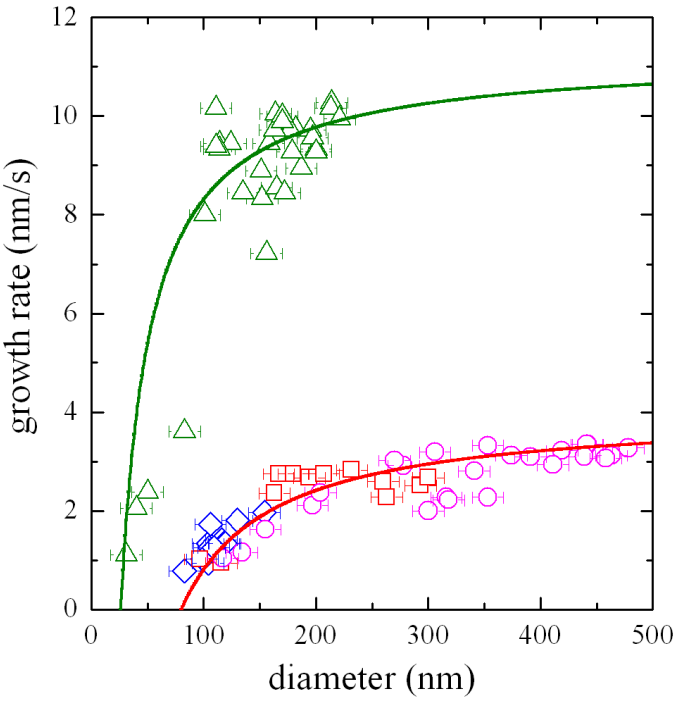

Figure III.8 – Comparison of growth rates of Si nanowires as a function of base diameter for different CVD conditions: same growth temperature but different silane partial pressures. The triangles (△) correspond to a silane partial pressure of 0.4 mbar, whereas the squares (□), diamonds (◇) and circle (○) correspond to a silane partial pressure of 0.08 mbar. The Au droplets for triangle, square and diamond conditions are obtained by UHV Au deposition. The density of Au droplets for the triangle and diamond conditions is higher than for the square condition. The Au droplet for the circle condition is obtained by annealing a Au thin film. The green and red curves correspond to the pressure-based model proposed in this work (Equation III.16).

Comparison of the droplet densities on the growth rate shows that the density does not affect the growth rate. Indeed, the fitted curve for Si NWs grown at low silane partial pressure overlaps whatever the density of Au droplet at the Si surface prior to the growth of Si NWs. Because a different droplet density means a different average distance between the Si NWs, such a result is consistent with our assumption to neglect $J_{diffusion}$ that would correspond to Si adatoms diffusing from the substrate. Therefore, our model where only the incorporation of Si atoms at the droplet surface is taken into account is valid.

As a conclusion, our result indicates that the growth rate and hence the NW length always increase with the NW diameter. In order to obtain a uniform NW length distribution, it is thus necessary to control the catalyst size with great care.

III.2.2 Molecular Beam Epitaxy (MBE)

A brief comparison needs to be made between the CVD and MBE synthesis methods before considering the results as for the MBE-grown NW. Two differences can be pointed out. The first important difference between the CVD and MBE growth modes is the NW species atom source. In CVD, the NW species atoms are provided by molecular precursors such as silane and therefore their decomposition is necessary. In MBE, Si atoms are directly produced by the evaporation of the bulk of Si material where the beam of Si atoms in the gas phase has a given orientation with respect to the substrate. In addition, there are three different areas which are exposed effectively to the Si atoms, namely, the Au-rich droplet surface, the NW sidewall surface, when the flux is not parallel to the sidewall, and the substrate. Thus, in the model of MBE-grown NWs, two different types of NWs are presented and discussed in detail, namely, vertical NWs (the flux direction and the NW growth direction are parallel) and inclined NWs (there is an angle between the flux direction and the NW growth direction).

Then, the growth pressure between CVD and MBE system is quite different. In CVD, the growth pressure is kept around 0.1 mbar or even higher. However, in MBE system, the pressure is very low in the range 10^{-9} mbar. It has been shown in the literature that the growth pressure can greatly influence the diffusion or migration of surface atoms [13]. Therefore, the diffusion of atoms can easily occur in MBE. Thus, it is necessary to consider the quantity $J_{diffusion}$ in the growth rate model.

III.2.2.1 Vertical nanowires

The first type of MBE-grown NWs to be considered is NWs with growth direction parallel to the flux direction. As an example, we will focus on the growth of [111]-oriented Si NWs, that are perpendicular to the Si(111) surface and are grown from a flux of Si atoms normal to the surface. In the following paragraph, these Si NWs are referred as the vertical NWs for simplicity. The Si NWs were grown by the MBE method and the Au catalyst droplets were formed on the Si substrate at a temperature of 360 ℃. The chamber pressure was kept at a very low pressure of 10^{-9} mbar during Si NW growth. The Si atoms were evaporated onto the Si substrate at 550 ℃ and the evaporation rate was 0.05 nm/s. The growth time was 60 min. A SEM image of these MBE-grown Si NWs is shown in Figure III.9. It can be seen from Figure III.9 that almost all of the Si NWs grew vertically on the Si (111) substrate.

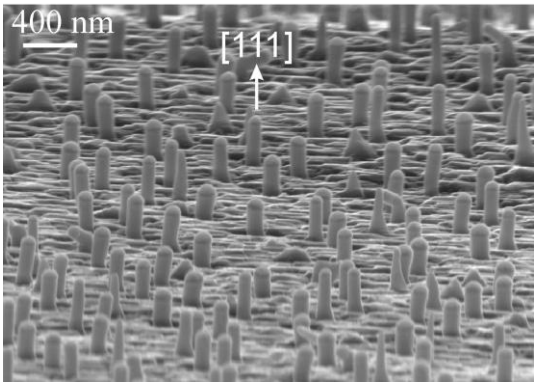

Figure III.9 – Scanning electron microscopy image of vertical Si NWs grown on a Si (111) substrate using MBE. The Au droplets are seen on the top of the Si NWs.

The schematic of the different incorporation pathways is illustrated in Figure III.10. There is a spontaneous deposition of a Si layer on the Si substrate, the thickness of this layer being proportional to the deposition flux rate. The investigation of the growth rate for these Si NWs as a function of diameter is reported in Figure III.11. It can be seen that the growth rate of the Si NWs synthesized by MBE decreases with the NW diameter. This trend has also been found for other semiconductor NWs elaborated by the MBE method such as GaP NWs [14] and GaAs NWs [15]. Here, a diffusion-induced model is proposed.

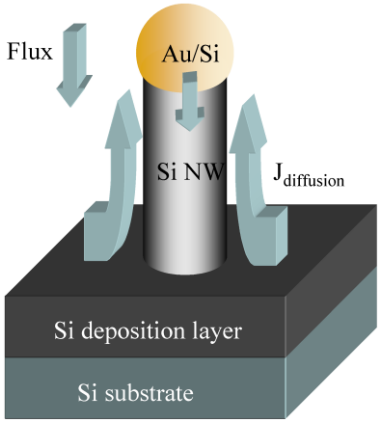

Figure III.10 – Schematic illustration of the atomic pathway involved in the growth during MBE. $J_{diffusion}$ yields for the flow of adatoms along the sidewalls towards the Au droplet.

As the growth direction of the Si NWs is parallel to the flux direction (the vertical NWs), no Si atom impinge directly onto the Si NW sidewall. These Si atoms are deposited only on the surface of the droplets and the substrate and the deposition flux is the same on the droplets and the substrate. However, the atom collecting surface on the substrate is much larger than the droplet surface. Therefore, the impingement flux on the droplet surface in Equation III.5 can be neglected. This leads to the following expression:

$$\frac{\pi d^2}{4\Omega}\frac{dL}{dt} = \pi d j_{diffusion} \qquad \text{(Equation III.15)}$$

The diffusion flux can be written as a Nernst-Einstein's diffusion flux expression [16]:

$$j_{diffusion} = -\frac{nD}{k_B T}\frac{\partial \mu}{\partial L} \qquad \text{(Equation III.16)}$$

Thus, the growth rate expression can be written as the following equation:

$$\frac{dL}{dt} = \frac{4\Omega}{d} \times \frac{nD}{k_B T} \times \frac{\Delta\mu_{Si}^{adatom-L}}{\lambda_{NW}} \qquad \text{(Equation III.17)}$$

In the equation above, the right term corresponds to the diffusion of Si adatoms from the sidewall of the Si NW towards TPB. $\Delta\mu_{Si}^{adatom-L}$ is the chemical potential difference between the adatoms at the Si NWs surface and TPB. n is the Si adatom density on the NW sidewall and it is chosen as its maximum value here, namely, one monolayer. D and λ_{NW} are the diffusion coefficient and the effective diffusion length of Si adatoms on the NW sidewall. The values of D and λ_{NW} can be estimated to be about 10^{-10} cm^2/s and 1 μm respectively and $\Delta\mu_{Si}^{adatom-L}$ = 1 following the literature [17, 18]. The experimental data and the fit curve are presented in Figure III.11 (a). As shown in Figure III.11 (a) the growth rate of the Si NWs decreases with the increase of diameter and a good agreement is observed between the experimental data and the curve. The experimental data of Si NWs from the literature [19] is also reported in Figure III.11 (b) using Equation III.17. The values of D and λ_{NW} are chosen to be 4.1×10^{-11} cm^2/s and 0.9 μm respectively because of the lower temperature 525 ℃ compared to the growth temperature in this work (550 ℃). In both experimental conditions the deposition flux has the same value of 0.05 nm/s. $\Delta\mu_{Si}^{adatom-L}$ is chosen to be 1.03 because it slightly change with the growth temperature.

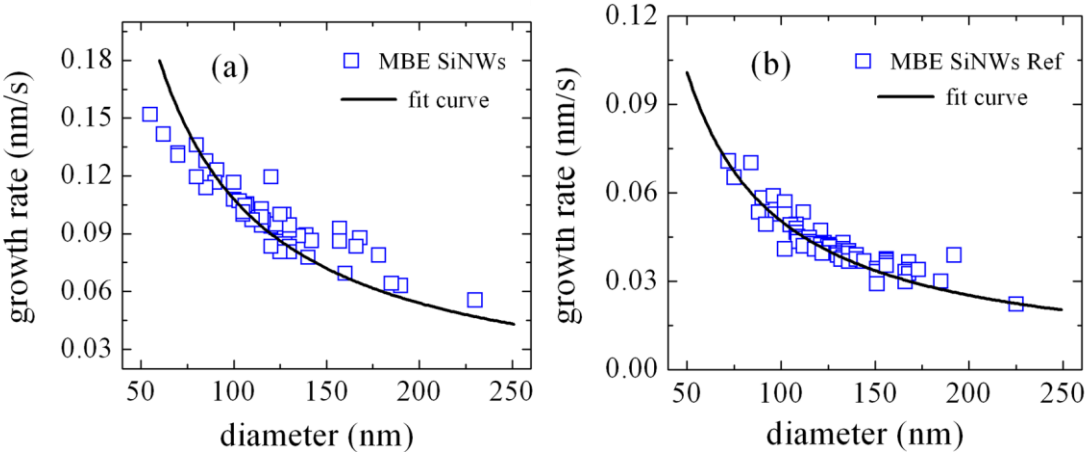

Figure III.11 – Evolution of Si NW growth using MBE synthesis method. The black fit curve is obtained using the model presented in this work. (a) Si NWs are fabricated by MBE at 550 ℃

for 60 min. (b) Si NWs are elaborated by MBE at 525 ℃ for 240 min, the experimental data are collected from [19].

III.2.2.2 Inclined nanowires

It has been shown that Ge NWs can grow with <110>-orientations on the Si (111) substrate due to a lower nucleation energy along this direction [20]. In our case, Ge NWs were grown by MBE on a Si (111) substrate using Au as the catalyst droplets. The chamber pressure was kept at a very low pressure of 10^{-9} mbar. The Ge atoms were deposited at a substrate temperature of 350 ℃ which is slightly lower than the eutectic Ge/Au alloy temperature of 361 ℃. It has been show recently in the literature that Ge NWs can indeed grow under the alloy eutectic temperature and the catalyst droplet can still remain liquid even though the temperature is 100 ℃ below the eutectic temperature [21]. The Ge atom evaporation rate was kept at 0.17 nm/s. The dependence between the NW growth length and the diameter was investigated like in the previous cases. However, in this part, the NW growth time was also chosen as a variable experimental parameter in order to study their morphological evolution with time.

Concerning the NW growth direction, two types of Ge NWs are found as indicated in the SEM image of Figure III.12 (a), namely, the vertical [111] and the inclined <110>-oriented Ge NWs. The inclined Ge NWs are much longer than the vertical [111]-oriented Ge NWs. The reason will be discussed afterwards. Figure III.12 (b) is a cross-section view of a single inclined <110>-oriented Ge NW which surpasses the spontaneous deposited Ge layer with a thickness H. The catalyst droplet of Au is seen on the top end of the Ge NW.

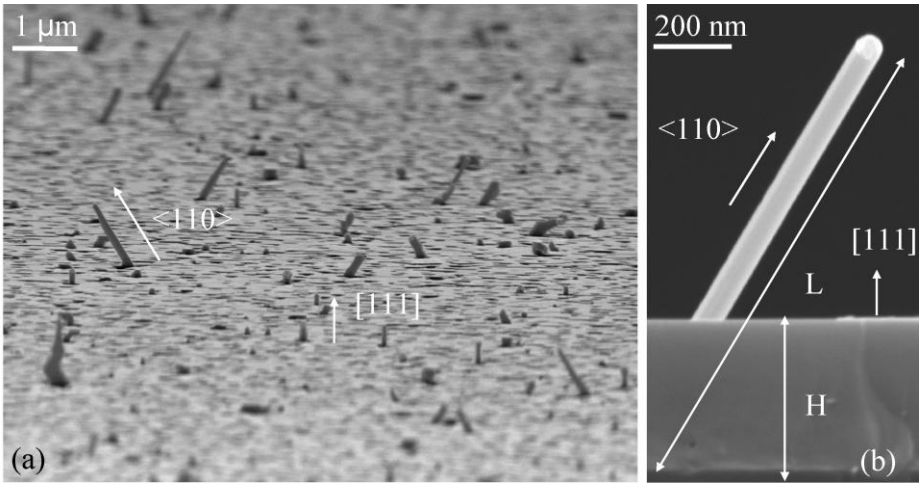

Figure III.12 – Scanning electron microscopy images of Ge NWs grown on a Si (111) substrate using MBE synthesis method. (a) Overall view of inclined and vertical Ge NWs with

a 10 ° tilt normal to Si substrate. The length of the inclined Ge NWs protruding over the overgrown layer is much larger than the length of the vertical Ge NWs. (b) Cross-section view of a single inclined Ge NW. H is the height of the Ge overgrown layer. L is the total length of the NW including the overgrown part.

Here we focus on the inclined NWs, since the vertical ones have been studied before and the orientation flux has not changed. During the evaporation of Ge atoms, they impinge on the substrate as well as on the NW sidewalls, because the flux is normal to substrate. As a result, two different diffusion terms have to be considered. The schematic illustration of the incorporation pathways is presented in Figure III.13.

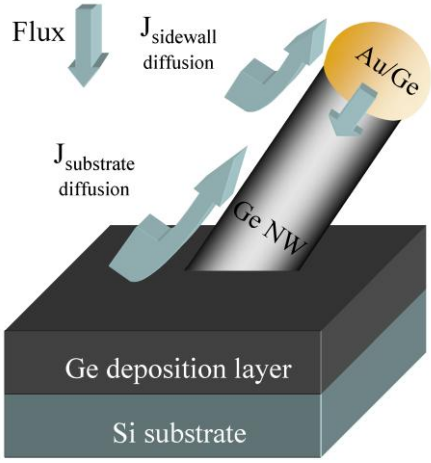

Figure III.13 – Schematic illustration of possible pathways for the MBE growth of an inclined Ge NW. $J_{diffusion}$ yields for the flow of adatoms along the sidewalls towards the Au droplet. There is an overgrown Ge layer on the Si substrate and its thickness is proportional to the deposition flux.

The time evolution of diameter-length dependence of inclined Ge NWs is plotted in Figure III.14. The data are collected from for three growth time (15 min, 30 min and 60 min) keeping the other growth parameters constant (catalyst droplet, Ge flux and temperature). Figure III.14 reveals that three diameter-length dependences are exhibited during NW growth. At short growth time (15 min), as shown with green circle in Figure III.14, the length of Ge NWs has the typical inversed dependence on their diameter just as the example found with the vertical MBE-grown Si NW (Figure III.11). However, in this case, the length of inclined NWs is much longer than the vertical NWs for the same NW diameters. We attribute this difference to the incorporation of the sidewall impingement. As the growth time becomes longer (30 min), the dependence of the length-diameter is found to be flat, as illustrated with the blue triangle in Figure III.14. At a growth time of 60 min, the dependence of the length-diameter

exhibits a behavior similar to the typical CVD-grown NWs (the red square in Figure III.14): the larger the diameter, the longer the NWs.

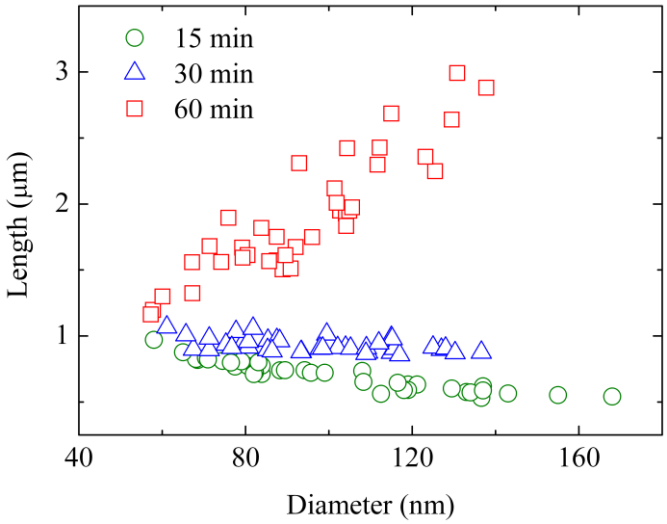

Figure III.14 – Time evolution of the diameter-length dependence of inclined <110>-oriented *Ge NWs. The experimental data are collected from three different growth time: green circle, 15 min; blue triangle, 30 min and red square, 60 min.*

For presenting the evolution of the diameter-length dependence in a more obvious way, the data are re-plotted in Figure III.15. Figure III.15 shows the dependence of the NW length on growth time for seven different diameters. It can be concluded that Ge NWs with smaller diameters can grow faster at the beginning but almost stop growing after a certain time. Whereas, Ge NWs with larger diameter grow faster with time. The growth rate of NWs is given by [22] (see Annex I):

$$\frac{dL}{dH} = A + \frac{BU + C}{dU / dl} \qquad \text{(Equation III.18)}$$

where H=Vt is the deposition thickness of the overgrown layer, t is the NW growth time, $l=L/\lambda_f$ is the normalized NW length and λ_f is the adatom diffusion length on the NW sidewalls. The solution of Eq. III.16 yields [23] (see Annex I):

$$L = 2\Lambda_s \sqrt{\frac{\exp(2ag_f H / R) - 1}{2ag_f}} \qquad \text{(Equation III.19)}$$

where $\Lambda_s = \lambda_s \sqrt{g_s / b}$ is the effective diffusion length on the substrate surface. a=[ω $sin(\alpha+\varphi)/cos\alpha$] is the geometrical factor for the MBE growth with the tilt angle φ to the substrate normal and the beam incident angle α without substrate rotation. $b=(D_s\sigma_f/D_f\sigma_s)$ with D_f, D_s, σ_f and σ_s are the adatom diffusion coefficients and the elementary areas of the sidewall and the substrate. The functions $g_f=1-\theta_l/\theta_f$ and $g_s=1-\theta_l/\theta_s$ describe the influence of (liquid)

droplet chemical potential ("*l*") on the diffusion of sidewall ("*f*") and surface ("*s*") adatoms. The quantity $\theta_l=exp(\mu_l/k_BT)$ is the activity of semiconductor atoms in the droplet, with μ_l as the corresponding chemical potential, k_B as the Boltzmann constant and T as the substrate temperature. The quantities $\theta_f=exp(\mu_f/k_BT)$ and $\theta_s=exp(\mu_s/k_BT)$ are the effective activities with μ_f and μ_s as the corresponding chemical potentials. The Equation III.19 can be reduced to the square root growth law $L=2\Lambda_s\sqrt{H/R}$ at small H regardless of g_f. At large H, it gives either the exponential increase of NW length with H at $g_f>0$, or the limited growth to a finite length at $g_f<0$. The Equation III.19 above provides qualitative description of infinite and limited NW growth modes at a constant diffusion length. However, we were not able to fit the experimental data with an R-independent Λ_s.

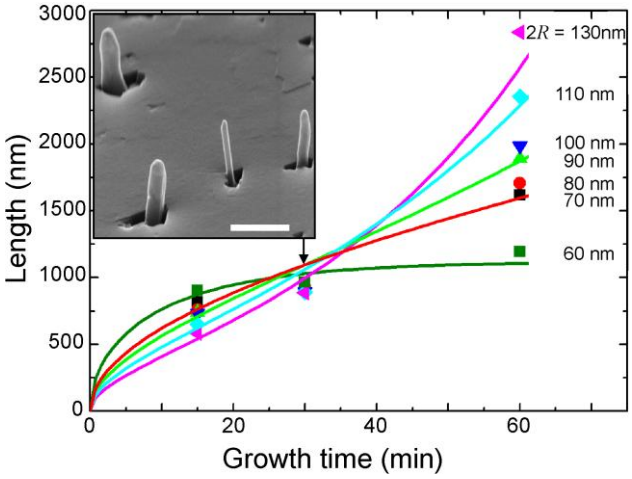

Figure III.15 – Dependence of NW length on growth time for <110>-oriented Ge NWs for seven different diameters (symbols), and theoretical fits (lines) obtained from Equation III. 19. Ge NWs with smaller diameter grow faster compared to the one with larger diameter at the beginning, whereas, the growth velocity is inversed when the time increases. Inset: SEM image of <110>-oriented Ge NWs grown for a time of 30 min. The scale bar is 600 nm.

As shown in Figure III.15, a crossing point exists and can be explained by the different directions and magnitudes of diffusion flux on the NW sidewall. It occurs, at a growth time of 30 min as shown by the black arrow in Figure III.15. For this growth time, the Ge NW length extending the overgrown Ge layer is around 600 nm whatever the NW diameter is. The color curves in Figure III.15 are the fitting curves using Equation III.19. The fitting parameters are listed in Table III.2. The magnitude and the direction of the corresponding diffusion flux are controlled by the ratio of θ_l/θ_f in Equation III.19. θ_f/θ_l increases from 0.70 (corresponding to a

negative diffusion flux) for 60 nm diameter NWs to ∞ (corresponding to a positive diffusion flux at negligible liquid activity) for 130 nm diameter NW.

d (nm)	Λ_s (nm)	g_f	θ_f/θ_l	$\Delta\mu_{fl}$ (meV)
60	220	-0.43	0.70	-20
80	193	0.04	1.04	2.2
90	181	0.26	1.35	16
110	158	0.63	2.70	54
130	140	1	∞	∞

Table III.2 – Fitting parameters <110>-oriented Ge NWs as a function of their diameter.

Since the diffusion of adatoms occurs along the NW sidewalls, we can wonder if any adatoms incorporate to the sidewalls when the length of the NWs is larger than the diffusion length. This would give rise to NW morphologies that deviate from a cylindrical shape. Thus, we study variations of the NW diameter between the base and the top of NWs in the next part of this chapter.

III.3 Growth condition effect on tapering

The diameter of ideal Si NWs is constant after NW growth begins and should correspond to the initial diameter of the catalyst droplet (Figure III.16 (a) and (b)). Considering the general shape of a single NW, two shapes are likely to exist, namely, a cylindrical one (Figure III.16 (b)) and a tapered one (Figure III.16 (c) and (d)). Here, tapering is defined as the decrease of NW top diameter or the increase of NW base diameter during the NW growth. As the ideal growth shape of a Si NW is a cylinder, it is reasonable to think about two possibilities to account for a deviation from this shape. The first type of NW tapering (Figure III.16 (c)) is the result of the reduction of the catalyst (Au) droplet volume which is induced by the migration Au atoms during the NW growth [24-29]. This effect can be inhibited by increasing the growth pressure (silane partial pressure [26] or total pressure [27]) or adding impurity precursors such as oxygen in the gas phase [30]. The second type of NW tapering (Figure III.16 (d)) is the result of radial deposition onto the NW sidewalls. Radial deposition on the sidewalls can be explained in two ways: the direct deposition from the precursor via VS mechanism and the diffusion of adatoms on the NW sidewall from the substrate. This phenomenon has been found for intrinsic Si NWs [31-33]. It is greatly enhanced when dopants are incorporated during the growth of the NW [34, 35]. This type of tapering can be inhibited by decreasing the growth temperature [36, 37]. Normally, both types of tapering occur simultaneously. In this work, we will study how the droplet density and a

gas pressure change affect the shape of the NWs.

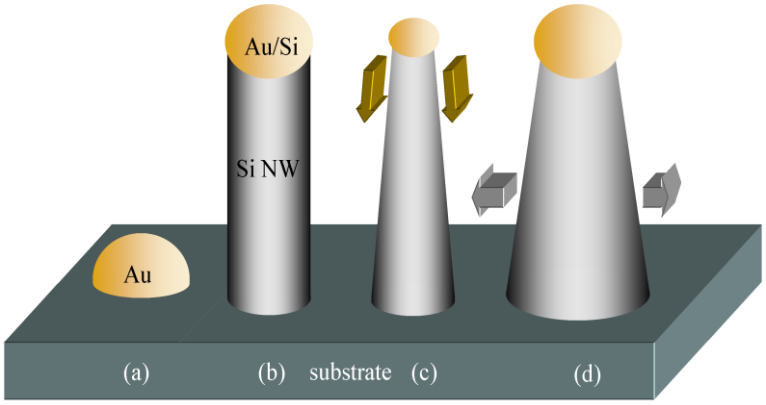

Figure III.16 – Schematic evolution of the diameter of Si NWs synthesized via VLS mechanism. (a) A catalyst droplet (Au) on a substrate (Si). (b) An ideal Si NW with a uniform diameter along NW growth direction. (c) The tapering results from the migration of Au atoms during NW growth, shrinking the size of the Au droplet. Arrows represent the direction of the Au atom migration. (d) The tapering is the result of a radial NW sidewall deposition. Arrows represent the lateral NW growth.

III.3.1 Catalyst droplet density

In order to study how the Au droplet density affects the shape of the NWs, Si NWs were grown with two different Au droplet densities under the same low silane partial pressure (0.08 mbar), the same total pressure (1.1 mbar), the same temperatures (500 ℃) and the same growth time (30 min) using CVD. The results are reported in Figure III.17. A linear relation is found between the diameter of the droplet at the top of NWs (d_{top}) and the diameter of their base (d_{base}). Although the growth conditions are the same, the tapering effect is more pronounced in the case of the low droplet density, when NWs with a similar base diameter are considered. The reason will be discussed afterwards.

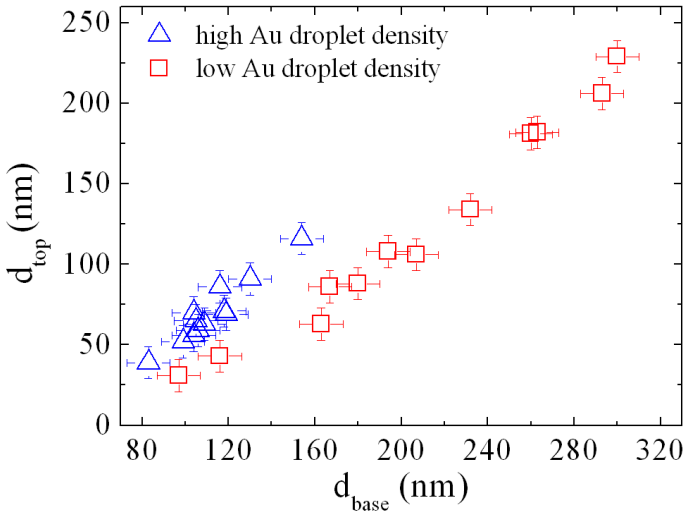

Figure III.17 – Measurements of the Si NW top diameters (d_{top}) as a function of their base diameters (d_{base}). Measurements from the high and low density droplets are plotted in blue triangles and red squares respectively. Si NWs are synthesized at the same temperature of 500 °C, the same growth time (30 min), the same silane partial pressure (0.08 mbar) and the same total pressure (1.1 mbar)

III.3.2 Growth precursor pressure

Si NWs were synthesized by CVD under two different silane partial pressures but with the same total pressure (1.1 mbar), the same catalyst droplet densities (high), the same temperatures (500 °C) and the same growth time (30 min). Here, the average tapering quantity is defined as $((d_{base} - d_{top}) / L = \Delta d/L$ which corresponds to the decrease of the diameter along the main axis of the NW. As the ratio between Δd and L is small, it corresponds to the angle between the main axis of the NW and the segment defined by the NW sidewall. The top and base diameters of the Si NWs and their length are measured with SEM. The results are reported in Figure III.18. In order to account for these results, two growth rates have to be considered. The first one is the axial growth rate which is the main growth rate and is related to the NW diameter and the precursor pressure. The second one is the lateral growth. At low silane partial pressure, it clearly appears that the tapering varies as the inversed of the length of the NW. Indeed, the rate of the lateral growth can be considered to be constant for a given specimen during the growth. Due to the formation of facets, the dissociation of the silane precursor on the NW sidewall does not lead to a significant diffusion of the Si atoms towards the Au-rich droplet, but rather to their direct incorporation onto the sidewall, causing a lateral overgrowth. If it is assumed that all the Si NWs start to grow at the same time, the overgrowth

will be the same whatever the initial NW diameter at a given length from the NW base. Since the thickness of the Si layer overgrown on the Si sidewall along the main axis of the NW depends only on the duration of the growth and NWs with the bigger diameters have the higher growth rate, the tapering angle will decrease as 1/L as the total diameter increases. In contrast, at high silane partial pressure, the ratio between Δd and L is quite small and does not significantly vary when the total diameter of NW increases.

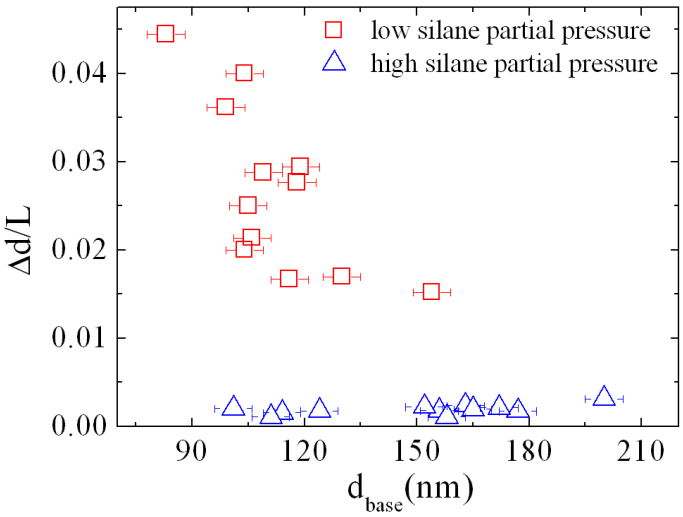

Figure III.18 – Degree of tapering, defined as Δd/L = (d_{base} – d_{top}) / L, as a function of the NW diameter for two different silane partial pressures. d_{base}, d_{top} and L are the base, the top diameters and the length of Si NWs respectively. Calculations from the high (0.4 mbar) and low (0.08 mbar) silane partial pressure are plotted in blue triangles and red squares respectively. Si NWs are synthesized at the same temperature of 500 ℃, the same growth time (30 min) and the same total pressure (1.1 mbar)

As mentioned previously, two reasons are at the origin of the tapering effect: the reduction of the droplet volume and the lateral growth of NW. The first part of the discussion focuses on the reduction of the catalyst droplet volume. There are two reasons that can contribute to the reduction of the catalyst droplet volume as mentioned earlier, namely, the migration of Au atoms through TPB towards the volume of the NW and the diffusion of Au atom through the interface between the droplet and the NW. It has been shown in the literature that the migration of Au atoms from the droplet towards the NW sidewall surface is the major mechanism for tapering during growth for low pressure conditions [24]. In order to estimate the number of Au atoms that leave the droplet, the Au droplet is assumed to be a hemisphere, the contact angle of the droplet being 90 °. It is also supposed that the droplet is

of pure Au at the beginning of the growth and that the Au concentration at the end of the growth may be given by the Au/Si phase diagram [38].

Although the initial diameter of the Au-rich droplet is not known, it is assumed that the base diameter does not change during the growth in case there is no lateral overgrowth. As a result, the reduction of the droplet size can be measured from the difference between the base diameters compared to the top diameter. One then needs to estimate the thickness of the Au atom coverage on the NW sidewall. Several thickness estimation values are given in the literature such as 1 monolayer [24] and 1.8 monolayer [28]. The later one was deduced by taking into account the existence of Au clusters on the NW sidewalls. In our work, the thickness of the Au coverage on the sidewalls is chosen as 1 monolayer. As this wetting layer is supplied by the Au-rich droplet at the top of the NWs, it is related to the decrease the droplet volume. Figure III.19 shows the comparison between both quantities: the increase of the Au coverage and the reduction of the droplet size. The plotted data corresponds to the average values obtained for 12 different NWs and three different growth conditions.

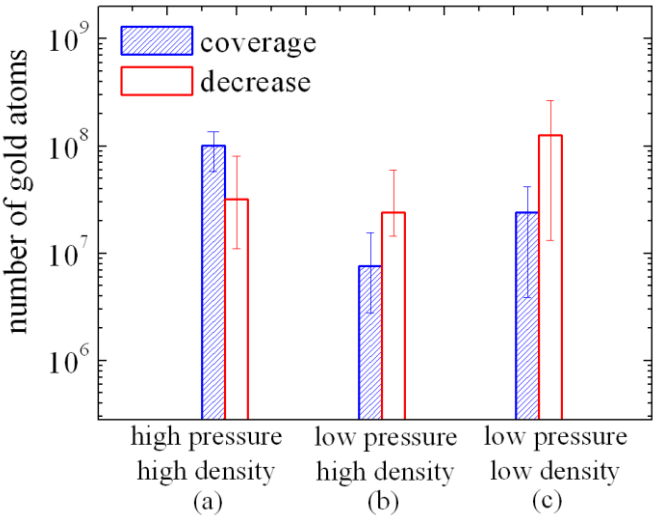

Figure III.19 – Average Au atom variation in droplets compared to average Au atoms needed to wet the NW sidewall surface with one monolayer for three different growth conditions. Blue shadow and red hollow bars represent the Au atom coverage on the Si NW sidewall surface and the reduction of Au atoms in the droplet during the Si NW growth respectively for all three growth conditions. Error bars represent the deviation obtained from 12 samples.

As illustrated in Figure III.19 (a), it is clearly shown in the case of the high silane partial pressure, that the lost of Au atoms in the droplets is not sufficient to cover the entire sidewall surface. The reverse situation is observed when the silane partial pressure is low and whatever the densities of the droplets are (Figure III.19 (b) and (c)). It can be assumed in

these later two cases that the migration of Au atoms occurs on the NW sidewall, the sidewalls growing laterally at the same time. Owing to these considerations, the results presented in Figure III.17 and Figure III.18 can be discussed as follows:

At low silane partial pressure, the lateral growth contribution to the tapering of the NWs can be assumed to be identical due to the same experimental conditions (same total pressure, same silane partial pressure and same temperature) for high and low densities of Au droplets. However, Figure III.17 shows that the NWs prepared with the lower density of droplet are more tapered. Therefore, this variation in the tapering effect is only caused by the migration of Au atoms on the NW sidewalls. It must be noted here that the total number of Au atoms deposited on the Si substrates, prior to Si NW growth, has the same value because Au deposition flux and time are the same for both samples. The Gibbs-Wulff theory indicates that the gradient of chemical potential is the driving force for diffusion on surface [18]. In this case, the migration coefficient of Au atoms on all NW surfaces has the same value because the pressure and the temperature are identical for both samples. The Au atoms flux on the NW sidewall surface, j, is given by the relation of Nernst-Einstein:

$$j = -\frac{nD}{k_B T}\frac{\partial \mu}{\partial L} \qquad \text{(Equation III.20)}$$

As the Au atom density on the substrate surface is small, the Au atoms can migrate from the droplets towards the regions of the substrate located between the NWs. Because these regions are bigger in the case of a sample with a low density of droplets, they can accommodate more Au adatoms migrating from the droplets during the growth. These droplets thus lose more Au atoms, causing the formation of NWs that are more tapered.

III.4 Conclusion

As a conclusion, in this chapter we have investigated key parameters that govern the NW morphology: their length and their diameter. Considering the NW length, two growth methods (CVD and MBE) have been used to synthesize NWs. Several growth rate models have been developed by taking into account the different incorporation pathways. For CVD-grown Si NWs, the dominant incorporation pathway is the impingement through the catalyst droplet surface. For MBE-grown NWs, two different growth directions (vertical and inclined) have been characterized in order to investigate the NW sidewall diffusion effect on NW growth rate. It is found that the growth rate of NWs with inclined growth direction is larger than the vertical one due to the impingement flux on the NW sidewalls. Normally, the growth rate of MBE-grown NWs decreases with their diameter. For the inclined NWs, the time

evolution of length-diameter dependence indicates that there is a cross point of the diameter-length dependence at a certain time, which can be used to narrow the NW length distribution regardless of the initial catalyst droplet size.

Concerning the change of Si NW diameter (tapering) during Si NW growth, we have found that two different growth parameters, namely, the growth precursor pressure and the catalyst droplet density, can influence the tapering simultaneously. The tapering of Si NWs synthesized at high precursor pressure and droplet density is weaker than the one grown at low precursor pressure and droplet density.

Bibliography of chapter III

[1] R. S. Wagner, and W. C. Ellis, Appl. Phys. Lett., 4, 89 (1964)
[2] H. J. Levinson, Principles of Lithography, SPIE Press (2005)
[3] E. I. Givargizov, J. Cryst. Growth, 31, 20 (1975)
[4] V. Schmidt, J. V. Wittemann, and U. Gosele, Chem. Rev., 110, 361 (2010)
[5] T. Xu, J. P. Nys, A. Addad, O. I. Lebedev, A. Urbieta, B. Salhi, M. Berthe, B. Grandidier, and D. Sti évenard, Phys. Rev. B, 81, 115403 (2010)
[6] D. H. K. Murthy, T. Xu, W. H. Chen, A. J. Houtepen, T. J. Savenije, L. D. A. Siebbeles, J. P. Nys, C. Krzeminski, B. Grandidier, D. Stievenard, P. Pareige, F. Jomard, G. Patriarche, and O. I. Lebedev, Nanotechnology, 22, 315710 (2011)
[7] N. Li, T. Y. Tan, and U. G ösele, Appl. Phys. A, 86, 433 (2007)
[8] H. Zhao, S. Zhou, Z. Hasanali, and D. Wang, J. Phys. Chem. C, 112, 5695 (2008)
[9] K. K. Lew, and J. M. Redwing, J. Cryst. Growth, 254, 14 (2003)
[10] J. Kikkawa, Y. Ohno, and S. Takeda, Appl. Phys. Lett., 86, 123109 (2005)
[11] F. Dhalluin, P. J. Desre, M. I. den Hertog, J.-L. Rouviere, P. Ferret, P. Gentile, and T. Baron, J. Appl. Phys., 102, 094906 (2007)
[12] S. Davis, J. Chem. Phys., 34, 659 (1961)
[13] U. Gosele, Nature, 440, 34 (2006)
[14] J. Johansson, C. P. T. Svensson, T. Martensson, L. Samuelson, and W. Seifert, J. Phys. Chem. B, 109, 13567 (2005)
[15] V. G. Dubrovskii, N. V. Sibirev, G. E. Cirlin, M. Tchernycheva, J. C. Harmand, and V. M. Ustinov, Phys. Rev. E, 77, 031606 (2008)
[16] M. Z. A. Munshi, Handbook of Solid State Batteries and Capacitors, World Scientific, Singapore (1995)
[17] D. Srivastava, and B. J. Garrison, Phys. Rev. B, 46, 1472 (1992)
[18] A. Pimpinelli, and J. Villain, Physics of Crystal Growth, Cambridge University Press (1998)
[19] L. Schubert, P. Werner, N. D. Zakharov, G. Gerth, F. M. Kolb, L. Long, U. Gosele, and T. Y. Tan, Appl. Phys. Lett., 84, 4968 (2004)
[20] A. Kramer, M. Albrecht, T. Boeck, T. Remmele, P. Schramm, and R. Fornari, Superlattices Microstruct., 46, 277 (2009)
[21] S. Kodambaka, J. Tersoff, M. C. Reuter, and F. M. Ross, Science, 316, 729 (2007)
[22] V. G. Dubrovskii, N. V. Sibirev, G. E. Cirlin, I. P. Soshnikov, W. H. Chen, R. Larde, E. Cadel, P. Pareige, T. Xu, B. Grandidier, J. P. Nys, D. Stievenard, M. Moewe, L. C. Chuang, and C. Chang-Hasnain, Phys. Rev. B, 79, 205316 (2009)
[23] V. G. Dubrovskii, T. Xu, J.-P. Nys, Y. Lambert, B. Grandidier, D. Sti évenard, W. H. Chen, and P. Pareige, Submitted
[24] J. B. Hannon, S. Kodambaka, F. M. Ross, and R. M. Tromp, Nature, 440, 69 (2006)
[25] L. Cao, B. Garipcan, J. S. Atchison, C. Ni, B. Nabet, and J. E. Spanier, Nano Lett., 6, 1852 (2006)
[26] M. I. den Hertog, J.-L. Rouviere, F. Dhalluin, P. J. Desr é, P. Gentile, P. Ferret, F. Oehler, and T. Baron, Nano Lett., 8, 1544 (2008)
[27] T. Kawashima, T. Mizutani, T. Nakagawa, H. Torii, T. Saitoh, K. Komori, and M. Fujii, Nano Lett., 8, 362 (2008)
[28] A. Bailly, O. Renault, N. Barrett, L. F. Zagonel, P. Gentile, N. Pauc, F. Dhalluin, T. Baron, A. Chabli, J. C. Cezar, and N. B. Brookes, Nano Lett., 8, 3709 (2008)
[29] P. Madras, E. Dailey, and J. Drucker, Nano Lett., 10, 1759 (2010)
[30] S. Kodambaka, J. B. Hannon, R. M. Tromp, and F. M. Ross, Nano Lett., 6, 1292 (2006)

[31] P. Aella, S. Ingole, W. T. Petuskey, and S. T. Picraux, Adv. Mater., 19, 2603 (2007)
[32] H. Schmid, M. T. Bjork, J. Knoch, H. Riel, W. Riess, P. Rice, and T. Topuria, J. Appl. Phys., 103, 024304 (2008)
[33] W. H. Chen, R. Larde, E. Cadel, T. Xu, B. Grandidier, J. P. Nys, D. Stievenard, and P. Pareige, J. Appl. Phys., 107, 084902 (2010)
[34] D. E. Perea, E. R. Hemesath, E. J. Schwalbach, J. L. Lensch-Falk, P. W. Voorhees, and L. J. Lauhon, Nat. Nanotechnol., 4, 315 (2009)
[35] G. Imamura, T. Kawashima, M. Fujii, C. Nishimura, T. Saitoh, and S. Hayashi, Nano Lett., 8, 2620 (2008)
[36] P. Xie, Y. Hu, Y. Fang, J. Huang, and C. M. Lieber, Proceedings of the National Academy of Sciences, 106, 15254 (2009)
[37] E. Koren, N. Berkovitch, and Y. Rosenwaks, Nano Lett., 10, 1163 (2010)
[38] H. Baker, and H. Okamoto, ASM Handbook: Volume 3: Alloy Phase Diagrams, ASM International, 2·76 (1992)

Chapter IV

IV Influence of the catalyst materials on the growth of out of plane and in-plane Si nanowires (VLS and SLS)

It is well known that impurities in a crystal modify the perfect crystal's chemical bonds and govern many important properties of materials, such as their conductivity, color and chemical reactivity [1, 2]. As seen in the previous chapter, the growth of Si nanowires (NWs) occurs through the use of catalysts droplet and it has been shown that the catalyst droplet might shrink in size during the growth, due to the diffusion of catalyst materials. Such diffusion occurs mainly on the NW sidewalls, but catalyst materials can also be incorporated into the volume of the NWs [3]. They act as impurities that affect the overall electrical properties of the NWs. As an example, Figure IV.1 compares the magnitude and lifetimes of photoconductance traces measured on Si NWs using the Time-Resolved Microwave Conductivity (TRMC) technique. This technique allows the detection of radiation-induced charge separation by time-resolved measurement of the changes in microwave adsorption [4]. In the case of an array of Si NWs grown from Au catalysts at high silane partial pressure (HP), the lifetime of the photo carriers is of the order of a few ns, whereas for the array grown at low silane partial pressure (LP), where Au is known to wet the NW sidewalls, the lifetime was found to reach µs. Understanding the role of the catalysts not only to increase the crystallization rate, but also to modify the electrical properties of Si NWs is crucial to build functional NWs.

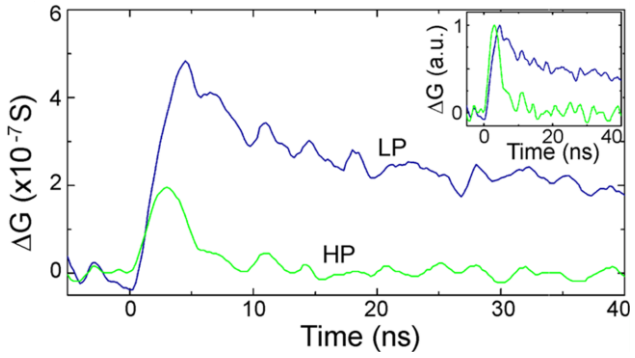

Figure IV.1 – Photoconductance transients observed for non-doped Si nanowires, which are synthesized at high silane pressure (HP) and low silane pressures (LP) respectively, photoexcited at 500 nm using an incident intensity of 6×10^{-7} J/cm^2/pulse. The inset is the normalized photoconductance transients for HP and LP Si NWs. Adapted from [5].

Here we will address several issues. Can we replace Au by other materials to grow Si NWs? Do all catalyst materials that we are going to study diffuse into the volume of the NWs? What are their distributions? Could we expect to turn their bulk incorporation into an asset for the electrical conductivity of the wires?

IV.1 Au distribution in Si nanowires

As Atom Probe Tomography (APT) is a high spatial resolution microscope with a lateral and depth resolution of 0.3 nm and 0.1 nm respectively, it is first possible to evidence whether Si NW is crystalline with the APT technique. Several experimental conditions such as precursor pressure and catalyst droplet diameter can influence the CVD-grown Si NW growth direction simultaneously. It was shown in the literature, that the dominant growth direction of Si NWs with large diameter (> 20 nm) is the [111] direction at low precursor pressure [6-8]. By taking advantage of this diameter-dependent growth orientation, Si NWs were grown intentionally on Si (111) pillars with large diameter catalyst droplets (50 nm < D < 80 nm) using the CVD synthesis method. As a consequence, Si NWs grow perpendicularly on the Si (111) pillars. A single Si NW on a pillar is prepared for the APT investigation by applying the specimen preparation method described in chapter II.2.4.1. The diameter and length of the Si NW analyzed in this work are 70 nm and 5 μm respectively. Figure IV.2 (a) is the cross-section view of 3D reconstruction of a single intrinsic Si NW investigated by laser assisted APT. The presence of three low atom density areas is consistent with the presence of three crystallographic poles. Figure IV.2 (b) is a cross-section of atom map reconstruction showing the [1-10], [2-11] and [101] crystallographic orientations with the measurement distances of 0.37 ± 0.01 nm, 0.32 ± 0.01 nm and 0.38 ± 0.01 nm respectively. The orientations are displayed in 1D in order to measure the inter plane distance accurately. Each crystallographic orientation is calculated from the NW growth direction and the angle between each orientation using the stereographic projection. The distance between the atomic plans can be used to accurately calibrate the 3D lattice reconstruction. The existence of atomic plane in the reconstruction volume reveals that Si NWs has a crystalline structure and attest that the growth takes place along the <111> orientation.

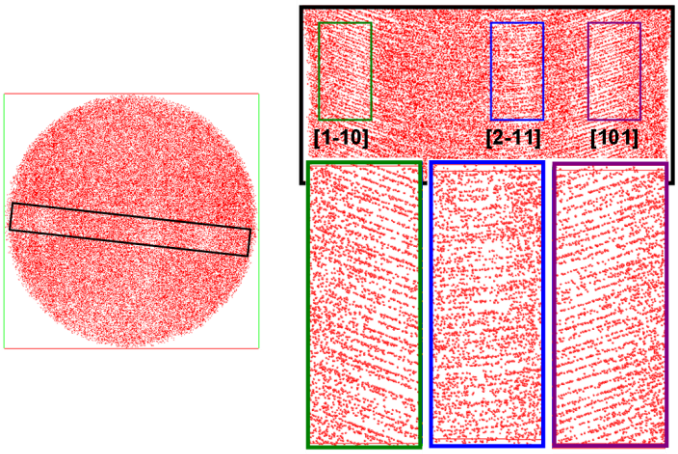

Figure IV.2 – (a) Top view of 3D reconstruction of Si atom distribution in an intrinsic [111] Si NW analyzed by atom probe tomography. The reconstruction surface is 32×32 nm^2. (b) Cross-section view of the 3D reconstruction encompassing the [1-10], [2-11] and [101] crystallographic directions.

Then, information on the chemical composition of the NWs can be obtained. As it was shown in the previous chapter, changing the pressure of silane modifies the volume of the catalyst droplet and the shape of the NWs during the growth. We have therefore studied the distribution of Au atoms in the Si NWs depending on the silane partial pressure.

IV.1.1 Low precursor pressure

The growth experimental condition for achieving the low precursor pressure is listed in Table IV.1. Silane is diluted with hydrogen in a ratio of 1:150. The total and silane partial pressures are kept at 1.1 mbar and 7.3×10^{-3} mbar respectively. The growth temperature and time are 500 ℃ and 30 min respectively.

Pressure (mbar)	T (℃)	SiH_4 (sccm)	H_2 (sccm)	Time (min)
1.1	500	1	150	30

Table IV.1 – Growth experimental condition of intrinsic Si NWs synthesized with low silane pressure. Silane is chosen as the precursor gas. Hydrogen is used as the carrier gas.

In order to study the core as well as the sidewall of the Si NW, a single Si NW was welded inclined on a W tip intentionally as discussed in chapter II.2.3.2. Figure IV.3 (a) shows the SEM image of an individual Si NW with the Au droplet on its top and small Au

clusters on its sidewall. Figure IV.3 (b) is a two-dimensional projection of the chemical analysis performed for this inclined Si NW. While the NW diameter was 65 nm, only one portion of the Si NW extending over 30 nm (reconstructed with inter plane distance) is characterized by APT. The diameter of the analyzed volume for a NW with a certain diameter is 0.56 R, as calculated in chapter II.2.3.2. Therefore, the maximum diameter of the analyzed volume given by APT for a Si NW with a diameter of 65 nm is 36.4 nm which is close to the diameter of the reconstructed volume (30 nm).

Figure IV.3 (c) and (d) show the mass to charge spectra of Au atoms on the Si NW sidewall surface and in the NW core respectively. A peak of Au atoms for Au^+ (197 amu) on the NW sidewall is clearly detected but no peak of Au^+ is detected inside the NW. The upper bound of the total Au atom concentration in the Si NW core is measured to be 3×10^{17} Au/cm^3. The yellow dots in the Si NW core are not the Au atom but just the background noise atoms due to the noise in mass spectrum at 197 amu. A significant incorporation of Au atoms into the core of the Si NWs during the growth is unexpected because of the low equilibrium solubility of Au in Si (e.g. 2×10^{15} Au/cm^3 in Si at 650 ℃ [9]). Although it has been shown that Au atoms can diffuse from the droplet, Figure IV.3 clearly shows that Au atoms prefer to stay adsorbed on the Si NW sidewall rather than to be embedded in the NW.

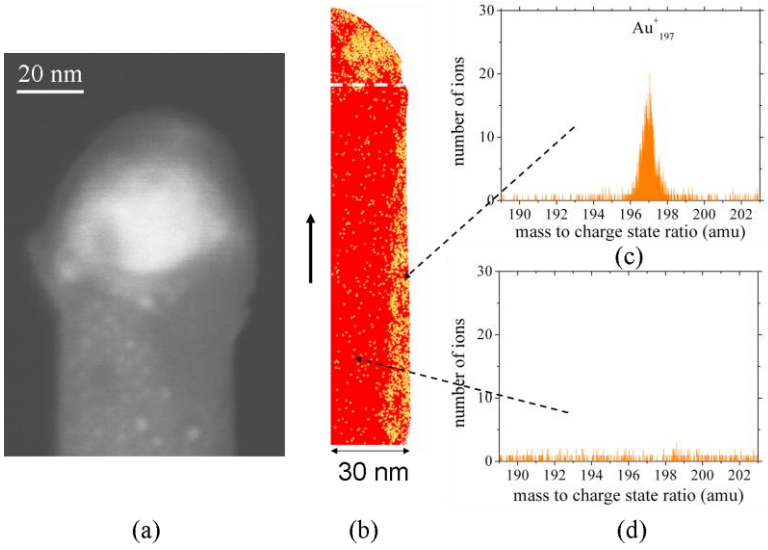

Figure IV.3 – Tomographic characterization of Au atoms in individual Si NW. (a) Scanning electron microscopy image of Si NW synthesized at low growth pressure. It clearly shows the existence of Au-rich droplet on top of NW and Au clusters on NW sidewall. (b) Analyzed volume of a Si NW by APT. Red dots correspond to Si atoms, whereas yellow dots are the signature of Au atoms. The vertical arrow indicates the NW growth direction. (c) and (d) are the mass to charge spectra of Au atoms on the NW sidewall and in the NW core respectively.

The advantage of APT is that the species can be located and viewed in 3D. Figure IV.4 (a) is a slice of the <111>-oriented Si NWs, where the (111) atomic planes are well characterized. This accurate inter plane distance (0.31 ± 0.01 nm) can be chosen as the reconstruction parameter. Figure IV.4 (b) and (c) are the 3D reconstruction of Si NW with a volume scale 30×27×143 nm^3, where 2300000 atoms are collected during the APT analysis. In this figure, Si, Au and O atoms have been represented by red, yellow and green dots respectively. The Au atoms can be detected clearly at the surface of the Si NW with a detection limit of 1.14×10^{19} at/cm^3, no Au atom is detected inside the NW. The O atoms are also detected at the surface of the Si NW (Figure IV.4 (c)). It should be pointed out that in the Figure IV.4 (c) the green dots inside the NW are not oxygen atoms but correspond to the background noise. Figure IV.4 (d) is the 3D reconstruction of iso concentration surface with 5% Au atoms (yellow) and 30% O atoms (green). The matrix (red) represents the Si atoms. The Au atoms exist on the Si NW sidewall and tend to aggregate to form clusters. Figure IV.4 (e) is the 45 °rotated view of Fig. 4 (d) given for clarity. The reconstruction of Figure IV.4 (d) and (e) are achieved with the Avizo software. As seen from Figure IV.4 (d), the NW sidewalls are covered with a thin layer of Si oxide. Interestingly, the Au clusters are also covered by a Si oxide layer. This phenomenon suggests that the oxidation of the Si NWs occurs after Si NWs are exposed to air and not in the CVD chamber. The average radius of Au cluster calculated from the pair correlation function g(r) is 1.5 nm. The concentration of Si atoms in the Au clusters is calculated to be 72% ±6 %, which is much more than the Si composition in bulk eutectic Au-Si alloy (24% of Si at our NW growth temperature).

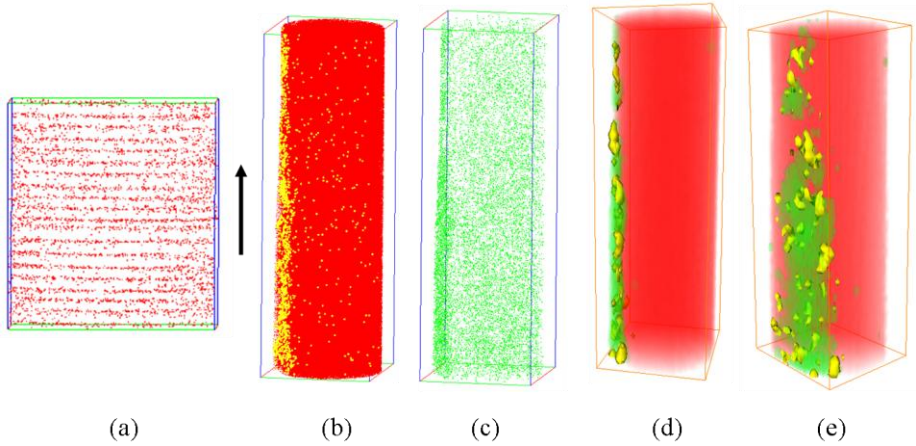

Figure IV.4 – 3D reconstruction of (a) a slice of Si [111] plane perpendicular to Si NW growth direction, (b) Au atoms (yellow dots) on the Si NW surface (red dots) and (c) oxygen atoms (green dots) on Si NW surface. The analyzed volume is 30×27×143 nm^3. The vertical arrows indicate the NW growth direction. Only 20% of the Si atoms are presented for clarity.

(d) The distribution of Au (yellow) and oxygen region (green) in the matrix of Si atoms (red) on the surface of Si NW are shown. (e) 45 °rotated view of the same volume.

Using these Au clusters, Si nano-branches can be grown from the backbone Si NW as shown in Figure IV.5. These Si nano-branches can further increase the surface-to-volume ratio of the NW. Before the synthesis of Si NWs, the Au droplets are prepared from the annealing of the Au thin film at 700 ℃ for 5 min in the CVD chamber prior to NW growth. Such a thermal treatment results in the formation of Au droplets with diameters ranging from 70 nm to a few hundred of nanometers. The experimental growth conditions are the same as in the previous case at low precursor pressure for inducing the formation of Au clusters on NW sidewall. It is clearly shown in Figure IV.5 that plenty of Si nano-branches grow around the Si NW sidewall. The mean diameter of the Si nano-branches is 6-8 nm, which is slightly larger than the typical diameter of Au clusters (3 nm), certainly due to Ostwald ripening of the Au clusters. The length of Si nano-branches at the base of Si NW is much longer than the one close the Au droplet due to the longer growth time.

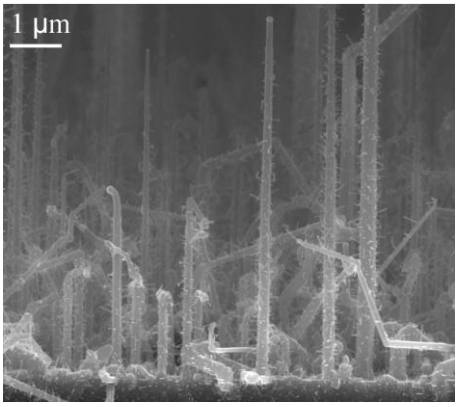

Figure IV.5 – Si nano-branches grown on Si NW at low silane partial pressure.

Finally, in order to analyze quantitatively the composition of this Si oxide layer, a composition profile along the cross-section is made, as shown in Figure IV.6. This profile has been made by moving a slice with a 1 nm step along the radial direction. The composition of this Si oxide layer is calculated to be: Si: 28.3%, O: 65.2% which is near the stoichiometry of SiO_2. It should be noted that the discrepancy of this value to 100% is due to the existence of Au atoms on the NW sidewall surface (Au: 6.5 %). It can be seen from Figure IV.6 that the interface between the Au cluster/SiO_2 region and the Si core of the NW is not abrupt: the diffusion of oxygen atoms into the Si NWs spreads over 4 nm.

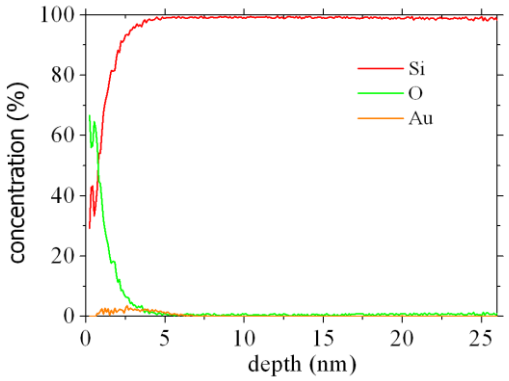

Figure IV.6 – Distribution of Si, O and Au atom composition along the cross-section of individual Si NW.

IV.1.2 High precursor pressure

In order to investigate the effect of the precursor pressure on the distribution of the catalyst (Au) atoms on the NW sidewall, Si NWs were also synthesized at high precursor pressure. The experimental growth condition is listed in Table IV.2. Silane is also diluted with hydrogen but in a ratio of 1:1 for achieving a higher precursor pressure. The total and silane partial pressure are kept at 0.798 mbar and 0.4 mbar respectively. The growth temperature and time are also 500 ℃ and 30 min.

Pressure (mbar)	T (℃)	SiH_4 (sccm)	H_2 (sccm)	Time (min)
0.798	500	50	50	30

Table IV.2 – Growth experimental condition of Si NWs synthesized at high silane pressure. Silane is chosen as the precursor gas. Hydrogen is used as the gas carrier.

In order to investigate the Si NW sidewall surface, a single Si NW is welded inclined on a W tip as in the previous case. The cleaved end of the Si NW is characterized by APT. Figure IV.7 shows the spatial distribution of the detected atoms in a reconstructed volume of 30 × 30 × 33 nm^3. The NW growth direction is <112> as determined by the APT using the stereographic projection of Figure IV.7 (b) and (c). The green and red dots represent the O and Si atoms respectively. Only Si and O atoms are detected during the APT analysis. There is no trace of Au atoms. The composition of the oxide layer corresponds to the native dioxide SiO_2.

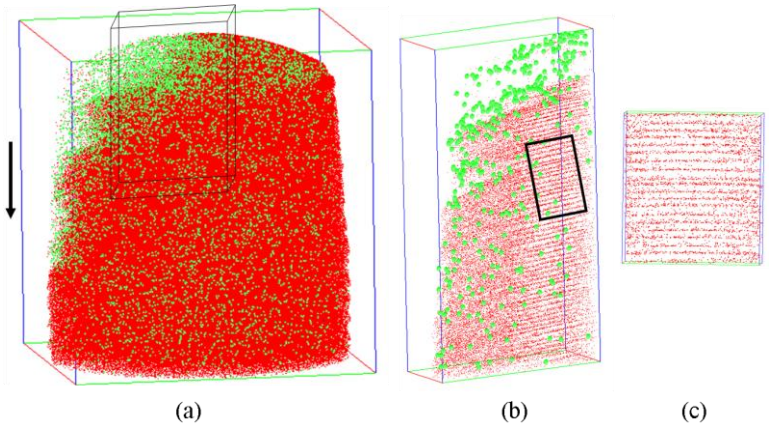

Figure IV.7 – (a) 3D reconstruction of the atom map distribution of a bottom end oriented intrinsic Si NW synthesized at high precursor pressure. The green and red dots represent the O ant Si atoms respectively. The reconstruction volume is 30 × 30 × 33 nm^3. Arrow indicates Si NW growth direction. (b) and (c) are cross section showing one of the [111] poles of Si NW with a <112> growth direction.

The comparison of this result with the one obtained at low silane partial pressure shows that no Au film or cluster is formed on Si NW sidewall at high silane pressure. Such a result is consistent with the results described in chapter III and in the literature [10, 11].

IV.2 Indium/Tin catalysts for the growth of Si nanowires

Other alternative catalysts such as Al [12], In [13] and Sn [14] have been explored in recent years in replacing Au for their incompatibility with the existing semiconductor technology. As it has been presented and discussed in the previous parts, Au atoms diffuse along the NW sidewalls. Wetting the NW sidewalls can lead to a thin metallic film that creates a Schottky barrier and modify the potential inside the NW core along the radial direction. Therefore, the diffusion of Au atoms causes a modification of NW properties that can be detrimental to its conductivity. In contrast to Au, the group III catalyst such as In can not only form an eutectic alloy with Si but also act as a p-type dopant. In this part, we investigate the role of catalysts consisting in an alloy between In and Sn for two different types of growth, the Vapor-Liquid-Solid (VLS) and Solid-Liquid-Solid (SLS) mechanisms. The melting temperatures of In and Sn are 156 ℃ [15] and 232 ℃ [16] respectively, which can provide the possibility to grow Si NWs at low temperatures. However, the nearly zero Si concentration in the catalyst droplet at the eutectic temperature [15] is a challenge for the

growth of Si NWs. Our goal is to study the catalyst atom distribution and concentration in the NW as such atomic species may diffuse in a similar manner as Au. In this work, the mixed catalysts droplets consisting of In and Sn atoms are prepared by a H_2 plasma treatment on the Indium Tin Oxide (ITO) substrate in a Plasma-Enhanced Chemical Vapor Deposition (PECVD) chamber with a typical rf power, H_2 flow rate, and chamber pressure of 5 W, 100 SCCM and 0.798 mbar respectively at a temperature of 300 ℃ for 1 min.

IV.2.1 By Vapor-Liquid-Solid (VLS) mechanism

The experimental growth conditions for VLS-grown Si NWs are listed in Table IV.3. The synthesis proceeds in a PECVD chamber. The total partial pressure is kept at 0.16 mbar. Silane has a flux of 10 sccm and it is diluted with hydrogen. The growth temperature and time are 500 ℃ and 15 min respectively. The NW growth temperature is much higher than the catalyst melting temperature. Although, Si NWs can be synthesized at low temperature such as 300 ℃, the morphology of the Si NWs was found to be irregular for such a low temperature [14].

Pressure (mbar)	T (℃)	SiH_4 (sccm)	Time (min)
0.16	500	10	15

Table IV.3 – Growth experimental condition of Si NWs synthesized with mixed catalysts of In and Sn via VLS mechanism. Silane is chosen as the precursor gas. Hydrogen is used as the carrier gas.

An SEM image of Si NWs catalyzed by In (Sn) via the VLS mechanism is presented in Figure IV.8. The diameter of the Si NWs is in the range of 150-200 nm with a typical length of 2-3 μm. We can observe that the In (Sn) catalyzed Si NWs are easily bent during the growth in comparison to the Au catalyzed Si NWs. As the diameter of the Si NWs is larger than 100 nm, the specimen preparation method described in chapter II.2.4.4 is used. An example of a single Si NW mounted on a W support tip before its welding by GIS and annular milling by FIB is shown in Figure IV.8 (b).

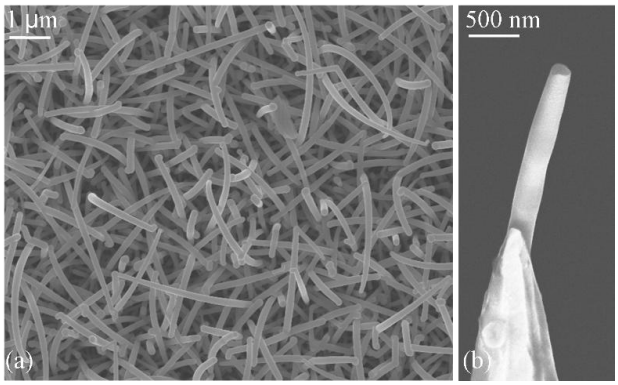

Figure IV.8 – Scanning electron microscopy image of VLS-grown Si NWs on an ITO substrate using mixed catalysts of In and Sn. (a) Top-view of the forest of Si NWs. The density of Si NWs is very high and the diameter is relatively large compared to Au catalyzed Si NWs. (b) A single Si NW is welded on a W support tip using the specimen preparation method described previously. The Si NW is directly taken from the Si NW forest in (a).

The mass-to-charge spectra of Si NW via the VLS mechanism using In and Sn as metal catalysts is presented in Figure IV.9. The existence of both types of catalyst materials in the Si NW is clearly observed in the core region of the NW, as shown by the detection of Sn^{++} and In^{+} isotope as shown in Figure IV.9 (a) and (b) respectively.

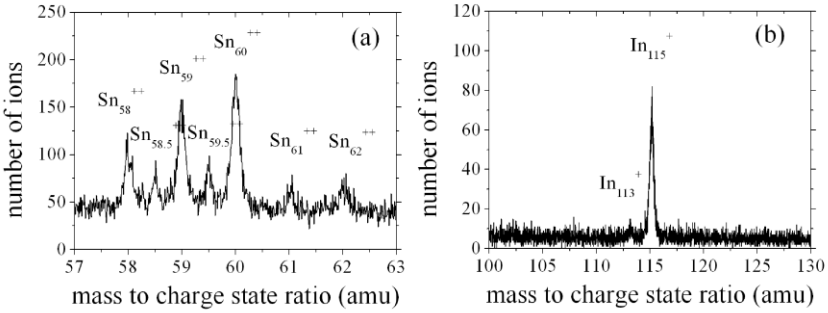

Figure IV.9 – Mass-to-charge spectra of Si NW via VLS mechanism using In and Sn as metal catalysts. Different isotopes of (a) Sn peaks (Sn^{++}) and (b) In peaks (In^{+}) have been distinguished by atom probe tomography.

The 3D reconstruction of an individual Si NW catalyzed by the mixed catalysts of In and Sn is performed by APT. Si, In and Sn atoms are represented by red matrix, blue dots and pink dots respectively in Figure IV.10. The Si crystalline [111] planes are resolved and the analyzed volume is $53 \times 53 \times 100$ nm^3. Note that only the NW core is investigated. Both In and Sn atoms are found to diffuse into the Si NW core during the growth with a concentration of $1.50 \pm 0.22 \times 10^{18}$ In/cm^3 and $6.85 \pm 0.54 \times 10^{18}$ Sn/cm^3 respectively. Such analysis thus reveals that a significant amount of In and Sn diffuse into NWs in comparison with Au.

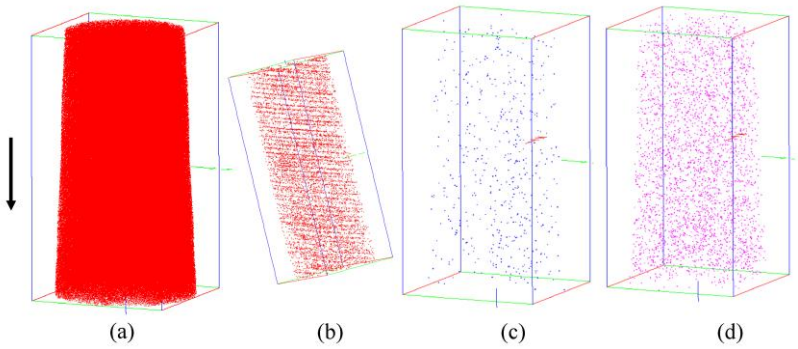

Figure IV.10 – Atom probe investigation of the core region of a Si NW synthesized with an alloy catalysts consisting of In and Sn via the VLS mechanism. The analyzed volume is 53×53×100 nm^3. The vertical arrow indicates growth direction. (a) 3D reconstruction of Si atoms. (b) Slice of the Si [111] crystalline planes normal to Si NW growth. The inter plane distance is 0.31 ±0.01 nm. (c) and (d) 3D distribution of In and Sn atoms respectively.

IV.2.2 By Solid-Liquid-Solid (SLS) mechanism

Using the same mixed catalysts, Si NWs are also synthesized by the SLS mechanism with two following steps: 1) The deposition of a thin amorphous Si:H layer with a typical thickness between 20 ~ 50 nm by the dissociation of pure SiH_4 under the following conditions: rf power, SiH_4 flow rate, and chamber pressure of 2 W, 10 SCCM, and 0.16 mbar at 100 ℃, respectively, 2) The annealing of the specimen in vacuum (10^{-6} mbar) at 500 ℃ for 15 h in order to activate the catalyst droplets to absorb the a-Si:H layer and produce crystalline Si NWs behind. A top-view of SEM image of in-plane Si NWs via the SLS mechanism is shown in Figure IV.11. The typical diameter of the Si NWs is 200 nm. The NWs have a length of several millimeters. The NW growth rate is calculated to 120 nm/s which is much higher than the one of the previous VLS-grown Si NWs (3 nm/s) at the same growth temperature. This higher growth rate of SLS-grown Si NWs is due to the direct contact of the a solid state a-Si:H with a 10^6-10^7 higher density than achievable in gas precursor [17]. The bright hemispherical protrusions correspond to the catalyst droplets. The inset image is a zoom of an in-plane Si NW with the catalyst droplet to the right. The diameter of the catalyst droplet is much larger than the one that form on the Si NWs grown by VLS. In this growth mode, the diameter of the Si NWs is directly controlled by the thickness of the a-Si:H layer rather than the catalyst droplet diameter. The magnified view also shows that the sidewalls of SLS-grown Si NWs are rougher than the VLS-grown Si NWs. A channel following the catalyst droplet is visible on each side of the NW. Based on the APT specimen preparation method described in

chapter II.4, a piece of the sample containing a NW was prepared. Such a preparation requires an additional step: the detachment of a single in-plane Si NW from the ITO substrate, where a slice of the NW is cut midway along its length with the micro manipulator. Figure IV.11 (b) shows one portion of in-plane Si NW which is detached from the ITO substrate and mounted on a W tip before welding by GIS and milling by FIB.

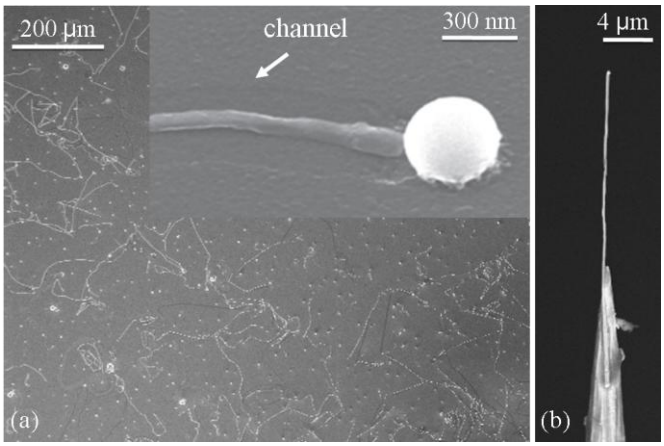

Figure IV.11 – Scanning electron microscopy image of SLS-grown Si NWs on an ITO substrate using the mixed catalysts of In and Sn. (a) Top-view of Si NW. The length of Si NW can reach several millimeters with a diameter of 200 nm. The inset is a magnification of the droplet with its diameter much larger than the one of the Si NW. (b) A single Si NW welded on a W support tip.

IV.2.2.1 Impurity concentration in Si nanowires

Figure IV.12 is the 3D reconstruction of one portion of an in-plane Si NW. The analyzed volume is $52 \times 52 \times 100$ nm^3. In the reconstruction volume, each dot represents one atom and different atoms are represented with different colors (Si, In and Sn are presented as red, blue and pink respectively as indicated in Figure IV.12). In and Sn atoms can be clearly detected. The In and Sn concentration amount are $2.72 \pm 0.16 \times 10^{19}$ In/cm^3 and $1.06 \pm 0.02 \times 10^{20}$ Sn/cm^3 respectively. The APT characterization reveals that In and Sn atoms are distributed uniformly in the analyzed volume. An extracted reconstruction slice, as presented in Figure IV.12 (c), shows a discrete distribution of the In atoms among the Si (111) crystallographic planes (for clarity, only Si and In atoms are presented).

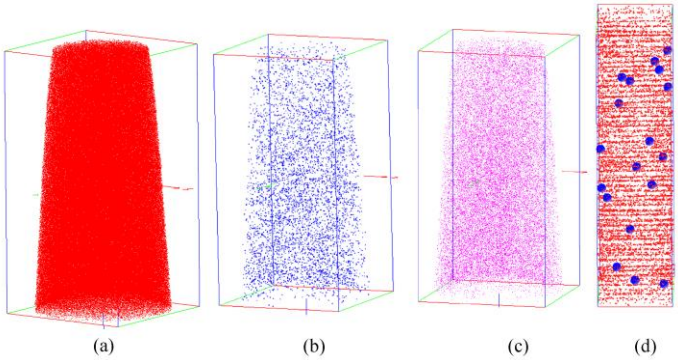

Figure IV.12 – 3D reconstruction of one portion of Si NW synthesized via SLS mechanism. The reconstruction volume is 52×52×100 nm^3. (a)-(c) Si, In and Sn atoms are clearly detected and are represented with red, blue and pink color respectively in the reconstruction volume. (d) A reconstruction slice of In atoms in Si (111) planes. The reconstruction volume is 5×5×20 nm^3. Only Si and In atom are represented for clarity.

The analyses of several Si NWs reveal that the In concentration has a relative stable value (1.50-3.69×10^{19} In/cm^3), whereas the Sn concentration varies (1.35-10.6×10^{19} Sn/cm^3) as plotted in Figure IV.13. The electrical measurements of these Si NWs show that their conductivity is similar and corresponds to the activation of In impurities with a concentration of ~ 1.5×10^{19} In/cm^3 [18].

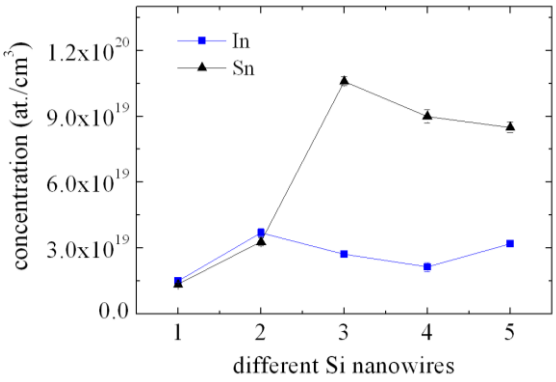

Figure IV.13 – In and Sn concentration measured from five different individual Si NWs (same specimen) by atom probe tomography. A stable In concentration in Si NW is observed, whereas the Sn concentration varies from one NW to another.

The comparison between both growth modes suggests that the concentration of In and Sn atoms in in-plane Si NWs via the SLS mechanism is much higher as compared to the one via the VLS mechanism. One possible explanation is proposed as follow taking into account the fluid mechanic. For VLS case, the incorporation of impurity into NW is assumed proceeds via a diffusion process, whereas, for SLS case, the incorporation of impurity into NW could

be assisted by a viscous flow due to the rotation of the catalyst droplet during NW growth [17]. The calculation in the literature [19, 20] shows that the diffusion process can be neglected in comparison to the viscous flow. Therefore, more impurity atoms can be incorporated into SLS-grown Si NWs. The diffusion pathway under these conditions is rather complex and will be not described in this work.

IV.2.2.2 In segregation in Si nanowires

The distribution of the impurities has a role on their electrical activity. As shown previously in Figure IV.12, In and Sn atoms can distribute uniformly in some portion of the Si NW. However, it is not always the case. In the reconstructed volume of Figure IV.14, different atomic elements are represented with different colors (Si, In and Sn are presented as red, blue and pink respectively). The analyzed volume is $52 \times 52 \times 157$ nm^3. In and Sn atoms can be clearly detected. Figure IV.14 (a), (b) and (c), (d) are the cross-section and normal view of the In and Sn atom distributions in the Si NW respectively. In these 3D reconstructions, In and Sn atoms are distributed in different manners. Whereas Sn atoms are uniformly distributed in the Si NW, In atoms segregate or form clusters. The In and Sn concentration are measured to be $1.50 \pm 0.06 \times 10^{19}$ In/cm^3 and $1.35 \pm 0.05 \times 10^{19}$ Sn/cm^3 respectively. The In concentration is much higher compared to its solid solubility in Si at our growth temperature of 500 ℃ (~ 10^{17} In/cm^3) [21, 22], whereas, the Sn concentration is close to its solid solubility in Si (~ 10^{19} Sn/cm^3) [23, 24]. For this solid solubility reason, In atoms are segregated at the stacking faults, whereas, Sn atoms are distributed uniformly. The segregation of the In atoms is confirmed with the study of lamellar [112] twins observed with HRTEM.

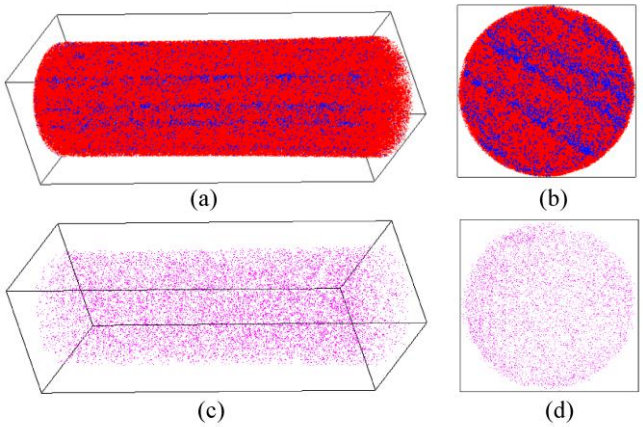

Figure IV.14 – 3D atomic mapping of one portion of an individual in-plane Si NW grown via SLS mechanism. The analyzed volume is $52 \times 52 \times 157$ nm^3. Si, In and Sn atoms are presented

as red, blue and pink respectively. (a) and (b) Cross-section and normal view of In atom distribution in a Si NW. (c) and (d) Cross-section and normal view of Sn atom distribution in the same Si NW.

The diffusion of impurity atoms inside the crystalline lattice is believed to be a thermally active process. Therefore, the impurity diffusivity can influence their distribution in the lattice. An impurity such as In with high diffusivity (10^{-22} cm^2/s [25]) can diffuse easily to the stacking faults in comparison to Sn with its low diffusivity (10^{-24} cm^2/s [25]). This can induce a segregation of In atoms and a uniform distribution of Sn atoms (Figure IV.14). The maximum diffusion length at 500 ℃ for 15h (total NW growth time) is estimated to 0.5 nm, this clearly shows that the diffusion of impurity can be accelerated by the existence of the extended defects such as stacking faults with an increase of diffusivity of almost three orders of magnitude as compared to the bulk one [26].

In Figure IV.15 (a), a one-dimensional concentration profile of the In concentration is drawn by moving a slice with a 1 nm step along the red arrow of Figure IV.15 (b). The In concentration in the region where it has segregated and in the matrix are measured to be 3.0 ± 0.28 $\times 10^{19}$ In/cm^3 and 5.6 ± 1.5 $\times 10^{18}$ In/cm^3 respectively. Figure IV.15 (c) is the iso concentration of In atoms in an individual Si NW. In these regions, the In concentration of the cluster reaches 2.0 ± 1.0 $\times 10^{21}$ In/cm^3. In conclusion, In can substitute to Si as single impurities, but it also form clusters, that could be metallic inside the semiconductor core of the NW.

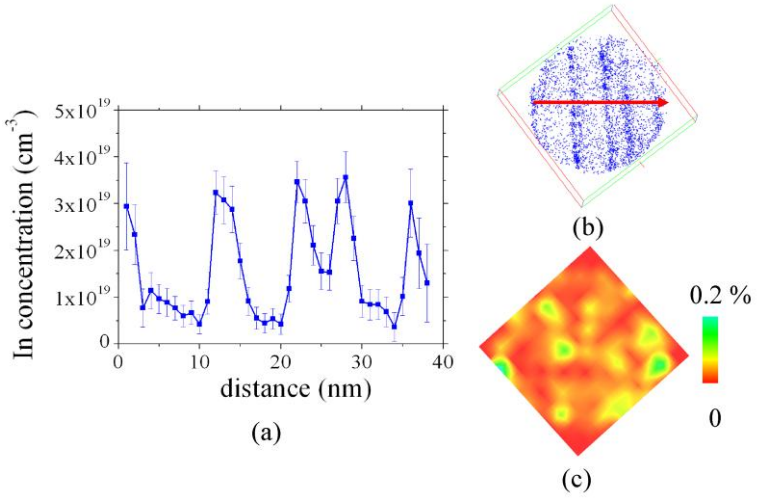

Figure IV.15 – Atomic scale characterization of In segregation in a single in-plane Si NW via SLS mechanism. (a) In concentration profile along the cross-section. The profile is taken along the red arrow in (b). Cross-section view of In segregation in a single Si NW. The

analyzed surface is 40×40 nm^2. (c) Iso concentration of In atoms in an individual Si NW. The scale bar with color represents the change of In concentration in the Si NW.

Assuming an equilibrium segregation process, the segregation energy (ΔE) then can be calculated. According to McLean's thermodynamic arguments [27], the segregation energy can be calculated from the average concentration B in the segregation (C_B) and the one in the matrix around the defect (C_A) as

$$\frac{C_B}{C_A} = \exp\frac{\Delta E}{kT}$$

where *k* is Boltzmann's constant and *T* is the NW growth temperature. In this defect, C_B = 3.0 ± 0.28 ×10^{19} In/cm^3 and C_A = 5.6 ± 1.5 ×10^{18} In/cm^3. Then, ΔE can be calculated to be 0.12 ± 0.01 eV. This value is lower than the segregation energy of B in loop defects (0.35 eV) [28].

Another type of catalyst atom distribution in the in-plane Si NW is shown in Figure IV.16. In and Sn atoms are presented with blue and pink dots respectively. The analyzed volume is 32×32×86 nm^3. The In concentration is 3.69 ± 0.20× 10^{19} In/cm^3. Again, it can be clearly seen that In atoms segregate in the Si NW and form several clusters. The In concentration in the region where In has segregated is 1 ± 0.08 × 10^{20} In/cm^3. In contrast, the In concentration in the matrix is very low with an upper bound of 1×10^{18} In/cm^3. This value is lower than the In concentration found in the VLS-grown Si NWs. Interestingly, Sn atoms are not distributed uniform anymore but segregate in the Si NW core. The Sn concentration is measured to be 3.28 ± 0.19 × 10^{19} Sn/cm^3 which is higher than its solid solubility. The Sn concentration in the region that are Sn-rich or Sn-poor amount to 7.0 ± 0.62 ×10^{19} Sn/cm^3 and 1.8 ± 1.2 ×10^{19} Sn/cm^3 respectively.

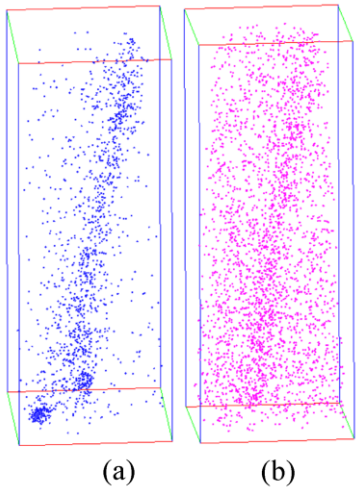

Figure IV.16 – 3D atomic mapping of catalyst atoms in an in-plane Si NW synthesized via the SLS mechanism. In and Sn atoms are presented with blue and pink dots respectively. The

analyzed volume is 32×32×86 nm^3. (a) Segregation and clusters of In atoms in the Si NW. (b) Segregation of Sn atoms in the same Si NW.

In order to investigate the structural region where a high concentration of In was found, HRTEM (by Dr. G. Patriarche at LPN) was also used in order to characterize the crystalline structure of in-plane Si NWs via the SLS mechanism. Figure IV.17 show HRTEM images of the in-plane Si NWs. One portion of a single in-plane Si NW is presented in Figure IV.17 (a). It shows clearly the presence of stacking defaults. Figure IV.17 (b) is a magnified view of a portion of the Si NWs. Defect lines appear brighter compared to other regions. These regions with more contrast correspond to high concentration of impurity catalyst atoms (In or Sn or both), because In and Sn are atoms that are much heavier than the matrix Si atoms. It reveals that the impurity atoms can segregate uniformly along Si NW or form nano clusters and the planar segregations are parallel one to each other as shown by APT. Figure IV.17 (d) shows the crystalline structure and lamellar twins with higher contrast. The inter plane distance and the twin angle are measured to be 0.22 nm and 142 °which indicates that these twin plane has [112] orientation.

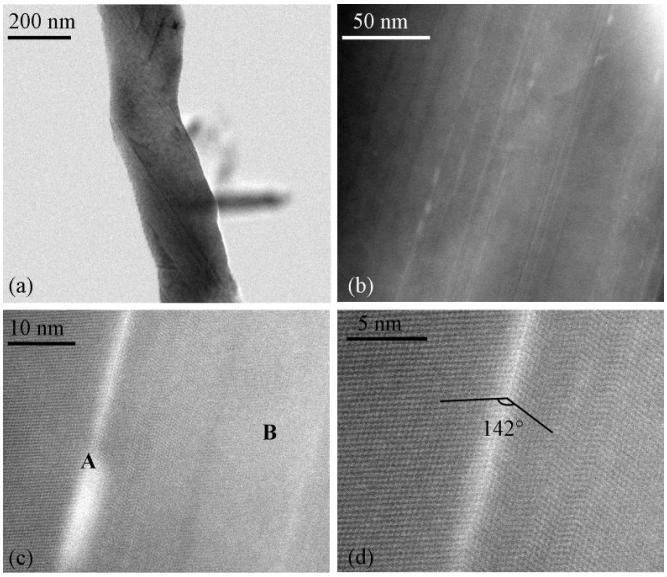

Figure IV.17 – High resolution transmission electron microscopy images of in-plane Si NW synthesized via SLS mechanism. (a) One portion of Si NW with defect lines. (b) High magnified view of one portion of Si NW with the impurity catalyst (In or Sn or both) in Si NW. (c) Higher magnified view. Two regions with a different contrast are labeled A and B. (d) Multiple [112] twins. One of them is made up of an impurity plane. The high resolution transmission electron microscopy characterization was performed by G. Patriarche in LPN, Marcoussis.

Figure IV.18 presents comparative images of In segregation in in-plane Si NWs characterized by HRTEM (Figure IV.18 (a)) and APT (Figure IV.18 (b) and (c)). For APT image, only 20% of Si atoms are presented for clarity.

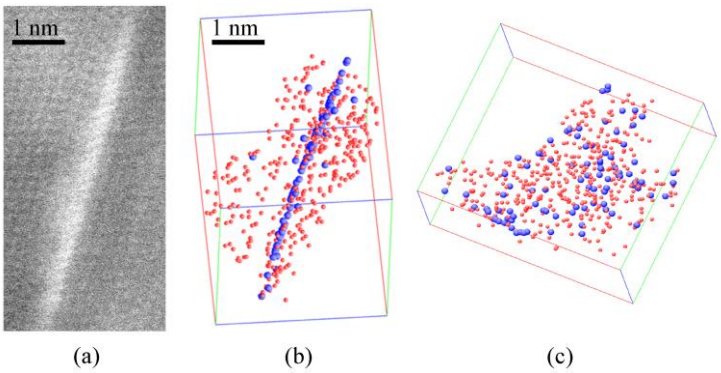

Figure IV.18 – Comparison between HRTEM and APT images showing In segregation characterized by (a) high resolution transmission electron microscopy and (b), (c) atom probe tomography. Only 20% of Si atoms are presented for clarity. (c) is the same volume as (b) with a rotation of 90°. HRTEM image has been obtained by Dr. G. Patriarche at LPN Laboratory.

Stacking faults are a rather common phenomenon in Si NWs. Indeed, they can also be found in Si NWs synthesized by other synthesis methods such as Supercritical Fluid-Liquid-Solid (SFLS) [29, 30], CVD [31] and PECVD [32] as well as in other semiconductor material such as GaP [33] and Ge [34]. Under given growth condition, VLS-grown Si NWs exhibit the same stacking faults [31]. It should be pointed here that the existence of twin in material has its own advantages. For example, it is possible to increase the mechanical and electrical properties of copper thin film by increasing the twin densities [35, 36]. As far as the orientation of twins is concerned, two different types of twins, namely, transverse and parallel to NW growth direction, exist. The accumulation or trapping of impurity atoms on extended defects such as stacking defaults and dislocations is also a rather general phenomenon such as the Cottrell atmosphere around Si defects [37]. The interaction between these impurity atoms and the extended defects are also extensively studied [26, 38]. Several reasons are at the origin of extended defects in semiconductor materials during their elaboration or after treatment such as ion implantation or mechanical strength. The stacking faults in our Si NWs are formed spontaneously during the NW growth. As the stacking faults can influence greatly the material properties, it is an important issue to attempt to understand how these faults are formed.

A two-dimensional nucleation-based model is proposed to explain the form of the longitudinal twins during the NW growth. The existence of stacking faults is due to the instabilities at the interface between the catalyst droplet and the NW. That is to say, the faults in NWs are transferred from the interface into NW. Figure IV.19 shows the schematic illustration of twin formation for SLS-grown NWs. It is assumed that the nucleation in the catalyst droplet of SLS-grown NWs follows the growth mode of mono nucleus and layer-by-layer as for VLS-grown NWs [39, 40]. In this case, the growing interface is assumed to be flat and continuous as illustrated in Figure IV.19 (a) with a red dashed line. The interface can be viewed as a semi molten state between liquid droplet and solid NW. At given growth condition, with high nucleation rate, this growth mode is no more adapted. Instead, the poly-nuclei growth mode is preferred but still with a layer-by-layer growth (Figure IV.19 (b)). The nucleation mode becomes poly-nuclei and multi layers (islands) with the increase of the supersaturation (in favor of an increase of the nucleation rate). This is due to the fact that at high supersaturation, the kink site, which is the preferential nucleation site, is no more the only nucleation site. The nucleation on the crystal surface could also occur according to the Terrace Ledge Kink model [41]. This process can induce the formation of several crystalline islands at the interface. Therefore, the interface with several nucleation sites is not flat any more as shown in Figure IV.19 (c). This lack of flatness at the interface can induce the formation of twins during nucleation. Therefore, it can be concluded that several pyramids can generate multi twins [32, 42].

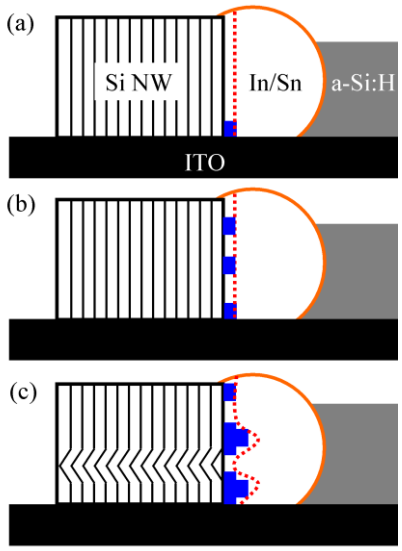

Figure IV.19 – Schematic illustration of longitudinal twin formation during NW growth. (a) Nucleation mode of mono nucleus and layer-by-layer for SLS-grown NWs. (b) Nucleation mode of poly-nuclei and layer-by-layer. (c) Nucleation mode of poly nuclei and multi layers.

Now, coming back to the impurity incorporation and segregation in NW. It is shown in the model above that twin defects may be transmitted from the molten nucleation interface into the solid NW. Based on this concept, the segregation of impurity in the NW could occur during the crystallization of the NW (between poly-nuclei) rather than by a solid diffusion process. However, owing to our experimental results, this process should not occur. Indeed, if the segregation of impurity occurs during the nucleation, no transport of impurity, either In or Sn, is needed due to the very fast nucleation of layers (estimation to 2.6 ms from growing of one monolayer). Thus, In and Sn should be introduce in the same way, with same quantity and same spatial distribution in the NW. But, this is contradictory with our APT results. Therefore, we can conclude that the segregation of impurities must occur via a solid diffusion mechanism in NW.

IV.3 Conclusion

In summary, different catalysts (Au, In and Sn) are used to synthesize Si NWs via the different growth mechanisms (VLS and SLS) in order to study their influences on the incorporation of catalyst atoms in the Si NWs.

For Au-catalyzed Si NWs via the VLS mechanism, the upper bound of Au concentration residing in the NW core is measured to be 3×10^{17} Au/cm^3 either at a low pressure or a high pressure of the precursors. It is found that at a low growth pressure the Au atoms will migrate from the Au-rich droplet on NW sidewall and will form nano clusters. The diameter and concentration of these nano clusters were measured. Subsequently, nano branches can be grown by taking advantage of these nano clusters. However, the existence of Au atoms on NW sidewall can modify the NW property through the formation a Schottky barrier. The existence of SiO_2 is also evidenced on the Si NW sidewall.

Mixed catalysts of In and Sn have also been investigated. In the VLS growth mode, they tend to distribute uniformly. In contrast, in the SLS growth mode, there is the formation of lamella twin defects due to the roughness of nucleation interface. Such defects favor the segregation of impurities that arrange into clusters. This kind of clusters may compensate the electrical activity role of the individual In impurity.

Bibliography of chapter IV

[1] J. Holden, S. Holden, and B. Singer, Crystals and Crystal Growing, The MIT Press (1982)
[2] Y. C. Cao, Science, 332, 48 (2011)
[3] J. E. Allen, E. R. Hemesath, D. E. Perea, J. L. Lensch-Falk, LiZ.Y, F. Yin, M. H. Gass, P. Wang, A. L. Bleloch, R. E. Palmer, and L. J. Lauhon, Nat. Nanotechnol., 3, 168 (2008)
[4] A. Huijser, T. J. Savenije, J. E. Kroeze, and L. D. A. Siebbeles, J. Phys. Chem. B, 109, 20166 (2005)
[5] D. H. K. Murthy, T. Xu, W. H. Chen, A. J. Houtepen, T. J. Savenije, L. D. A. Siebbeles, J. P. Nys, C. Krzeminski, B. Grandidier, D. Stievenard, P. Pareige, F. Jomard, G. Patriarche, and O. I. Lebedev, Nanotechnology, 22, 315710 (2011)
[6] Y. Wu, Y. Cui, L. Huynh, C. J. Barrelet, D. C. Bell, and C. M. Lieber, Nano Lett., 4, 433 (2004)
[7] V. Schmidt, S. Senz, and U. Gosele, Nano Lett., 5, 931 (2005)
[8] A. Lugstein, M. Steinmair, Y. J. Hyun, G. Hauer, P. Pongratz, and E. Bertagnolli, Nano Lett., 8, 2310 (2008)
[9] C. B. Collins, R. O. Carlson, and C. J. Gallagher, Phys. Rev., 105, 1168 (1957)
[10] T. Kawashima, T. Mizutani, T. Nakagawa, H. Torii, T. Saitoh, K. Komori, and M. Fujii, Nano Lett., 8, 362 (2008)
[11] P. Madras, E. Dailey, and J. Drucker, Nano Lett., 10, 1759 (2010)
[12] O. Moutanabbir, S. Senz, R. Scholz, M. Alexe, Y. Kim, E. Pippel, Y. Wang, C. Wiethoff, T. Nabbefeld, F. Meyer zu Heringdorf, and M. Horn-von Hoegen, ACS Nano, 5, 1313 (2011)
[13] R. Q. Zhang, Y. Lifshitz, D. D. D. Ma, Y. L. Zhao, T. Frauenheim, S. T. Lee, and S. Y. Tong, The Journal of Chemical Physics, 123, 144703 (2005)
[14] L. Yu, P.-J. Alet, G. Picardi, I. Maurin, and P. R. i. Cabarrocas, Nanotechnology, 19, 485605 (2008)
[15] H. Baker, and H. Okamoto, ASM Handbook: Volume 3: Alloy Phase Diagrams, ASM International, 2·259 (1992)
[16] H. Baker, and H. Okamoto, ASM Handbook: Volume 3: Alloy Phase Diagrams, ASM International, 2·365 (1992)
[17] L. Yu, P.-J. Alet, G. Picardi, and P. Roca i Cabarrocas, Phys. Rev. Lett., 102, 125501 (2009)
[18] L. Yu, W. H. Chen, G. Patriarche, S. Bouchoule, P. Pareige, R. Rogel, A. C. Salaun, L. Pichon, and P. Roca i Cabarrocas, Applied Physics Letters 99 (20), 203104 (2011).
[19] W. Mullins, J. Appl. Phys., 30, 77 (1959)
[20] F. Yang, J. Appl. Phys., 80, 6188 (1996)
[21] G. Backenstoss, Phys. Rev., 108, 1416 (1957)
[22] R. Olesinski, N. Kanani, and G. Abbaschian, Journal of Phase Equilibria, 6, 128 (1985)
[23] F. A. Trumbore, C. R. Isenberg, and E. M. Porbansky, J. Phys. Chem. Solids, 9, 60 (1959)
[24] K. Min, Appl. Phys. Lett., 72, 1884 (1998)
[25] S. W. Jones, Diffusion in Silicon, ICKnowledge LCC, Georgetown, MA (2006)
[26] M. Legros, G. Dehm, E. Arzt, and T. J. Balk, Science, 319, 1646 (2008)
[27] D. McLean, Clarendon Press, Oxford (1957)
[28] S. Duguay, Appl. Phys. Lett., 97, 242104 (2010)
[29] A. H. Carim, K. K. Lew, and J. M. Redwing, Adv. Mater., 13, 1489 (2001)

[30] F. M. Davidson, D. C. Lee, D. D. Fanfair, and B. A. Korgel, J. Phys. Chem. C, 111, 2929 (2007)
[31] F. J. Lopez, E. R. Hemesath, and L. J. Lauhon, Nano Lett., 9, 2774 (2009)
[32] S. Conesa-Boj, I. Zardo, S. Estrade, L. Wei, P. Jean Alet, P. Roca i Cabarrocas, J. R. Morante, F. Peiro, A. F. i. Morral, and J. Arbiol, Cryst. Growth Des., 10, 1534 (2010)
[33] J. Johansson, L. S. Karlsson, C. Patrik T. Svensson, T. Martensson, B. A. Wacaser, K. Deppert, L. Samuelson, and W. Seifert, Nat. Mater., 5, 574 (2006)
[34] S. Barth, J. J. Boland, and J. D. Holmes, Nano Lett., 11, 1550 (2011)
[35] L. Lu, Y. Shen, X. Chen, L. Qian, and K. Lu, Science, 304, 422 (2004)
[36] L. Lu, X. Chen, X. Huang, and K. Lu, Science, 323, 607 (2009)
[37] K. Thompson, P. L. Flaitz, P. Ronsheim, D. J. Larson, and T. F. Kelly, Science, 317, 1370 (2007)
[38] K. Sumino, and I. Yonenaga, Solid State Phenomena, 85-86, 145 (2001)
[39] V. G. Dubrovskii, and N. V. Sibirev, Phys. Rev. E, 70, 031604 (2004)
[40] C.-Y. Wen, M. C. Reuter, J. Bruley, J. Tersoff, S. Kodambaka, E. A. Stach, and F. M. Ross, Science, 326, 1247 (2009)
[41] J. F. Nicholas, Landolt-Börnstein: Numerical Data and Functional Relationships in Science and Technology, 24a, Sringer (2008)
[42] C. Cayron, M. Den Hertog, L. Latu-Romain, C. Mouchet, C. Secouard, J.-L. Rouviere, E. Rouviere, and J.-P. Simonato, J. Appl. Crystallogr., 42, 242 (2009)

Chapter V

V Dopant metrology in “out of plane elaboration” Si nanowires (etching and VLS): an atom probe approach

For application such as the solar cells, one important issue is to increase the photon collector surface. The “out of plane elaboration” of Si NWs can improve this due to the large surface to volume ratio considering Si NWs. As it is naturally an intrinsic material, Si NWs need to be doped for their use in solar cell devices. In order to understand the doping process, whatever is the process, the characterization of an individual Si NW is necessary. As a nano object characterization technique, the atom probe gives us the opportunity to have the information on the dopant distribution and concentration in a single Si NW.

In this chapter, the dopant metrology in Si NWs synthesized respectively by “top-down” or “bottom-up” approaches is realized using APT. It will be presented and discussed following two parts:

i) Si NWs synthesized by the “top-down” approach. The distribution and concentration of B in individual Si NWs are presented and discussed.

ii) Si NWs synthesized by the “bottom-up” approach. The distribution and concentration of B and P in individual Si NWs with different morphology are measured and discussed. A model suggesting the doping mechanism is proposed and discussed in order to explain the experimental observations.

V.1 Si nanowires elaborated by etching

At first, Si NWs synthesized by the “top-down” approach are characterized by APT. Si NWs are fabricated from a B-doped Si wafer (with a homogeneous B doping of 1×10^{19} B/cm^3) using the Langmuir-Blodgett assembly and etching as described in chapter I.1.2.1. Figure V.1 (a) and (b) are SEM images of Si NWs on a Si wafer showing the cross-section view and top view respectively. The sidewall of Si NWs exhibits a saw tooth facets just as for Si NWs synthesized by the “bottom-up” approach, namely, the CVD method. But in this case the origin of these two kinds of saw tooth facets is different. The facet on Si NWs grown by “bottom-up” approach is the result of the evolution of the catalyst droplet whereas the facet on Si NWs grown by “top-down” is due to the anisotropic etching. Indeed, the NW fabrication process by etching includes two successive and alternate steps: the passivation and the etching.

The couple SF_6/O_2 is used for the etching of the substrate and C_4F_8 is used as the passivation gas. However, during the etching, a part of SF_6/O_2 can also remove the passivation layer. This "depassivation" step plays an important role for in the facet formation.

Figure V.1 clearly shows that the morphologies of Si NWs: NW length, diameter, density and orientation are well controlled in comparison to Si NWs issue from the "bottom-up" approach. This is an important aspect as far as the integration of Si NW into device such as solar cell is considered. The control of the doping of NW is as important as controlling the NW morphology. Therefore, in the next paragraph, we use the APT technique to investigate these Si NWs in order to consider whether the doping of Si NWs is well controlled or not.

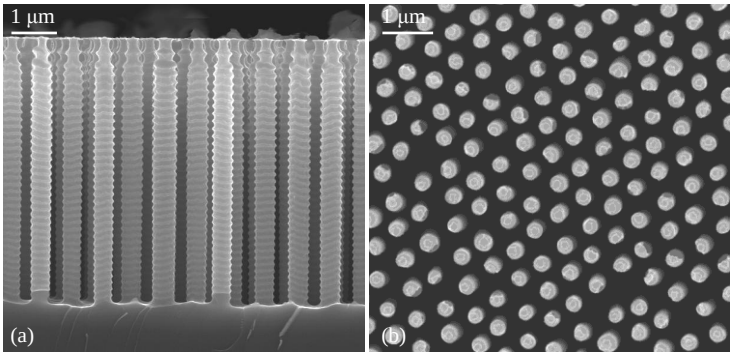

Figure V.1 – Scanning electron microscopy images of B-doped Si NWs synthesized by "top-down" approach: (a) cross-section view and (b) top view.

The diameter of these Si NWs is in the range of 400 nm which is too large for APT investigation. Therefore, the Si NW needed to be ion-milled by FIB after mounting on a support tip. The 3D reconstruction of a volume of B-doped Si NW is shown in Figure V.2. Si and B atoms are represented by red and black dots respectively. The analyzed volume is $34 \times 34 \times 130$ nm^3.

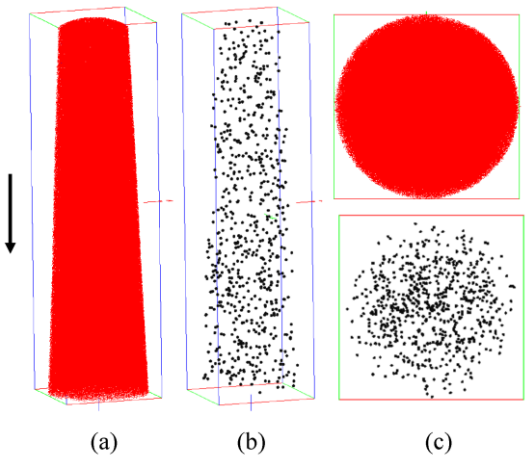

Figure V.2– Atom probe investigation of an individual B-doped Si NW core region. Si NW is fabricated by the "top-down" approach. Three-dimensional tomographic reconstruction of (a)

Si atoms and (b) B atoms. (c) Cross-section view of Si and B atoms. B distribution is uniform in Si NW. The analyzed volume is 34×34×130 nm^3. Arrow indicates Si NW etching direction.

It can be concluded from Figure V.2 that either the axial or the radial B distribution is homogeneous. This is confirmed from the calculation of "frequency distribution" and the Chi-square test[2] as shown in Figure V.3. Three different Si NWs extracted from the same etched wafer are measured. In Figure V.3, the comparison between the experimental distribution and binomial distribution of B atoms in Si NWs is shown. Figure V.3 clearly reveals that the B atoms in Si NWs are randomly distributed. This observation is reasonable as B atoms are uniformly distributed in the Si wafer before the fabrication process. The etching process itself does not induce any modification of the B distribution. As a conclusion, the B distribution in Si NWs synthesized by the "top-down" approach does not suffer from any change during the fabrication process.

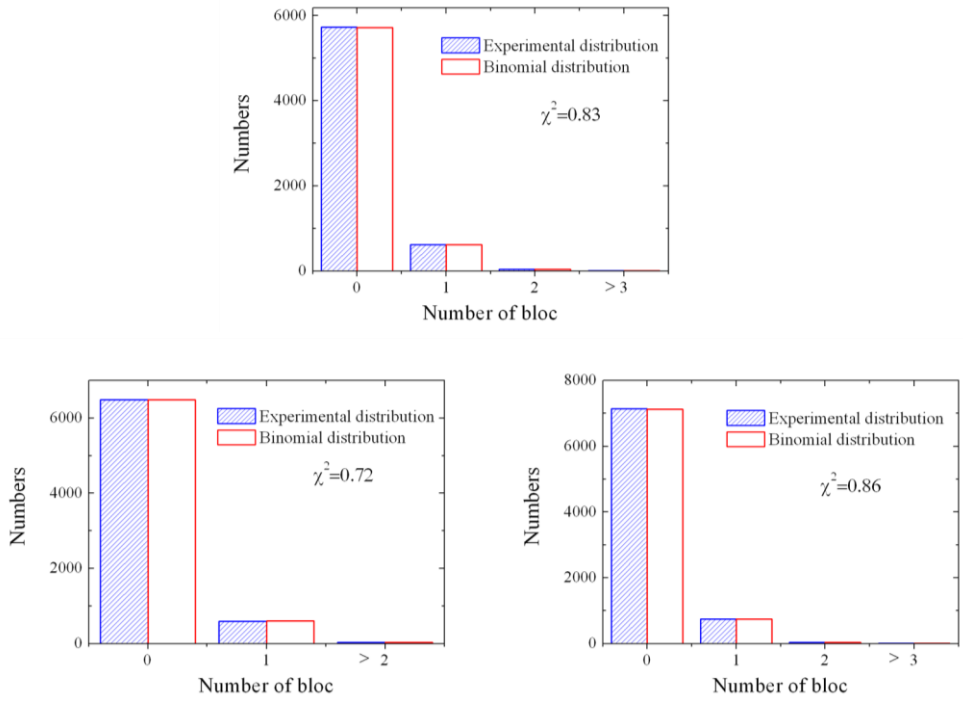

Figure V.3 – Comparison between the experimental distribution and the binomial distribution of B atoms in Si NWs.

The B concentrations in individual Si NW are quantitatively measured and plotted in Figure V.4. The mean B concentration is calculated to be 1.1 ± 0.1 ×10^{19} B/cm^3. This value is

[2] It is a statistical law which shows the homogeneity of the distribution. For an ideal homogeneous distribution, the value of χ^2 will reach 0.999.

of the same order than the initial doping concentration of the Si wafer (1×10^{19} B/cm^3). Therefore, the NW fabrication process has no influence on the dopant concentration.

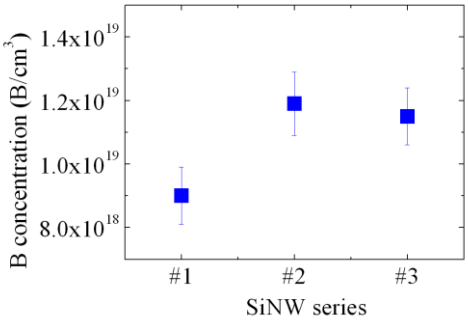

Figure V.4 – B concentration measured in three different Si NWs from the same specimen. The mean B concentration in Si NWs is measured to be 1.1 ±0.1 ×10^{19} B/cm^3

As a partial conclusion, it can be stated that no change of B distribution and concentration is involved during the NW fabrication following the etching process Therefore, the control of B distribution and concentration in Si NWs synthesized by etching can be realized by controlling the initial Si bulk. This part confirms the advantage of Si NWs synthesized by the "top-down" approach that either the morphology or the doping of Si NW can be effectively controlled.

An additional characterization has been performed in order to investigate the out diffusion of dopant [1] under heat treatment. Therefore, we annealed at 900 ℃, B-doped Si NWs synthesized by etching (same as above). The heat treatment was performed under ultra high vacuum for 3 hours. Three Si NWs were investigated. The preparation method for APT characterization of NW is the same as above. The 3D reconstruction of annealed B-doped Si NW is shown in Figure V.5. Si and B atoms are represented by red and black dots respectively. The analyzed volume is $32\times32\times120$ nm^3. The calculation of the "frequency distribution" and the Chi-square test with the value χ^2 of 0.77, 0.85 and 0.79 clearly reveals that the B atoms are also randomly distributed in the core of Si NWs after annealing. The mean B concentration is calculated to be $1.1 \pm 0.2 \times10^{19}$ B/cm^3. So, no redistribution of B in the NW after annealing is observed. This is in good agreement with the solubility limit of the system equal to 6.2×10^{19} B/cm^3 (from $C = 9.25\times10^{22} \exp(-0.73\text{eV}/k_BT)$ [2]). It must be noted here, that if there is a surface effect on the boron distribution, we did not succeed to observe it because only the core of NW has been studied. The need to FIB the specimen to sharpen it does not allow the surface to be studied by APT as explained previously. A more complex APT sample preparation method is needed as described in chapter II.2.4.3 which is under

development in order to determine the nanoscale surface effect. One can conclude that if there is a surface effect on the dopant redistribution it is much localised and does not affect the core of the system.

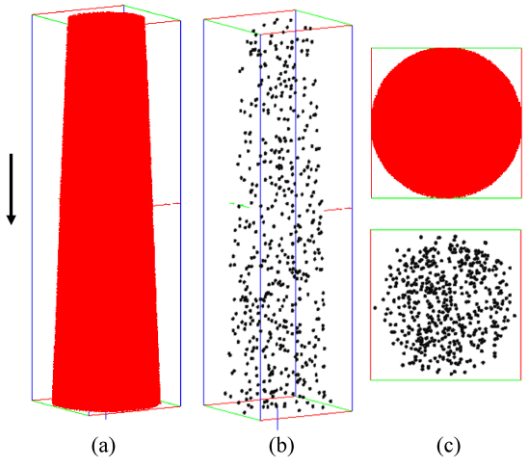

Figure V.5 – Atomically resolved reconstruction of an individual B-doped Si NW core region. Si NW fabricated by etching is annealed at 900 ℃ for 3 h under ultra high vacuum. Three-dimensional tomographic reconstruction of (a) Si atoms and (b) B atoms. (c) Cross-section view of Si and B atoms. B distribution is uniform in Si NW. The analyzed volume is 32×32×120 nm^3. Arrow indicates Si NW etching direction.

As it is shown above, the dopant distribution and concentration depends only on the initial Si bulk for Si NWs synthesized by the “top-down” approach. However, this is a high cost fabrication process. The alternative low cost fabrication mechanism is the VLS mechanism which is based on the “bottom-up” approach. However, this mechanism imposes the complexity of dopant incorporation into Si NWs. Therefore, the information of dopant distribution and concentration is needed to understand how dopant atoms are incorporated into Si NW. In the following parts, the dopant distribution and concentration of Si NWs is presented and discussed. The effects of NW morphology and the nature of the dopant (B or P) on the dopant distribution and concentration are investigated.

V.2 Si nanowires elaborated by Vapor-Liquid-Solid mechanism

V.2.1 B and P distribution and concentration in Si nanowires

V.2.1.1 B-doped Si nanowires with weak tapering

It has been shown in chapter IV.1 that the high growth pressure can inhibit the Au diffusion during Si NW growth. Au atoms can greatly influence the electrical transport due to their high deep traps in Si [3]. Therefore, the B-doped Si NWs are synthesized at high SiH_4 gas pressure in order to eliminate the Au diffusion. The growth experimental condition of the NWs studied here is listed in Table V.1. The total and SiH_4 partial pressure is kept at 10 mbar and 0.65 mbar respectively. The dominant Si NW growth direction is [112] as the precursor pressure is relatively high [4]. For having a B-doped Si NW, B_2H_6 is chosen as the dopant precursor with the ratio SiH_4:B_2H_6= 4000:1. H_2 is chosen as the carrier gas. Si NWs are synthesized at 500 ℃ during 20 min.

Pressure (mbar)	T (℃)	SiH_4 (mbar)	H_2 (sccm)	B_2H_4 (sccm)	Time (min)
10	500	0.65	200	0.05	20

Table V.1 – Growth experimental condition of B-doped Si NWs. Silane is chosen as the precursor gas. Diborane is chosen as the dopant precursor for realizing the B-doped Si NWs. Hydrogen is used as the carrier gas.

A SEM top-view image of this B-doped Si NWs is shown in Figure V.6 (a). In order to perform APT analysis, a single NW need to be extracted form this forest. In order to do so, the specimen preparation method described previously in chapter II.2.4.2 is used. Figure V.6 (b) shows a single B-doped Si NW welded on a W support tip. From the SEM measurement, it is found that the B-doped Si NWs suffer from tapering with a tapering rate evaluated to be 1.9 nm/μm. This weak tapering is mainly caused by the lateral sidewall growth as the migration of catalyst atoms is inhibited effectively at high growth pressure.

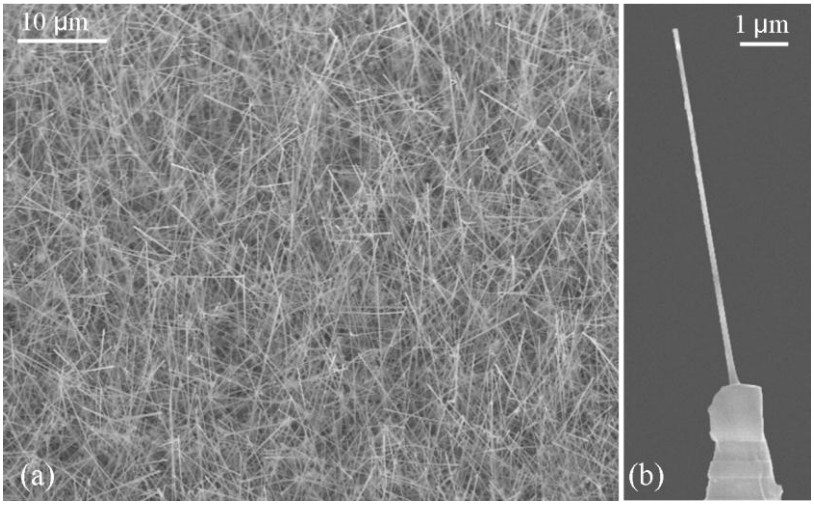

Figure V.6 – Scanning electron microscopy image of B-doped Si NWs grown on a Si substrate. (a) Top-view of the forest of Si NWs. The density of Si NWs is very high because of small diameter of Si NWs. The growth direction of Si NWs is [112]. (b) A single Si NW is welded on a W support tip. Si NW is randomly chosen from the Si NW forest in figure (a).

We reported in chapter II.2.4.2 that the specimen preparation method we are using in order to realize APT experiments (welding a single NW on a support tip), allows to investigate either the base or top region or the sidewall surface of the Si NW. In this last case, the Si NW is intentionally welded with an inclined angle on the W tip in order to detect the NW sidewall surface information. Figure V.7 (a) is a zoom of the base of a Si NW. The hexagonal section or faceting can be seen. This geometry is well reproduced after APT experiment and atomic 3D reconstruction. Figure V.7 (b) and (c) are the atomic reconstruction of Si, O and B atoms (red, green and black dots respectively) of the NW. The volume is $34 \times 33 \times 63$ nm^3. As it can be seen, two facets of the Si NW shown on Figure V.7 (a) are reconstructed in Figure V.7 (b). Normally, the sidewall facets of NW have different crystallographic orientations [5, 6] and different facet length [7]. As far as the Si NWs in this work are concerned, their growth orientation is [112]. They are thus surrounded with two different groups of surface orientation, namely, <111> and <113>. However, we can't point out the precise orientations of the first and second sides observed with APT reconstruction. The non homogeneous distribution of B atoms can be seen, with a B-rich area near the surface, as illustrated in Figure V.7 (b) and (c). No Au atom is detected at the base sidewall surface of Si NW which assesses that there is no migration of Au atoms during growth when the precursor pressure is high.

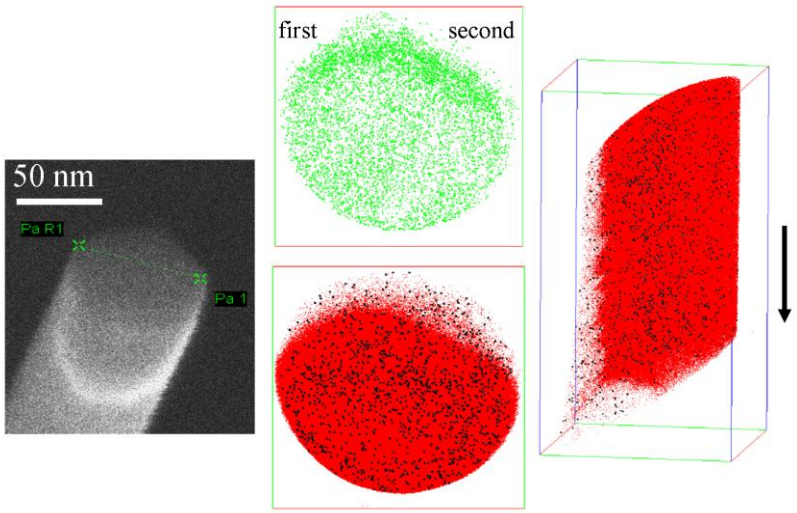

Figure V.7 – Characterization of B-doped Si NW by atom probe tomography. The base sidewall surface is chosen as the investigation region. (a) A zoom of the base end of a single B-doped Si NW welded on a W support tip. A hexagon facet of Si NW can be clearly seen. The 3D reconstruction of an individual B-doped Si NW for (b) cross-section view and (c) side view. The dots and matrix represent B atoms and Si atoms respectively. The volume of analyzed box is 34×33×63 nm^3. Arrow indicates Si NW growth direction.

In order to quantitatively characterize the NW sidewall, a composition profile from the surface toward the core is made. This radial composition profile is given in Figure V.8. Si and O composition profiles are represented with red and green line separately. These composition profiles have been made by moving a "sampling box" step by step along the radius of the NW. The steps are performed every 1 nm. As it is observed on figure V.6, the existence of SiO_2 on NW sidewall surface is evidenced. Figure V.8 also shows the B concentration along the radius in the Si NW (from the surface towards the core). For comparison, the concentrations are calculated from two different radii and the data are plotted as black squares (second side) and blue circles (first side) in Figure V.8. It is clearly shown that the radial B atom distribution is not homogeneous in the Si NW. A lower B concentration is found in the core of the NW in comparison to its near surface. However, these two facet profiles have different tendencies. The mean B concentration for the second side is 6.6×10^{19} B/cm^3 which is higher than the one for the first side (3.6×10^{19} B/cm^3). The combination of our results and the literature observation could lead to the conclusion that the B distribution has a sidewall-facet-dependence due to the different sidewall orientations or facet width. The reason can be discussed as follow. We assume that the deposition of Si atoms and B atoms on NW sidewall

are two separate processes. The B concentration in the Si deposition layer can be written as $C = F_B/F_{Si}$. Where, F_B and F_{Si} represent the B incorporation flux and Si incorporation flux respectively. Therefore, the B concentration on two NW sidewall sides can be written as follow:

$$First \quad side: C_1 = \frac{F_B^1}{F_{Si}^1}; \quad Second \quad side: C_2 = \frac{F_B^2}{F_{Si}^2}$$

The B incorporation flux is believed to be same due to the homogenous decomposition of dopant precursor. Moreover, it is found that the sidewall growth velocity of facet with large width is faster than the one with short width [7] which indicates that there is difference between the two Si incorporation fluxes (F_{Si}^1 and F_{Si}^2) on NW sidewall. Thus, a difference between C_1 and C_2 is expected.

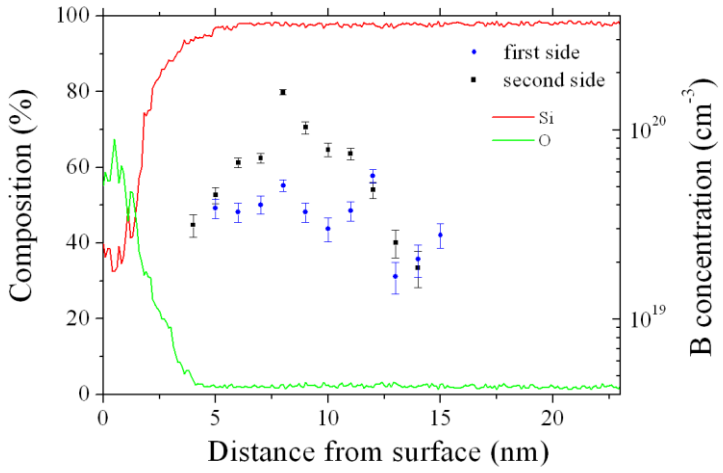

Figure V.8 – Radial profile of single Si NW. The left y axis represents the composition profile of Si and O atoms along the cross-section of an individual B-doped Si NW. Si and O composition profile are represented with red and green line respectively. The right y axis represents the B concentration in Si NW from surface to core. The blue squares and black circulars represent the first and second side NW sidewall surface respectively.

In order to investigate the B distribution in the core region of the NW, a new set of experiments has been performed. In this case, the same specimen preparation procedure is applied as previously, namely, welding a single Si NW on a W tip, but with a very small inclination angle in order to insure that the NW (or its longitudinal direction) is perpendicular to the APT detector. The analysis of the base end of Si NW is also chosen as the analyzed region in order to compare to the previous results and to avoid the specific ending growth.

Figure V.9 (a) is an example of a 3D reconstruction of the core zone of an individual B-doped Si NW. The analyzed volume is $30 \times 30 \times 116$ nm^3. The diameter of the Si NW was 58 nm. Thus the diameter of the analyzed volume can be estimated to be 32.5 nm using Equation II.9 in chapter II. This value is very close to the radius of APT reconstruction cylinder (30 nm). One possible reason for this difference is that there is a global volume compression during the APT reconstruction. Figure V.9 (b) is a slice of volume perpendicular to Si [112] orientation. In that case the inter plane distance is 0.22 ± 0.01 nm (zone A). Figure V.9 (c) is a slice of volume perpendicular to the Si [110] direction (zone B). The inter plane distance in that case is 0.38 ± 0.01 nm. The crystallographic plane means that the B-doped Si NW core is crystalline. However, whether the sites of B atoms in Si are substitutional or interstitial can not be obtained from this slice. Figure V.9 (d) and (e) are the 3D images of O and B atoms in Si NW. The green dots, associated to oxygen, in the volume correspond to the background noise and are not representative. O atoms are only situated in the first layers, at the beginning of the characterization. The calculation of the O concentration in this top region shows a layer of SiO_2 with a thickness of 4 nm. It is reasonable to have a cap of SiO_2 on the top region of the analyzed volume because the characterization region is the NW base. It should be noted here that this oxidation of NW base occurs after the specimen preparation because the specimen is kept in the normal condition without any vacuum control for several days before introducing into the APT specimen chamber. A cross-section view of the radial B distribution is also presented in Figure V.9 (f). It can be clearly seen that B atoms are radial inhomogeneously distributed in the Si NW.

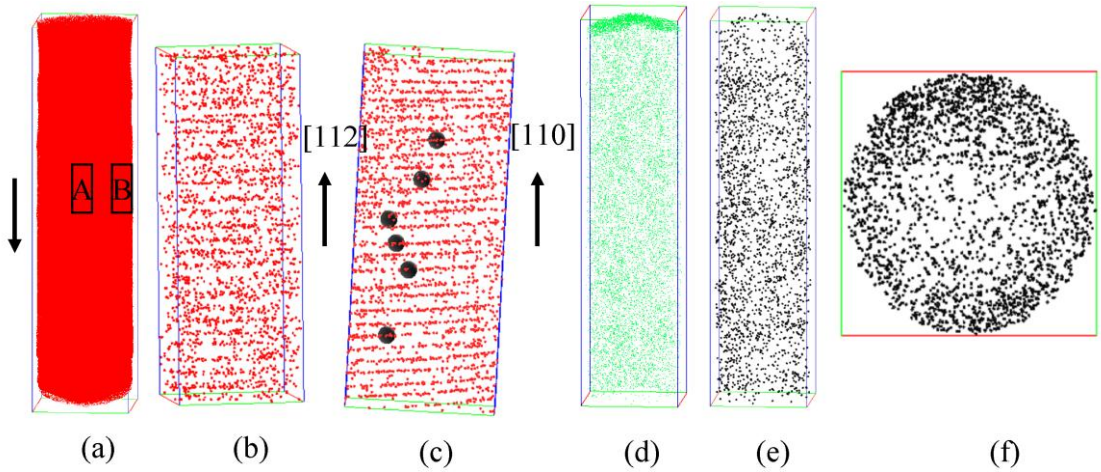

Figure V.9 – Atom probe investigation of an individual B-doped Si NW core region. (a) Three-dimensional tomographic reconstruction of Si atoms. Arrow indicates Si NW growth direction. Crystallographic orientation of NW in (b) centre region (zone A) with [112] and (c) edge region (zone B) with [110]. 3D reconstructions of (d) O atoms and (e) B atoms in Si NW.

The analyzed volume is 30×30×116 nm^3. (f) Cross-section view of radial B distribution. B atoms are not homogeneously distributed in the Si NW.

A quantitative analysis of the B concentration and distribution has been done and is shown in Figure V.10. The inset is the cross-section of the NW where the measurement was performed. The red arrow denotes the path along which the B concentration is measured. It is indicated in Figure V.10 that B concentration can decrease with one order of magnitude in the Si NW over a radial distance of 15 nm from the surface toward the Si NW core. The B concentration in the core ($8.1 \pm 6.6 \times 10^{18}$ B/cm^3) of the Si NW is smaller than the estimation given by the flux ratio, 2.5×10^{19} B/cm^3 in this growth condition.

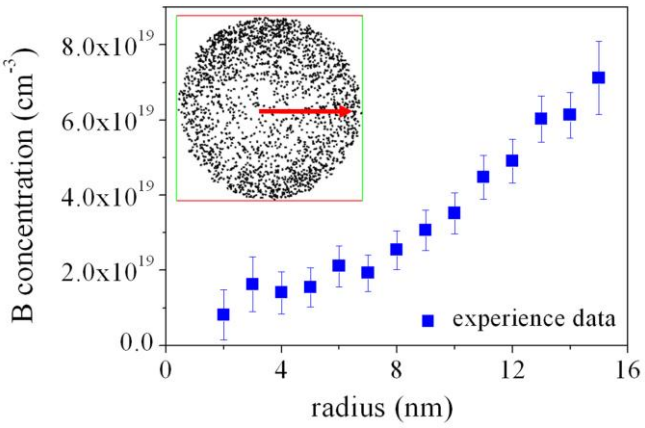

Figure V.10 – Radial concentration profile of B in a Si NW. The inset is the cross-section view of B atoms in Si NW. The red arrow represents the path along which the B concentration is measured.

For comparison, this B-doped Si NW has also been characterized by HRTEM, realized by Dr. G. Patriarche at LPN laboratory, Marcoussis. Figure V.11 is the HRTEM images of different portions of an individual B-doped Si NW. Figure V.11 (a1) is the top end of a Si NW, close to the Au droplet. The existence of Au clusters on the Si NW sidewall surface is evidenced as it has been shown with the 3D APT reconstruction in chapter IV.1. However, it should be noted here that the Au clusters only exist at the top end of the Si NW. This is due to the change in the growing condition at the end of the growth process (decrease of temperature and decrease of gas pressure). Figure V.11 (a2) shows the zoom (with an atomic scale resolution) of the sidewall region of the Si NW shown in Figure V.11 (a1). It shows that the crystalline Si NW is covered by a 4 nm thick SiO_2 layer. This value is consistent with the measurement from APT (chapter IV.1). A very thin B doped layer at the surface of the NW is

also detected. Figure V.11 (b1) is a TEM picture of the middle part (between base and top) of the Si NW. The diameter of Si NW increases as compared to its top end. No Au droplet is observed as expected. A core-shell structure with an under doped core covered by an over doped shell is observed even in this low magnification regime. Figure V.11 (b2) is the atomic structure of the sidewall region of the Si NW shown in Figure V.11 (b1). The dark region represents the high B doped layer which is still crystalline but with some crystal defects such as dislocation or stacking fault. A possible reason of the presence of these defects might be because of the tetrahedral radius of B and Si respectively equals to 0.82 nm and 1.18 nm, with a mismatch ratio of 0.75. This relatively large mismatch can lead to the formation of dislocations. The NW size measurement result reveals a diameter increase of 1.9 nm/μm from the NW top to the base. The non homogeneous axial B concentration assesses that the weak tapering of Si NW is caused by the lateral sidewall growth.

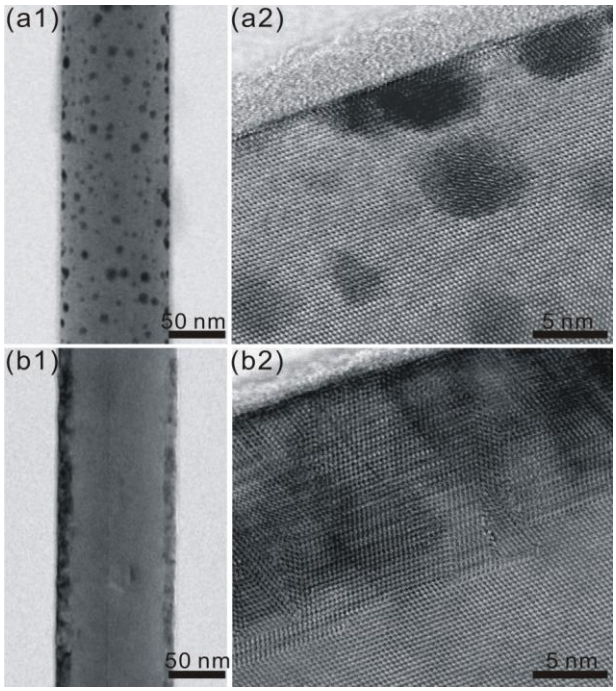

Figure V.11 – High resolution transmission electron microscopy images of different regions of an individual B-doped Si NW. (a1) Image of the top end of the Si NW (close to Au droplet). Arrow indicates Si NW growth direction. (a2) High magnification of sidewall region of Si NW shown in (a1). (b1) Image of middle region of Si NW. (b2) High magnification of sidewall region of Si NW shown in (b1). The dark region represents the high B doped Si layer. The High resolution transmission electron microscope characterization is realized by Dr. G. Patriarche in LPN, Marcoussis.

As a partial conclusion, two phenomena have been confirmed by these HRTEM image: 1) the Au diffusion on NW sidewall is effectively inhibited at high pressure except the ending growth region; 2) there is a sidewall deposition on the NW with an increase of the thickness from the top to the base. Combining the APT and HRTEM results, it can be concluded that B atoms are inhomogeneously distributed along the radial direction. An under doped core is covered by an over doped shell with crystalline defects (dislocation or stacking fault).

It has been shown in the previous chapter that NWs can exhibit the form of cylinder as well as a cone depending on different growth condition. Therefore, to investigate the influence of NW morphology on the distribution and the concentration of dopant is an important issue. In order to realize this characterization, NWs with strong tapering are synthesized. The influence of NW morphology on the mass spectrum of APT is also investigated.

V.2.1.2 B-doped Si nanowires with strong tapering

In this part, B doped Si NWs with a significant tapered shape are investigated. Si NWs are provided by the LAAS laboratory at Toulouse. The experimental condition to get this tapering effect is listed in Table V.3. Silane is also chosen as the Si precursor and boron trichloride is chosen as the dopant precursor. Nitrogen is used as the carrier gas. Boron trichloride is diluted with nitrogen with a ratio of 5%. The growth time and temperature are 32 min. and 470 ℃ respectively. The growth pressure is kept at 149 mbar which is a very high value. The migration of Au atoms on Si NW sidewall surface can be inhibited in such high pressure as shown in chapter III.3 due to the saturation of the atomic sites on the Si NW sidewall.

Pressure (mbar)	T (℃)	SiH_4 (sccm)	5%BCl_3+N_2 (sccm)	Time (min)
149	470	250	200	32

Table V.3 – Growth condition of B-doped Si NWs. Silane is the Si precursor and boron trichloride is the dopant precursor. Nitrogen is used as the carrier gas. B*oron trichloride is diluted with nitrogen with a ratio of 5%.*

The Figure V.12 (a) is a SEM image of the NWs grown in these conditions. A clear tapering effect is observed as shown in Figure V.12. The growth direction of Si NWs is not controlled. There are some kinks during Si NW growth. The catalyst (Au) droplet can be seen

on the top of Si NWs. From the SEM measurements it is shown that the average diameter change with length is estimated to be 48 nm/µm compared to the value of 1.9 nm/µm from the previous B-doped Si NWs series. This large tapering effect is mainly due to the NW sidewall lateral growth rather than the gold diffusion which is inhibited at such high growth pressure. In order to make APT experiments, a single B-doped Si NW is chosen from the Si NW forest and is welded on a W support tip using the same specimen preparation method as previous (Figure V.12 (b)). Here, the top end of Si NW is chosen for investigation. Because the base diameter of NW is very large (≈300 nm) which is not suitable for APT characterization. Although, we can use FIB to mill the NW with larger diameter, the NW surface information is normally destroyed during the FIB process. Therefore, we chose the Au catalyst NW end as the analyzed region. Note here (Figure V.12 (b)) that small "particles" on NW sidewall surface are produced during the welding of sample preparation for APT.

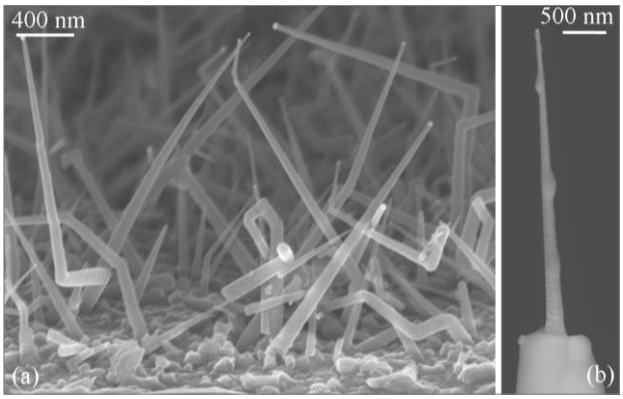

Figure V.12 – Scanning electron microscopy image of B-doped Si NWs with large tapering. (a) Side-view of the forest of Si NWs with 15 ° tilt normal to Si substrate. (b) A single Si NW is welded on a W support tip using the specimen preparation method described previously. Si NW is chosen directly from the Si NW forest in (a).

The 3D APT reconstruction of an individual tapered B-doped Si NW is shown Figure V.13. Si, O and B atoms are represented by red, green and black dots respectively. The analyzed volume is $30 \times 30 \times 116$ nm^3. The diameter of the reconstructed volume is not a constant because of the large tapering effect. The existence of a SiO_2 layer on the Si NW sidewall surface is evidenced. B atoms are not homogeneously distributed in the tapered Si NW.

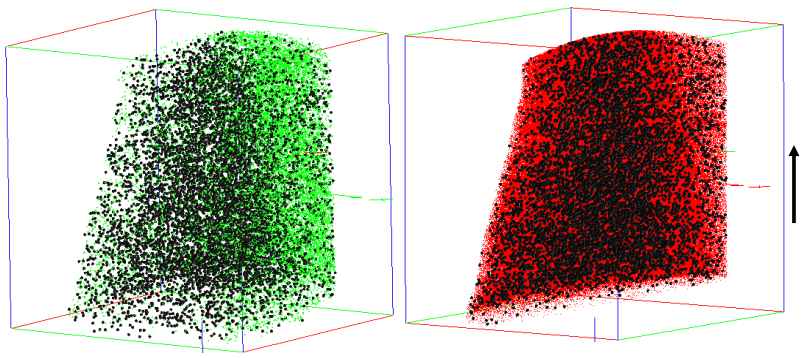

(a) (b)

Figure V.13 – Atom probe tomographic 3D reconstruction of an individual tapered B-doped Si NW. Si, O and B atoms are represented by red matrix, green dots and black dots respectively. (a) The coverage of SiO_2 on B atoms. (b) The inhomogeneous B atom distribution in Si NW. The analyzed volume is 30×30×116 nm^3. Arrow indicates Si NW growth direction.

Indeed, owing to the B concentration and distribution, illustrated in Figure V.14, it is clear that, as in the untapered Si NWs, B atoms accumulate at Si NW sidewall surfaces. The B concentration in the region of 5-20 nm from the surface is calculated to be $3.57 \pm 0.54 \times 10^{20}$ B/cm^3, whereas an estimation of the concentration given by the flux ratio is 1×10^{20} B/cm^3 under this growth condition.

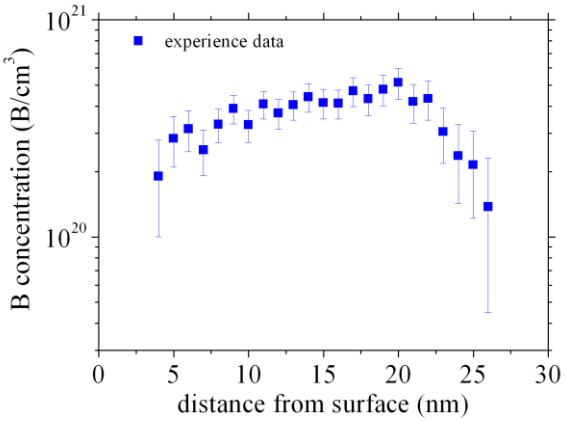

Figure V.14 – Radial B concentration profile in a tapered Si NW. B concentration is plotted from the NW surface to interior. The inhomogeneous B distribution is evidenced as in untapered Si NWs.

In order to investigate the effect of NW morphology on APT results, the mass spectra from these two kinds of B-doped Si NW: with tapering and with weak tapering are compared and discussed. Figure V.15 (a) is the mass spectrum of the Si NW with weak tapering (1.9

nm/µm) and its schematic illustration. The shank angle θ is assumed to be 0 °. A long spectrum thermal tail can be clearly seen following Si peaks. Figure V.15 (b) is the mass spectrum of the Si NW with tapering (48 nm/µm) and its schematic illustration. The shank angle θ is measured to be 2.75 °. The thermal tail on the mass spectrum is lower and shorter compared to the one for untapered Si NW. One possible reason of the existence of the thermal tail following the Si peak is that Si atoms can also be evaporated during the interval of laser pulse despite of its femtosecond. The longer thermal tail in the mass spectrum can degrade the mass resolution. The evaporation of atoms during APT investigation can be viewed as a thermal activation [8]. The shape of the NW influences greatly the temperature relaxation of NW during the interval of laser pulse [9, 10]. For an untapered NW, it needs more time for cooling to the base chamber temperature. The simulation from literature shows that a tip with a taper angle of 4° needs only 50 ns when it is cooled to 70 K compared to 4 µs for an untapered tip [10]. The reason can be explained as follow. The thermal conductivity of Si NW decreases compared to Si bulk [11]. As soon as the heat diffuses from the NW tip (small diameter) to the NW base (large diameter) with a higher thermal conductivity, the cooling rate of NW will increase greatly. By taking advantage of this phenomenon, dependence between sample morphology and mass spectrum quality, NW can be synthesized intentionally with large tapering in order to detect elements with atomic mass larger but near to Si such as P for example.

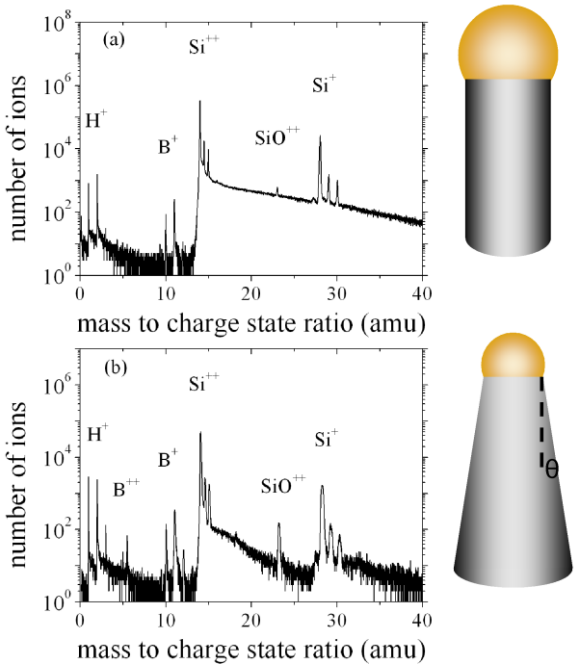

Figure V.15 – Comparison of B-doped Si NW mass spectra. (a) Mass spectrum of an untapered Si NW with a shank angle equals to 0 ° and its schematic illustration. A spectrum

thermal tail can be clearly seen. (b) Mass spectrum of a tapered Si NW and its schematic illustration. The shank angle θ is measured to be 2.75 °.

As a partial conclusion, the inhomogeneous distribution of B atoms in Si NW is a general phenomenon whatever are the morphology of NWs and the dopant precursor. We also show that the NW morphology can influence greatly the quality of the mass spectrum of APT. The mass resolution for the tapered NW is better than the one for the untapered NW due to its faster cooling rate. Therefore, a tapered NW can be intentionally synthesized for detecting the dopant such as P in Si NW with a high resolution. However, it should be noted here that no P-doped Si NW with high tapered morphology is synthesized in this work.

After presenting the no dependence of B distribution with NW morphology, the relation between the dopant distribution and dopant type is also investigated and will be presented in the following paragraphs.

V.2.1.3 P-doped Si nanowires

In this part, P-doped Si NWs are synthesized and characterized. The growth experimental condition is listed in Table V.4. The total and SiH_4 partial pressure is kept at 10 mbar and 0.65 mbar respectively. PH_3 is chosen as the dopant precursor for realizing P-doped dopant. H_2 is chosen as the carrier gas. Si NWs are synthesized at 500 ℃ for 20 min.

Pressure (mbar)	T (℃)	SiH_4 (mbar)	H_2 (sccm)	PH_3 (sccm)	Time (min)
10	500	0.65	200	0.05	20

Table V.4 – Growth experimental condition of P-doped Si NWs. Phosphine is chosen as the dopant precursor for realizing the P-doped Si NWs. Hydrogen is used as the carrier gas.

A SEM image showing a top -view of P-doped Si NWs is presented in Figure V.16 (a). From the SEM measurements, it is also concluded that the tapering of P-doped Si NWs is weak (tapering with a change of 3 nm/μm.) just as B-doped Si NWs. A single Si NW is mounted on a W support tip before the welding procedure of Pt is realized as shown in Figure V.16 (b). It seems that the Si NW is welded inclined on W tip from the side view of SEM. However, the cross-section view of SEM shows that this Si NW is welded on W tip with no inclination from the axis of the overall sample, as shown in Figure V.16 (c). Figure V.16 (c) is

a cross-section view of the Si NW shown in Figure V.16 (b). The direction of the Si NW is perpendicular to the APT detector.

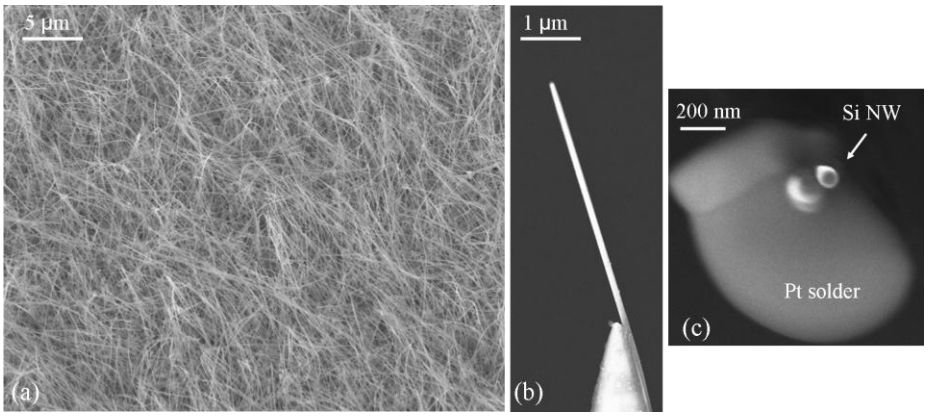

Figure V.16 – Scanning electron microscopy image of P-doped Si NWs grown on a Si substrate. (a) Top-view of the forest of Si NWs. The growth direction of Si NW is [112]. (b) A single Si NW is mounted on a W support tip. Si NW is chosen directly from the Si NW forest in (a). (c) Cross-section view of Si NW in (b) after welded by Pt.

The 3D reconstruction of an individual P-doped Si NW (with a diameter of 70 nm) is shown in Figure V.17 (a). The analyzed volume is $38 \times 38 \times 116$ nm^3. Si and P atoms are represented by black and red dots respectively. Arrow indicates Si NW growth direction. Only the NW core region is characterized by APT because Si NW is perpendicular to APT detector (Figure V.16 (c)). For clarity, the missing information of NW is illustrated with a meshy shell in Figure V.17 (a). The cross-section view of P distribution in Si NW core is presented in Figure V.17 (b).

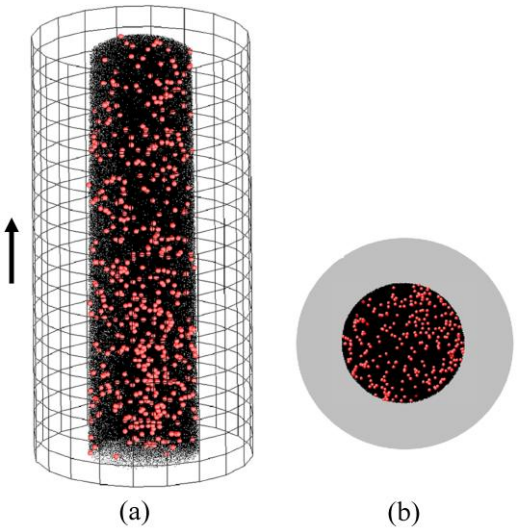

Figure V.17 – 3D reconstruction of an individual P-doped Si NW. Si and P atoms are represented by black and red dots respectively. The analyzed volume is $38 \times 38 \times 116$ nm^3. (a)

The 3D reconstruction of P distribution in Si NW core. The missing NW information during APT investigation is illustrated with a meshy shell. Arrow indicates Si NW growth direction. (b) Cross-section view of P distribution in Si NW core. A weak inhomogeneous distribution of P atoms is found. The grey shell represents the missing information.

In order to quantitatively investigate the P-doped level in the Si NW, the P distribution in the core region is plotted in Figure V.18. P concentration is plotted starting from the Si NW core towards the surface. The concentration of P is $2.6 \pm 1.5 \times 10^{18}$ P/cm^3 in the NW core and gradually increases toward the NW surface up to P concentration of $7.5 \pm 1.9 \times 10^{18}$ P/cm^3 for a distance of 19 nm. The P distribution (gradient) is more flat compared to the one in B-doped Si NW. For B-doped Si NW, the B concentration increases from $8.1 \pm 6.6 \times 10^{18}$ B/cm^3 in the core to $7.1 \pm 0.9 \times 10^{19}$ B/cm^3 for a distance of 15 nm. The possible reason is the higher diffusivity of P in Si compared to the one of B in Si [12]. For a given surface dopant concentration, the tendency of a dopant concentration profile with higher diffusivity is more flat than the one with low diffusivity. This will be discussed in the next paragraph.

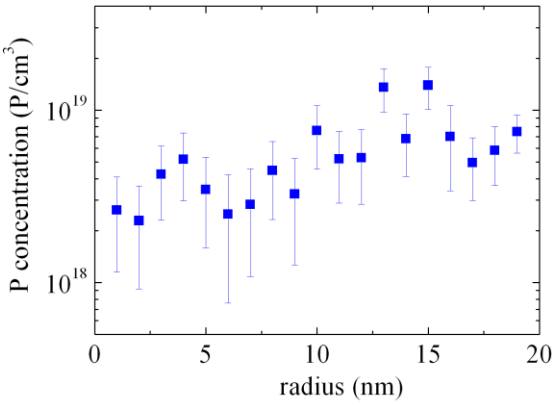

Figure V.18 – Radial plot of P distribution profile in a P-doped Si NW. P concentration is plotted from the NW interior to surface. The tendency of P distribution is more flat compared to the one in B-doped Si NW.

It should be noted here that we did not succeed in the APT characterization of P-doped NW sidewall until now. During our APT characterization of NWs, dozens of NWs with weak tapering (dozens of nanometers of diameter with a length about 10 micro meters) either B-doped or P-doped suffer from fracture often due to the brittleness of NWs. Moreover, the P-doped Si NWs are more brittle as compared to the P-doped one during APT characterization. Therefore, a comparison with Secondary Ion Mass Spectrometry (SIMS) measurements

performed on a film grown simultaneously with our Si NWs is made [13]. It is revealed that the film thickness is similar to the over grown layer on NW sidewall and the concentration of P in the film is measured to be 5×10^{19} P/cm^3. Thus we expect that the P concentration in the NW shell has a similar concentration as in the film which is an order of magnitude higher than the one in the NW core ($2.6 \pm 1.5 \times 10^{18}$ P/cm^3). Thus the P-doped Si NW is expected to exhibit a core-shell structure with a low doped NW core surrounded by a high doped shell as for B-doped Si NWs. The radial variation of P concentration can lead to the formation of n-n$^+$ core-shell structure. The internal electric field created in this kind of core-shell structure can separate the photoexcited electron-hole pairs efficiently as shown by the TRMC technique [13].

In conclusion, the P atoms are also inhomogeneously distributed in the P-doped Si NW as in B-doped Si NW. The P concentration also increases from the NW core towards the surface. As shown in the previous paragraphs, the inhomogeneous distribution of dopant atoms in NW is a rather general phenomenon whatever the NW morphology and dopant type are and can induce the formation of a NW core-shell structure. This kind of core-shell structure can modify the NW properties as compared to the one with uniform dopant distribution. Therefore, to understand the mechanism of the formation of this kind of NW core-shell structure is an important issue. In the parts following, the possible mechanisms of the formation of NW core-shell structure are proposed and discussed.

V.2.2 Modelling the doping of nanowires

Combining the observations of APT and HRTEM, one can consider that there are three different pathways for the dopant to incorporate into NW as illustrated in Figure V.19. The first pathway (arrow 1 in Figure V.19) is the direct incorporation from the vapor into NW through the sidewall. This is the Vapor-Solid (VS) mode, with the formation of a lateral deposition layer, as suggested in this work. It is also suggested in the literature that the incorporation can occurs via the sidewall without any formation of lateral layer [14]. The second pathway (arrow 2 in Figure V.19) could be the direct impingement through the catalyst droplet surface. However, it is mostly believed in the literature, even if the literature is not abundant on this subject, that the dopant profile observed inside the NW is governed by the diffusion from the sidewall into NW because of the higher dissociative chemisorption rate on NW sidewall surface than on the surface of the drop [15]. These authors assume that the precursor fluxes influence the local equilibrium composition of the liquid droplet and thus act

on the liquid-solid interface by changing the chemical potential of species in the droplet. This chemical potential change may, in turn, influence the decomposition of precursor. In Figure V.19, a third pathway for incorporation of dopant is also illustrated. It involves the interfacial boron diffusion along the interface between the droplet and NW. It should be noted that this third pathway is not considered in any modelling and is only expressed here as an additional possibility and is discussed after.

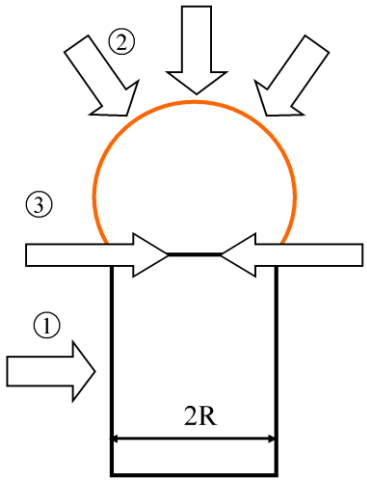

Figure V.19 – Schematic illustration of three possibilities of dopant incorporation into NWs. The first one is the diffusion through the NW sidewall. The second one is the incorporation through the catalyst droplet surface then nucleate into NW. The third one is the interfacial diffusion along the interface between the droplet and the NW.

Therefore, if we assume that the pathway "2" is negligible in the incorporation process of the dopant, the modelling of the diffusion profile of dopant in the NW is simply given by the resolution of the non-stationary diffusion equation. The non-stationary diffusion equation in the NW as a cylinder can be written as (see Annex II):

$$\frac{\partial C}{\partial t} = \frac{1}{r}\frac{\partial}{\partial r}\left(rD\frac{\partial C}{\partial r}\right) \qquad \text{(Equation V.1)}$$

Where, C (r,t) is the radius dependent dopant concentration at time t, r is the distance from the NW centre and D is the dopant diffusion coefficient.

Now, the important point is to choose an appropriate initial boundary condition for diffusion. The initial conditions of Equation V.1 can be written as:

$$C = 0, t = 0$$
$$C = M, r = R, t \geq 0$$

The initial condition shows that there is no dopant distribution at t=0 (no NW growth and no dopant incorporation). The concentration of dopant in the core (r→0) is negligible as

compared to the one diffused from the sidewall. The determination of the NW surface boundary condition M can be discussed as three cases.

The first possible boundary condition is a constant dopant influx M through the sidewall into NW. In this case, the boundary condition at r=R can be written as:

$$M = D\left(\frac{\partial C}{\partial r}\right)_{r=R}$$

The solution of Equation V.1 with this boundary condition can be written as:

$$C(r,t) = \frac{2Mt}{R} + \frac{MR}{D}\left[\frac{r^2}{2R^2} - \frac{1}{4} - 2\sum_{n=1}^{\infty}\frac{J_0(r\alpha_n/R)}{\alpha_n^2 J_0(\alpha_n)}\exp(-D\alpha_n^2 t/R^2)\right] \quad \text{(Equation V.2)}$$

where R is Si NW radius, J_n is the Bessel's function of the first kind of order n which is the solution of Bessel's differential equation

$$x^2\frac{d^2y}{dx^2} + x\frac{dy}{dx} + (x^2 - n^2)y = 0$$

and α_n are the roots of equation $J_0(R\alpha_n) = 0$. ∞ is chosen to be equal to ten and this is an accurate result due to a strong decrease in exponential terms of Equation V.2 with increasing α_n. The first ten roots of this equation and with its corresponding values of $J_1(R\alpha_n)$ are given in Ref. [16]. The values of $J_0(r\alpha_n)$ are given in Ref. [17]. There are two fitting parameters in Equation V.2, namely, the dopant influx M and the diffusion coefficient D. However, it is difficult to choose an appropriate value for the influx M which depends on the chemisorption rate and decomposition rate of dopant precursor. If we chose the influx as the precursor ratio of flux (SiH_4:B_2H_6= 4000:1), the APT result clearly reveals that this estimation is under evaluated. An appropriate and reasonable value for the influx M is difficult to give as it is dependant on the dissociation rate of silane and diborane, which are not known, as well as the evolution in time of these rates. So, this leads to the second case.

The second possible boundary condition is that the NW surface dopant concentration can vary linearly with time with M=kt, where k is the surface doping rate as proposed in the literature [18]. The solution of Equation V.1 can be written as follow using this boundary condition:

$$C(r,t) = k\left(t - \frac{R^2 - r^2}{4D}\right) + \frac{2k}{RD}\sum_{n=1}^{\infty}\exp\left(-D\alpha_n^2 t\right)\frac{J_0\left(r\alpha_n\right)}{\alpha_n^3 J_1\left(R\alpha_n\right)} \quad \text{(Equation V.3)}$$

The boundary condition with *M=kt* can be justified by considering the surface concentration on the NW sidewalls, driven by the influx from the vapor phase, $dc/dt = J$, yielding *c=Jt*. However, the linear increase with time can be broken by the boron desorption

from the sidewalls that should occur at the typical growth temperatures around 500°C. When the desorption is included, the kinetic equation for *c* is changed $dc/dt = J - c/\tau$, with τ being the effective B lifetime on the sidewalls. In this case, the solution is given by $c = J\tau[1-\exp(-t/\tau)]$, showing that, rather than growing infinitely, the surface concentration saturates at a constant value of $J\tau$ at $t >> \tau$. Therefore, a more reasonable boundary condition at large enough t would be a constant concentration. In this case, the boundary condition at r=R can be written as:

$$M = C_0 = const, r = R, t > 0$$

Using this boundary condition, the solution of diffusion Equation V.1 can be written as:

$$\frac{C(r,t)}{C_0} = 1 - \frac{2}{R}\sum_{n=1}^{\infty} \exp\left(-D\alpha_n^2 t\right)\frac{J_0(r\alpha_n)}{\alpha_n J_1(R\alpha_n)} \qquad \text{(Equation V.4)}$$

There are also two fitting parameters in Equation V.4, namely, the surface concentration and the diffusion coefficient. However, the surface concentration C_0 can be measured accurately by APT. Therefore, we chose the third hypothesis for the boundary condition. It must be noted that whatever is the chosen hypothesis, the diffusion equation is based on the Fick's diffusion law in cylinder, only the boundary condition at r=R varies.

Now, the NW surface concentration can be estimated from the APT result. It has been seen that, for B-doped Si NW, the nano-structure is constituted of the NW core (where the APT characterization are mostly made), the lateral deposition shell (the missing information during APT if NW is not inclined during APT characterization) and the SiO_2 layer. Considering the results obtained by APT and illustrated in Figure V.10, the calculation below shows that the entire NW core has been investigated by APT. The diameter of the analyzed volume and the diameter of the entire Si NW are 30 nm and 58 nm, respectively. The thickness of the lateral deposition layer is measured from the NW tapering and it is assumed that there is no decrease of catalyst droplet diameter due to the high growth pressure. Thus the thickness of the lateral deposition layer is estimated to be about 10 nm. The thickness of the SiO_2 layer is measured to be 4 nm following (chapter IV.1). Therefore, we can argue that the outmost region in the APT reconstruction is just the interface between the core and lateral deposition shell. In other word, we assume that the entire NW core is characterized by the APT from the geometry calculation. Thus, the sidewall deposition layer concentration C_0 is equal to the outermost B concentration measured by APT, that is to say 7.1×10^{19} B/cm^3. This value is close the mean B concentration (6.6×10^{19} B/cm^3) in the case of Figure V.7 where the

sidewall surface of another NW is characterized. Using this boundary condition, the fitting of dopant profile can be realized by change the value of D. The doping profile, calculated from Equation V.4, is plotted in Figure V.20. Various profiles are given depending on the diffusion coefficient value. The different diffusion profiles are plotted using different diffusion coefficient but with a fixed sidewall surface concentration C_0. The best fit with the experimental concentration profile is obtained for D = 1.69×10^{-16} cm^2/s. This value is much larger than the one reported for bulk diffusivity of B in Si (≈ 10^{-18} cm^2/s) [12] at the NW growth temperature (500 ℃). It must be noted that considering this bulk diffusivity, B atoms could only diffuse 1 nm under the surface of the NW. Moreover, if this bulk diffusivity is taken into account in the calculation the best fit will be obtained for a surface dopant concentration C_0 of about 3×10^{21} B/cm^3 . This value is much higher than the APT results (7.1×10^{19} B/cm^3) and the estimation of flux (2.5×10^{19} B/cm^3). As a conclusion, it seems that the diffusivity of B in Si NWs is enhanced as compared to the one in Si bulk.

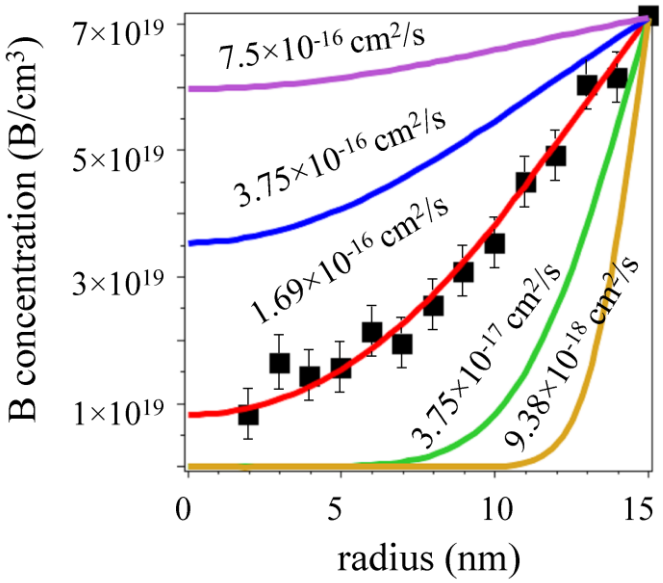

Figure V.20 – Calculated dopant profile for B-doped Si NW. Different profiles are represented with different color which is calculated using different diffusion coefficient but with a fixed NW surface dopant concentration.

The enhancement of dopant diffusivity in semiconductor NWs has been also found in the literature. It is reported in the literature that the P atoms can diffuse into Ge NWs with an enhanced diffusivity of 1×10^{-15} cm^2/s at the growth temperature of 460 ℃ [14]. As far as the diffusion of B atoms in Si bulk is consider, several reasons can induce the enhancement of its diffusivity. It is reported in the literature that the generation of an excess of vacancies [19] can enhance the diffusivity. The diffusion of B in Si can be considered as a vacancy mechanism

under non-oxidizing condition [20]. An excess of vacancies therefore can accelerate the diffusion. In our NW case, there are some defects at the NW sidewall surface as show in Figure V.11. The excess of vacancies at the NW sidewall surface then might be expected. Another explanation is given by [21] which shows an oxidation enhanced diffusion. The interstitial formation energy of B is relatively low (2.26 eV), therefore, the B diffusivity can be enhanced by oxidation with the injection of interstitials into Si. However, in our NW growth case, the diffusion occurs during the NW growth. Whereas, the oxidation of NW occurs after the NW growth when exposure to air at room temperature. It should be noted here that as NW is a typical one-dimensional nanostructure, its very high surface to volume ratio as well as the crucial surface property could also probably enhance the diffusivity.

An alternative explanation to this enhancement of diffusivity or large diffusion profile in NW is to consider that the diffusion or incorporation of B dopant occurs at the interface between catalyst droplet and the NW via the triple line, rather than or in addition to the sidewall surface of the NW as illustrate in Figure V.19. In this case, the high dopant concentration in the NW will be due to the enhance diffusivity of dopant in the molten interface between the droplet and the crystalline NW. When considering this option, an explanation should be given to consider why the dopant atoms could diffuse from the NW surface (or droplet surface) into the catalyst droplet through the TPB rather than to diffuse directly into NW via the sidewall. Although, it is very different from the case of Si diffusion on NW sidewall as during MBE process where the driving force is the chemical potential between the liquid Au-rich droplet and the adatoms, the surface diffusion of boron atoms on the NW sidewall occurs preferentially as compared to the volume diffusion due to the existence of dangling bonds on the NW surface. The dangling bonds can be considered as the "vacancies" and B atoms can diffuse easily with the existence of vacancies. The modelling of the diffusion profile considering this triple line incorporation is under consideration but is rather complex because it implies surface diffusion (surface between solid and gas), liquid diffusion at the interface liquid/solid) and then solid diffusion.

IV.3 Conclusion

In summary, the dopant metrology of B and P atoms in individual Si NWs synthesized by the "top-down" approach and the "bottom-up" approach is realized.

For the Si NWs fabricated by the "top-down" approach, the morphology of Si NWs such as diameter, length and inter distance are well controlled. Our APT results show that the

doping of Si NWs can be effectively controlled by controlling the doping of Si bulk. No change is involved during the fabrication of Si NWs by etching.

As far as the Si NWs synthesized by the "bottom-up" approach is considered, the dopant atoms such as B and P are distributed uniformly in the whole volume of individual Si NWs whatever the NW morphology is. A good agreement is found between the results of APT and HRTEM. The formation of NW core-shell structure is due to the under doped NW core and the over doped shell. The dopant atoms incorporate into NW principally through the sidewall by a diffusion mechanism with a diffusivity D of 1.69×10^{-16} cm^2/s. This value is much larger compared to the one in the Si bulk. Several possible reasons of this enhanced diffusivity are presented and discussed. The influences of NW morphology (weak tapering and strong tapering) on APT mass spectrum are also investigated. It is found that NW with strong tapering has a better mass resolution compared to the one with weak tapering due to the faster cooling.

Bibliography of chapter V

[1] K. Suzuki, H. Yamawaki, and Y. Tada, Solid-State Electron., 41, 1095 (1997)

[2] A. Armigliato, D. Nobili, P. Ostoja, M. Servidori, and a. S. Solme, semiconductor silicon, 77, 638 (1977)

[3] A. J. Tavendale, and S. J. Pearton, J. Phys. C: Solid State Phys., 16, 1665 (1983)

[4] A. Lugstein, M. Steinmair, Y. J. Hyun, G. Hauer, P. Pongratz, and E. Bertagnolli, Nano Lett., 8, 2310 (2008)

[5] Y. Wu, Y. Cui, L. Huynh, C. J. Barrelet, D. C. Bell, and C. M. Lieber, Nano Lett., 4, 433 (2004)

[6] R. Q. Zhang, Y. Lifshitz, D. D. D. Ma, Y. L. Zhao, T. Frauenheim, S. T. Lee, and S. Y. Tong, The Journal of Chemical Physics, 123, 144703 (2005)

[7] T. Xu, J. P. Nys, A. Addad, O. I. Lebedev, A. Urbieta, B. Salhi, M. Berthe, B. Grandidier, and D. Sti évenard, Phys. Rev. B, 81, 115403 (2010)

[8] T. T. Tsong, and T. J. Kinkus, Phys. Rev. B, 29, 529 (1984)

[9] J. H. Bunton, J. D. Olson, D. R. Lenz, and T. F. Kelly, Microsc. Microanal., 13, 418 (2007)

[10] D. E. Perea, E. Wijaya, J. L. Lensch-Falk, E. R. Hemesath, and L. J. Lauhon, J. Solid State Chem., 181, 1642 (2008)

[11] D. Li, Y. Wu, P. Kim, L. Shi, P. Yang, and A. Majumdar, Appl. Phys. Lett., 83, 2934 (2003)

[12] G. E. McGuire, Semiconductor Materials and Process Technology Handbook, Noyes Publication, 501 (1988)

[13] D. H. K. Murthy, T. Xu, W. H. Chen, A. J. Houtepen, T. J. Savenije, L. D. A. Siebbeles, J. P. Nys, C. Krzeminski, B. Grandidier, D. Stievenard, P. Pareige, F. Jomard, G. Patriarche, and O. I. Lebedev, Nanotechnology, 22, 315710 (2011)

[14] E. Koren, N. Berkovitch, and Y. Rosenwaks, Nano Lett., 10, 1163 (2010)

[15] D. E. Perea, E. R. Hemesath, E. J. Schwalbach, J. L. Lensch-Falk, P. W. Voorhees, and L. J. Lauhon, Nat. Nanotechnol., 4, 315 (2009)

[16] A. Gray, and G. B. Mathews, A Treatise on Bessel functions, Macmillan, 280 (1895)

[17] E. T. Goodwin, and J. Staton, The Quarterly Journal of Mechanics and Applied Mathematics, 1, 220 (1948)

[18] E. Koren, J. K. Hyun, U. Givan, E. R. Hemesath, L. J. Lauhon, and Y. Rosenwaks, Nano Lett., 11, 183 (2011)

[19] H. Shibayama, H. Masaki, H. Ishikawa, and H. Hashimoto, J. Electrochem. Soc., 123, 742 (1976)

[20] R. B. Fair, "Concentration Profiles of Diffuse Dopants in Silicon," in F. Y. Y. Yang, Ed. "Impurity dopant Processes in Silicon," North Holland (1981)

[21] H. J. Gossmann, C. S. Rafferty, H. S. Luftman, F. C. Unterwald, T. Boone, and J. M. Poate, Appl. Phys. Lett., 63, 639 (1993)

Conclusion and perspectives

The main subject of this thesis work is to contribute to the understanding of the growth rate and the application of the high resolution analytical technique, namely the Atom Probe Tomography (APT), to the metrology of impurities (catalyst and dopant) in individual Si NWs (NWs) in order to master the elaboration processes. An overview of one-dimensional nanostructures was presented in Chapter I. Two different approaches for the elaboration of these nanostructures, namely, the "top-down" approach (etching in this work) and the "bottom-up" approach (VLS and SLS) mechanisms in this work were described. Si NWs, which are the "nano-materials" studied in this work are presented as well as some general concepts such as the nucleation of Si atoms in catalyst droplet, the migration of atoms from catalysts, the growth direction, the morphology of NW sidewall surface and the NW growth rate. In order to be integrated in devices or components, the Si NWs must be doped. Different doping processes exist but techniques for the dopant metrology are more rare or complex. Often, several techniques must be used and the complementarities of the results give a reasonable trend. In this first part, three widely dopant characterization techniques which are also adapted and applied to NWs are presented and compared. APT is a new one in this field and is the central technique of this work.

In Chapter II, the experimental techniques used in this work were presented in two different parts. The first part deals with the NW elaboration techniques including the etching, the VLS mechanism-based methods (CVD and MBE) and the SLS mechanism-based method. The second part is devoted to the structural and chemical characterization techniques (SEM/FIB, TEM and APT). It must be noted that the latter technique does not give information on physical properties but gives chemical information at the ultimate scale: the atom. APT is the main technique used in this work, and was applied to these materials for the time in the laboratory. The basic concepts and advantages of APT were given in details in this chapter. Several sample preparation methods for APT characterization of NW have been developed in order to realize this work. These methods have been improved during this work, as the high success rate of APT analyses on these nano-objects is strongly based on the specimen preparation.

Chapter III dealt with the modeling of the NW growth rate (length). This parameter is important to control the elaboration and integration of NWs in solar cell devices for example.

Two widely used NW growth methods (CVD and MBE) were chosen. Two different materials, namely, Si and Ge were used to synthesize NWs.

- For CVD-grown Si NWs, an empirical model and a pressure-based model were presented and discussed. A good fit between the experimental data and the fitting curves from both models were found, indicating that the NW growth rate and hence the length increases with the NW diameter and reach a saturation at a given diameter due to the Gibbs-Thomson effect. For catalyst droplets with the same diameter (narrow size distribution), a higher precursor pressure can be used to synthesis longer NWs. The dominant Si incorporation pathway of CVD-grown NWs is the impingement through the catalyst droplet surface.
- For MBE-grown NWs, two different NW growth directions (vertical and inclined) have been characterized and have allowed to investigate the sidewall diffusion of atomic species on the NW growth rate. Two materials were used to grow NWs with different growth directions. The vertical NW was Si NWs, whereas the inclined one was Ge NWs. Normally, the growth rate of MBE-grown NWs decreases with its diameter. However, for the inclined NWs, the time evolution of length-diameter dependence reveals that there is a cross point of the diameter-length dependence at a certain growth time.
- Meanwhile, we also found that the NWs normally suffer from the tapering effect. Two growth conditions can influence this effect simultaneously, namely, the growth precursor pressure and the catalyst droplet density. The tapering of NWs synthesized at high precursor pressure and droplet density is weaker than the one grown at low precursor pressure and droplet density.

In Chapter IV, the APT characterization of different NWs grown from different catalysts was performed. Normally, the use of catalyst for NW growth is necessary and these catalyst impurities can influence the NWs properties. Therefore, in order to obtain the information on the distribution and the concentration of these impurities in the NWs, experiments were performed and were summarized in this chapter. We found that the presence of catalyst atoms in Si NWs is a rather general phenomenon whatever the nature of the catalyst is and whatever the growth mechanism is.

At first, we studied the most widely used catalyst for Si NW synthesis: Au. Two different growth pressures were used to elaborate Si NWs. From APT results, it was found that the upper bound of Au concentration residing in the NW core is 3×10^{17} Au/cm^3 either at a low or high precursor pressures. Moreover, Au atoms can migrate and form clusters on NW

sidewall at low pressure condition. The presence of these Au atoms on NW sidewalls can greatly influence the NW electrical property through the formation of a Schottky barrier. The existence of a SiO_2 layer is also evidenced on Si NW sidewall by APT. Because Au atoms alter the Si NW electrical property, an alternative catalyst such as In or Sn was also used for the Si NW growth. For a good understanding of the diffusion of atoms from the catalysts, two growth mechanisms (VLS and SLS) were used. Again, we found that the catalyst atoms (In and Sn) diffuse into Si NWs whatever the type of growth (VLS or SLS) is. However, different distribution and concentration are found depending on the growth mechanism. In the VLS growth mode, the catalyst atoms tend to distribute uniformly in Si NW. In contrast, in the SLS growth mode, the presence of lamella twin defects, due to the roughness of the nucleation interface, act as segregation sites for catalyst atoms. This segregation of impurities also evolves in clustering, when saturation occurs.

The last chapter is devoted to the dopant metrology in Si NWs using the APT technique. Two different sets of "out of plane" Si NWs were characterized. The first one consists of Si NWs fabricated by etching of B-doped Si wafer. The morphology of these Si NWs, diameter, length and the NW inter space, is effectively controlled under the fabrication process. APT investigations showed that the dopant distribution and concentration is not influenced by the etching process and the dopant level and its distribution correspond to the ones expected in the initial Si bulk. The second set of Si NWs is synthesized by the CVD method. In that case, the dopant atoms (B or P) are inhomogeneously distributed in Si NWs whatever the nature of the dopant is and whatever the morphology of the NW (tapered or not) is. A core-shell structure with an under-doped core surrounded with an over-doped shell is evidenced and quantified by APT and correlate well with HRTEM images of the NWs. Meanwhile, the influence of the NW morphology on APT mass spectrum is also discussed in terms of temperature cooling efficiency. As far as the atomic mechanisms are concerned, the dopant sidewall diffusion is believed to be the dominant mechanism and pathway for their incorporation into NW. A solid diffusion-based model is proposed to simulate the radial inhomogeneous dopant profile in Si NWs. The best fit is given taking into account the Boron diffusivity, D, of 1.69×10^{-16} cm^2/s. This value is much higher than the expected one in Si bulk at the same temperature. This difference is still difficult to correctly understand, but some possible explanations are discussed.

Thus, the atom probe technique has been successfully introduced to the different problematic linked to NW materials. Even if Si NWs have found applications, still lots of work need to be accomplished to fully understand their growth, doping and properties. The

use and the development of nano analytical techniques are essential to reach these goals. Further works should be undertaken in order to develop fundamental relation between the NW growth rate and other experimental conditions such as the growth temperature. As far as the sample preparation method for APT characterization of NW is considered, a direct and convenient method for radial characterization need to be improved and developed. Some tests have been done during this work, but time is needed to improve them and make them successful. In terms of dopant incorporation, the modelling is complex and the parameters that may be involved in the process are numerous. A critical review of their importance and priority is necessary. The collaboration developed during this work with other laboratories has established the base of a new model that is under development.

Annex

I Derivation of growth rate equation

The schematic illustration of the growth rate model is presented in Figure A.1. The first contribution of NW growth rate is influenced by the adsorption-desorption processes on the droplet surface which is directly impinged by the vapor. Therefore, the equation of growth rate can be written as:

$$\frac{\pi R^2}{\Omega}\frac{dL}{dt} = \pi R^2 (J_{ads} - J_{des}^L) \qquad \text{(Equation A.1)}$$

with $J_{ads} = J_\infty^L \exp\frac{\Delta\mu_V - \mu_\infty^L}{k_B T}$ and $J_{des}^L = J_\infty^L \exp\frac{2\Omega\gamma}{Rk_B T}$. It can be obtained that

$$\frac{dL}{dt} = V\left[1 - \exp\left(\frac{\Delta\mu_V - \mu_\infty^L}{k_B T} + \frac{2\Omega\lambda}{Rk_B T}\right)\right] \qquad \text{(Equation A.2)}$$

where, $V=\Omega J_{ads}$ is the direct impingement rate of semiconductor atoms on the droplet surface. Then,

$$\left(\frac{dL}{dH}\right)_{ads} = 1 - \exp\left(\frac{\Delta\mu_V - \mu_\infty^L}{k_B T} + \frac{2\Omega\lambda}{Rk_B T}\right) \qquad \text{(Equation A.3)}$$

where, H=Vt is the deposition thickness of the overgrown layer and t is the NW growth time.

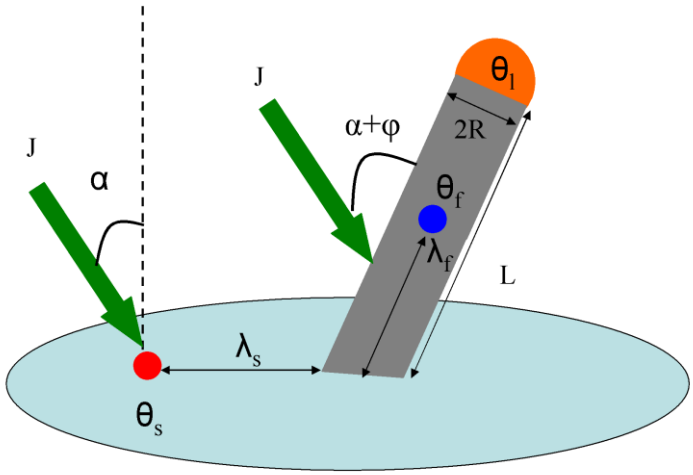

Figure A.1 – Schematic illustration of the model. The parameters are described in the text.

The second contribution of NW growth rate is the diffusion on substrate and sidewall. Stationary adatom concentrations on the substrate surface (n_s) and sidewall facets (n_f) obey diffusion equations

$$D_s \Delta n_s + J\cos\alpha - \frac{n_s}{\tau_s} = 0 \qquad \text{(Equation A.4)}$$

$$D_f \frac{d^2 n_f}{dz^2} + J\sin(\alpha+\varphi) - \frac{n_f}{\tau_f} = 0 \qquad \text{(Equation A.5)}$$

where Δ is the two-dimensional Laplace operator in the substrate plane (r), z is the vertical coordinate, D_s, D_f are the diffusion coefficients, and τ_s, τ_f are the effective lifetimes on the substrate and the sidewalls, respectively. Four boundary conditions to Equation A.1 and A.2 are given by

$$\left.\frac{dn_s}{dr}\right|_{r\to\infty} = 0$$

$$D_s \left.\frac{dn_s}{dr}\right|_{r=R} = -D_f \left.\frac{dn_f}{dz}\right|_{z=0}$$

$$\sigma_s n_s(R) = \sigma_f n_f(0)$$

$$k_B T \ln\left[\sigma_f n_f(L)\right] = \mu_l^{\infty} + \frac{2\gamma\Omega_l}{R} \qquad \text{(Equation A.6)}$$

Solving Equation A.4 and A.5 with boundary conditions (Equation A.6), the diffusion flux to the NW top is obtained from

$$j_{diff}(L) = -D_f\, 2\pi R \left.\frac{dn_f}{dz}\right|_{z=L} \qquad \text{(Equation A.7)}$$

Diffusion induced contribution to the growth rate, $(dL/dt)/_{diff}$ is found by multiplying the diffusion flux by the factor $\pi R^2/\Omega$. The exact result for $(dL/dt)/_{diff}$ can be presented in the form [1]:

$$\left(\frac{dL}{dH}\right)_{diff} = \frac{2\lambda_s}{R}\left[\frac{(\lambda_f/\lambda_s)\dfrac{\omega\sin(\alpha+\varphi)}{\cos\alpha}(1-\theta_l/\theta_f)U(L/\lambda_f) + \delta R/\lambda_s(1-\theta_l/\theta_s)}{dU(L/\lambda_f)/dl}\right] \qquad \text{(Equation A.8)}$$

where, $l=L/\lambda_f$ is the normalized NW length and λ_f is the adatom diffusion length on the NW sidewalls. where, $a=[\omega\, sin(\alpha+\varphi)/cos\alpha]$ is the geometrical factor for the MBE growth with the tilt angle φ to the substrate normal and the beam incident angle α without substrate rotation. $b=(D_s\sigma_f/D_f\sigma_s)$ with D_f, D_s, σ_f and σ_s are the adatom diffusion coefficients and the elementary areas of the sidewall and the substrate. The functions $g_f=1-\theta_l/\theta_f$ and $g_s=1-\theta_l/\theta_s$ describe the

influence of (liquid) droplet chemical potential ("*l*") on the diffusion of sidewall ("*f*") and surface ("s") adatoms. The quantity $\theta_l=exp(\mu_l/k_BT)$ is the activity of semiconductor atoms in the droplet, with μ_l as the corresponding chemical potential, k_B as the Boltzmann constant and T as the substrate temperature. The quantities $\theta_f=exp(\mu_f/k_BT)$ and $\theta_s=exp(\mu_s/k_BT)$ are the effective activities with μ_f and μ_s as the corresponding chemical potentials. The l-dependent function U(l) in Equation A.8 is determined as:

$$U(l)=\sinh(l)+b\frac{\lambda_f}{\lambda_S}\delta\left(\frac{R}{\lambda_S}\right)\left[\cosh(l)-1\right] \qquad \text{(Equation A.9)}$$

with $b=(D_s\sigma_f/D_f\sigma_s)$. The function δ is defined as $\delta(R/\lambda_s)=K_1(R/\lambda_s)/K_0(R/\lambda_s)$, where K_i denotes the modified Bessel function of the second kind of order *i*, and λ_s is the diffusion length of surface adatoms.

Combining the adsorption-desorption and the diffusion contribution, the Equation A.8 can be simply written as:

$$\frac{dL}{dH}=\left(\frac{dL}{dH}\right)_{ads}+\left(\frac{dL}{dH}\right)_{diff}=A+\frac{BU+C}{dU/dl} \qquad \text{(Equation A.10)}$$

The *R*-dependent coefficients *A*, *B* and *C* describe contributions originating from the direct impingement and the growth of quasi two-dimensional surface layer, the diffusion of sidewall and surface adatoms, respectively. The two diffusion-induced contribution of growth rate can be defined as:

$$B=\omega\frac{2\lambda_f\sin(\alpha+\varphi)}{R\cos\alpha}g_f(R);C=\frac{2\lambda_s}{R}\delta\left(\frac{R}{\lambda_s}\right)g_s(R) \qquad \text{(Equation A.11)}$$

Non-linear kinetic equation for L takes a very simple form when A is neglected. Such case corresponds to the diffusion-induced growth with $\lambda_s/R>>1$.Integrating Equation A.10 for A=0 with the initial condition U(H=0), it can be obtained that:

$$U=\frac{C}{B}\left[\exp\left(\frac{BH}{\lambda_f}\right)-1\right] \qquad \text{(Equation A.12)}$$

In view of $B\propto\lambda_f$, the factor C/B in Equation A.4 is inversely proportional to λ_f, while the exponent does not depend on λ_f. Therefore, the universal, λ_f-independent asymptote of Equation A.4 at $L/\lambda_f\to 0$ is obtained by substitution of $sinh(L/\lambda_f)$ to L/λ_f and $cosh(L/\lambda_f)$-1 to $L^2/(2\lambda_f^2)$ in Equation A.2. The resulting U is inversely proportional to λ_f. The λ_f-independent asymptote therefore has the form:

$$L+\frac{b}{2}\delta\left(\frac{R}{\lambda_s}\right)\frac{L^2}{\lambda_s}=\frac{\lambda_s}{a}\delta\left(\frac{R}{\lambda_s}\right)\frac{g_s(R)}{g_f(R)}\left[\exp\left(\frac{2ag_f(R)H}{R}\right)-1\right] \qquad \text{(Equation A.13)}$$

Where, $a=[\omega\sin(\alpha+\varphi)/\cos\alpha]$ is the geometrical factor of MBE growth.

Neglecting the linear term in the left hand side of Equation A.5, it can be obtained that:

$$L = 2\Lambda_s \sqrt{\frac{\exp(2ag_f H/R)-1}{2ag_f}} \qquad \text{(Equation A. 14)}$$

where $\Lambda_s = \lambda_s \sqrt{g_s / b}$ is the effective diffusion length on the substrate surface.

II Diffusion equation

The dopant diffusion into Si NW obeys the Fick's first and second laws of diffusion. These two laws are given, for a one dimensional problem, as:

Fick's first law of diffusion: $J = -D\frac{\partial C}{\partial x}$

where J is the rate of transfer per unit area of section, D the diffusion coefficient, C the dopant concentration and x the space coordinate measured normal to the surface.

Fick's second law of diffusion is given by: $\frac{\partial C}{\partial t} = D\frac{\partial^2 C}{\partial x^2}$

Si NW is, on the average, considered as a cylinder, so that it is simpler to work with cylinder coordinate using the transformation:

$$x = r\cos\theta$$
$$y = r\sin\theta$$

Considering an elementary volume of the cylinder (based on dr, rdθ, dz), the second Fick's law can be rewritten such as:

$$\frac{\partial C}{\partial t} = \frac{1}{r}\left[\frac{\partial}{\partial r}\left(rD\frac{\partial C}{\partial r}\right) + \frac{\partial}{\partial \theta}\left(\frac{D}{r}\frac{\partial C}{\partial \theta}\right) + \frac{\partial}{\partial \mathrm{z}}\left(rD\frac{\partial C}{\partial \mathrm{z}}\right)\right] \qquad \text{(Equation A. 15)}$$

Si NW being considered as on dimensional system (length infinitely larger than radius) the dopant diffusion is only radial and time dependent. Thus, the equation I.3 can be simplified as:

$$\frac{\partial C}{\partial t} = \frac{1}{r}\frac{\partial}{\partial r}\left(rD\frac{\partial C}{\partial r}\right) \qquad \text{(Equation A. 16)}$$

Bibliography of annex

[1] V. G. Dubrovskii, N. V. Sibirev, G. E. Cirlin, I. P. Soshnikov, W. H. Chen, R. Larde, E. Cadel, P. Pareige, T. Xu, B. Grandidier, J. P. Nys, D. Stievenard, M. Moewe, L. C. Chuang, and C. Chang-Hasnain, Phys. Rev. B, 79, 205316 (2009)

Publications

1. W. H. Chen, R. Lardé, E. Cadel, T. Xu, B. Grandidier, J. P. Nys, D. Stiévenard, and P. Pareige, ‘‘Study of the effect of gas pressure and catalyst droplets number density on silicon nanowires growth, tapering and gold coverage’’, **Journal of Applied Physics** 107, 084902, **2010**.
2. W. H. Chen, R. Lardé, E. Cadel, T. Xu, B. Grandidier, J. P. Nys, D. Stievenard, and P. Pareige, ‘‘Growth rate model and doping metrology by atom probe tomography in silicon nanowire’’, **Physica Status Solidi (c),** 8, 771, **2011**
3. V. G. Dubrovskii, N. V. Sibirev, G. E. Cirlin, I. P. Soshnikov, W. H. Chen, R. Larde, E. Cadel, P. Pareige, T. Xu, B. Grandidier, J. P. Nys, D. Stievenard, M. Moewe, L. C. Chuang, and C. Chang-Hasnain, ‘‘Gibbs-Thomson and diffusion-induced contributions to the growth rate of Si, InP, and GaAs nanowires’’, **Physical Review B** 79, 205316, **2009**.
4. M. Roussel, W. H. Chen, E. Talbot, R. Lardé, E. Cadel, F. Gourbilleau, B. Grandidier, D. Stiévenard and P. Pareige, ‘‘Atomic scale investigation of silicon nanowires and nanoclusters’’, **Nanoscale Research Letters** 6, 271, **2011**
5. D.H.K. Murthy, T. Xu, W. H. Chen, T.J. Savenije, L.D.A. Siebbeles, J. P. Nys, C. Kzreminski, B. Grandidier, D. Stiévenard, P. Pareige, F. Jomard, G. Patriarche and O. I. Lebedev, “Efficient photogeneration of long-lived charge carriers in core-shell n-type silicon nanowires”, **Nanotechnology**, 22, 315710, **2011**
6. L. Yu, W. H. Chen, G. Patriarche, S. Bouchoule, P. Pareige R. Rogel, A. C. Salaun, L. Pichon, and P. Roca i Cabarrocas, “Growth-in-place deployment of in-plane silicon nanowires”, **Applied Physics Letters** 99, 203104, **2011**
7. W. H. Chen, V.G. Dubrovskii, X. Liu, T. Xu, R. Lardé, P. Pareige, J. P. Nys, B. Grandidier, D. Stiévenard and G. Patriarche, “Boron distribution in the core of Si nanowire grown by chemical vapor deposition”, **submitted**, **2011**
8. V.G. Dubrovskii, T. Xu, J. P. Nys, B. Grandidier, D. Stiévenard, W. H. Chen and P. Pareige, “Narrowing the length distribution of Ge nanowires”, **submitted**, **2011**

Conference presentations

1. ‘‘Etude des mécanismes de la croissance et du dopage de nanofils de silicium’’, (Oral) Journée nanoscience nord-ouest, Poitier, France 16-17 Octobre, 2008
2. ‘‘Influence des paramètres de fabrication (CVD) sur la croissance des nanofils de silicium: observation et modélisation’’, (Oral) GDR nanofils et nanotubes semiconducteurs Workshop, Autrans, France 30 Juin-03 Juillet, 2009
3. ‘‘Growth mechanism and atom probe studies of silicon nanowires’’, (Poster) 4th nanowire growth Workshop, Paris, France 26-27 October, 2009
4. ‘‘Growth rate models and dopant metrology in silicon nanowire by atom probe tomography’’, (Oral) E-MRS Spring Meeting, Strasbourg, France 7-11 June, 2010
5. ‘‘Atomic scale dopant detection in an individual silicon nanowire by atom probe tomography’’, (Oral) 13th Annual NSTI Nanotech Conference & Trade Show, Anaheim, CA, U.S.A. 21-24 June, 2010
6. ‘‘Growth model and dopant detection in silicon nanowire’’, (Poster) Junior Euromat, Lausanne, Switzerland 26-30 July, 2010
7. ‘‘Atom probe investigation of silicon nanowires grown by VLS and IPSLS’’, (Poster) GDR nanofils et nanotubes semiconducteurs Workshop, Lille, France 20-21 January, 2011
8. ‘‘Investigation of dopants in silicon nanowires grown by Solid-Liquid-Solid or Vapor-Liquid-Solid’’, (Oral) Journée nanoscience nord-ouest, Rouen, France 24-25 March, 2011